

DEPARTMENT OF PHYSICS, UNIVERSITY OF JYVÄSKYLÄ

**JET TRANSVERSE MOMENTUM DISTRIBUTIONS  
MEASURED BY ALICE**

**BY  
TOMAS SNELLMAN**

PHD thesis

Supervisors: Jan Rak, Dong Jo Kim

Jyväskylä, Finland  
December, 2018

## **3** Contents

<b>4</b>	<b>1</b>	<b>Introduction</b>	<b>3</b>
5	1.1	Quantum chromodynamics . . . . .	4
6	1.1.1	Foundation of QCD . . . . .	4
7	1.1.2	Asymptotic Freedom . . . . .	5
8	1.2	Heavy ion physics . . . . .	9
9	1.2.1	History . . . . .	9
10	1.3	Features of Heavy-Ion Collisions . . . . .	11
11	1.3.1	Collision Geometry . . . . .	11
12	1.3.2	Nuclear Geometry . . . . .	12
13	1.3.3	Hydrodynamical Modelling . . . . .	15
14	1.4	Flow . . . . .	18
15	1.4.1	Anisotropic Flow . . . . .	19
16	1.4.2	High $p_T$ Phenomena . . . . .	20
17	1.5	Hard processes . . . . .	21
18	1.5.1	pQCD factorization . . . . .	21
19	1.5.2	Jet hadronisation . . . . .	23
20	1.5.3	Jet energy loss . . . . .	25
21	1.5.4	Monte Carlo Implementations . . . . .	33
22	1.6	QGP in Small systems . . . . .	33
23	1.6.1	Collective phenomena . . . . .	34
24	1.6.2	Absence of jet quenching . . . . .	35
25	<b>2</b>	<b>Experimental setup and data samples</b>	<b>37</b>
26	<b>3</b>	<b>Experimental Details</b>	<b>38</b>
27	3.1	CERN . . . . .	38
28	3.2	Large Hadron Collider . . . . .	40
29	3.2.1	LHC experiments . . . . .	41
30	3.3	ALICE . . . . .	41
31	3.3.1	Tracking . . . . .	42
32	3.3.2	TPC . . . . .	44
33	3.3.3	TPC upgrade . . . . .	44
34	3.3.4	Particle identification . . . . .	46
35	3.3.5	Electromagnetic Calorimeter . . . . .	47
36	3.3.6	Forward detectors . . . . .	47

37	3.3.7	Muon spectrometer . . . . .	48
38	3.3.8	Trigger . . . . .	49
39	<b>4</b>	<b>Event and track selection</b>	<b>50</b>
40	<b>5</b>	<b>Analysis method</b>	<b>50</b>
41	5.1	Jet Finding . . . . .	50
42	5.1.1	Anti $k_T$ algorithm . . . . .	50
43	5.2	$j_T$ . . . . .	51
44	5.2.1	1 over $j_T$ . . . . .	51
45	5.3	Unfolding . . . . .	52
46	5.3.1	Bayesian unfolding . . . . .	53
47	5.3.2	Toy Monte Carlo . . . . .	53
48	5.3.3	Pythia Response matrices . . . . .	54
49	5.3.4	2D response matrices . . . . .	55
50	5.3.5	Unfolding algorithm . . . . .	55
51	5.3.6	Effect of number of iterations . . . . .	55
52	5.3.7	Effect of different prior . . . . .	56
53	5.3.8	Effect of $p_T$ truncation . . . . .	56
54	5.3.9	Unfolding closure test . . . . .	56
55	5.4	Background . . . . .	58
56	5.4.1	Perpendicular cone background . . . . .	59
57	5.4.2	Random background . . . . .	59
58	5.4.3	Auto-correlations . . . . .	62
59	5.5	Fitting . . . . .	62
60	<b>6</b>	<b>Systematic uncertainties</b>	<b>63</b>
61	<b>7</b>	<b>TPC Upgrade?</b>	<b>65</b>
62	<b>8</b>	<b>Systematic errors</b>	<b>66</b>
63	8.1	Background subtraction . . . . .	66
64	8.2	Unfolding . . . . .	66
65	8.3	Tracking . . . . .	66
66	8.4	Combining systematics . . . . .	66
67	<b>9</b>	<b>Results</b>	<b>69</b>
68	9.1	statistics . . . . .	69
69	9.2	Data . . . . .	69
70	9.3	Background . . . . .	69
71	9.4	Inclusive results . . . . .	71
72	9.5	Comparison between A and C side . . . . .	71

73	9.6	Subtracted signal . . . . .	71
74	9.7	Fitting . . . . .	71
75	9.7.1	Results . . . . .	71
76	9.8	Comparison to dihadron results . . . . .	71
77	9.9	Different $R$ parameters . . . . .	75
78	<b>10</b>	<b>Discussion</b>	<b>78</b>
79	10.1	Discussion . . . . .	78
80	<b>11</b>	<b>Summary</b>	<b>80</b>

## 81 List of Figures

82	1	QCD phase diagram . . . . .	7
83	2	$\eta/s$ vs $(T - T_c)/T_c$ . . . . .	8
84	3	The definitions of the Reaction Plane and Participant Plane coordinate systems . . . . .	11
85	4	Interaction between partons in central and peripheral collisions. . . . .	12
86	5	An illustration of the multiplicity distribution in ALICE measurement with centrality classes. . . . .	13
87	6	The results of one Glauber Monte Carlo simulation. . . . .	16
88	7	Schematic representation of a heavy-ion collision . . . . .	17
89	8	Charged particle spectra . . . . .	18
90	9	Illustration of flow in momentum space in central and peripheral collisions. . . . .	19
91	10	QCD Leading Order . . . . .	21
92	11	Hard scattering . . . . .	21
93	12	Jet showering . . . . .	22
94	15	Elliptic flow, $v_2$ from $p_T = 1$ to 60 GeV/ $c$ . . . . .	28
95	16	Photon spectrum . . . . .	29
96	17	Measurements of the nuclear modification factor $R_{AA}$ in central heavy-ion collisions . . . . .	31
97	18	A comparison between observed $R_{AA}(\Delta\phi, p_T)$ and $R_{AA}$ using $v_2$ . . . . .	32
98	19	Calculations of the initial energy density in small collision systems at RHIC and the resulting hydrodynamic evolution. . . . .	34
99	20	Two-particle correlation results in PbPb, pPb, and pp collisions at the LHC []. . . . .	35
100	21	RpA in proton-lead collisions . . . . .	36
101	22	CERN collider complex . . . . .	39
102	23	ALICE . . . . .	42

109	24	ITS . . . . .	43
110	25	TPC . . . . .	45
111	26	Illustration of $\vec{j}_T$ . The jet fragmentation transverse momentum, $\vec{j}_T$ , is defined as the transverse momentum component of the track momentum, $\vec{p}_{\text{track}}$ , with respect to the jet momentum, $\vec{p}_{\text{jet}}$ . . . . .	51
113	27	Results from unfolding in Toy Monte Carlo . . . . .	54
114	28	Unfolding with different number of iterations . . . . .	56
116	29	Effect of changing minimum jet $p_T$ used in unfolding from 5 to 10 GeV . . . . .	57
117	30	Effect of changing minimum jet $p_T$ used in unfolding from 5 to 10 GeV . . . . .	57
119	32	$j_T$ Response matrices in single jet $p_T$ bins . . . . .	59
121	33	Pythia closure test results. Fake tracks include also tracks that do exist in the true dataset, but for one reason or another were not given $j_T$ values. $j_T$ is only calculated for tracks that are associated with jets . . . . .	60
125	35	$j_T$ signal with random background subtraction fits in different jet $p_T$ bins . . . . .	66
126	36	Differences between perpendicular cone and random background subtraction in the resulting RMS values. . . . .	67
128	37	$j_T$ signal with random background subtraction fits in different jet $p_T$ bins . . . . .	67
130	38	Differences between Bayesian and SVD unfolding in the resulting RMS values . . . . .	67
132	39	$j_T$ background with two different methods . . . . .	70
134	40	Inclusive $j_T$ with background . . . . .	70
135	41	Comparison of inclusive $j_T$ distributions between A and C side for minimum bias and EMCAL triggered data. . . . .	72
137	42	$j_T$ signal with background subtracted . . . . .	73
138	43	Comparison of the effect of background method on $j_T$ signal. . . . .	73
139	44	$j_T$ signal fits in different jet $p_T$ bins . . . . .	74
140	45	RMS values extracted from the fits for the gaussian (narrow) and inverse gamma (wide) components . . . . .	74
141	46	RMS values extracted from the fits for the gaussian (narrow) and inverse gamma (wide) components . . . . .	75
143	47	Jet $j_T$ results are compared to results obtained in the dihadron anal- ysis. This is done both in jet $p_T$ and trigger $p_T$ bins by converting between them. . . . .	75
147	48	Pythia $R$ parameters $j_T$ . . . . .	76
148	49	Pythia $R$ parameters RMS . . . . .	77

149	50	Comparison of results with dihadron $j_T$ results. Dihadron trigger $p_T$ bins are converted to jet $p_T$ bins using observed mean $p_{T\text{jet}}$ values in $p_{T\text{trigger}}$ bins. Dihadron results are for $0.2 < x_{  } < 0.4$ . . . . .	78
150			
151	51	PYTHIA $R$ parameters $j_T$ . . . . .	79
152			
153	52	Results of calculating $j_T$ with respect to the jet axis or the leading hadron. The assumption is that because the leading hadron is an imperfect estimate of the jet axis, low $j_T$ tracks should on average be shifted to higher $j_T$ . . . . .	79
154			
155			
156			

# 157 1 Introduction

158 At sufficiently high energies quarks and gluons are no longer bound to hadrons,  
159 but they form a deconfined state known as Quark-Gluon plasma (QGP). The  
160 main goal of heavy ion physics is the study of QGP and its properties. One of the  
161 experimental observables that is sensitive to the properties of QGP is the azimuthal  
162 distribution of particles in the plane perpendicular to the beam direction.

163 When nuclei collide at non-zero impact parameter (non-central collisions), their  
164 overlap region is asymmetric. This initial spatial asymmetry is converted via multi-  
165 ple collisions into an anisotropic momentum distribution of the produced particles.  
166 For low momentum particles ( $p_T \lesssim 3$  GeV/c), this anisotropy is understood to  
167 result from hydrodynamically driven flow of the QGP [1–5].

168 One way to characterize this anisotropy is with coefficients from a Fourier se-  
169 ries parametrization of the azimuthal angle distribution of emitted hadrons. The  
170 second order coefficient,  $v_2$  which is also known as elliptic flow, shows clear depen-  
171 dence on centrality. The collision geometry is mainly responsible for the elliptic  
172 flow. Higher harmonics don't depend that much on centrality. These higher har-  
173 monics carry information about the fluctuations in collisions. The event-by-event  
174 fluctuations have an increasing importance in measurements and it has been ob-  
175 served that measurements of elliptic flow in central collisions and measurements  
176 of higher order harmonics are consistent with the assumption that flow in these  
177 cases is mainly due to fluctuations [6].

178 At LHC energies  $\sqrt{s_{NN}} = 2.76\text{GeV}$  it has been observed that in general there  
179 is little difference to flow at RHIC energies. The  $v_2$  coefficient is about 20% greater  
180 at LHC than at RHIC, depending on the centrality bin. The particle identified  
181  $v_2$  for kaons and pions follows the same trend. However it was observed that for  
182 proton  $v_2$  the quark number scaling does not work [7]. So far there is no agreement  
183 of why this scaling breaks down at LHC or why it works so well at RHIC energies.

184 **1.1 Quantum chromodynamics**

185 **1.1.1 Foundation of QCD**

186 There are four known basic interactions in the universe: gravity, electromagnetic,  
187 weak and strong interactions. The standard model of particle physics includes  
188 three of these excluding the gravitational interaction. The theory of strong inter-  
189 actions is known as Quantum Chromodynamics (QCD).

190 The development of QCD began after the introduction of new powerful particle  
191 accelerators that were capable of particle physics research in the 1950s. Before this  
192 particles were mainly discovered from cosmic rays. Positrons, neutrons and muons  
193 were discovered in the 1930s and charged pions were discovered in 1947 []. The  
194 neutral pion was discovered in 1950 [8].

195 The Lawrence Berkeley National Laboratory started the Bevalac accelerator in  
196 1954, Super Proton Synchrotron (SPS) in CERN began operating in 1959 and the  
197 Alternating Gradient Synchrotron at Brookhaven started in 1960. With an energy  
198 of 33GeV AGS was the most powerful accelerator of that time. By the beginning  
199 of 1960s several new particles had been discovered. These include antiprotons,  
200 antineutrons,  $\Delta$ -particles and the six hyperons ( $\Xi^0$ ,  $\Xi^-$ ,  $\Sigma^\pm$ ,  $\Sigma^0$  and  $\Lambda$ ).

201 Facing this number of different particles started the search for symmetries. Al-  
202 ready in 1932 Heisenberg [9] had proposed an isospin model to explain similarities  
203 between the proton and the neutron. In 1962 Gell-Mann and Ne'eman presented  
204 that particles sharing the same quantum numbers (spin, parity) could be organ-  
205 ised using the symmetry of SU(3). [10] Heisenberg's Isospin model followed the  
206 symmetry of SU(2). Using the SU(3) model known baryons and mesons could be  
207 presented as octets. This also lead to the discovery of the  $\Omega^-$  particle since this  
208 was missing from the SU(3) decoupler that included heavier baryons.

209 The most simple representation of SU(3) was a triplet. Inside this triplet  
210 particles would have electric charges  $2/3$  or  $-1/3$ . These had not been however  
211 detected. In 1964 Gell-Mann [11] and Zweig proposed that baryons and mesons  
212 would bound states of these three hypothetical triplet particles that Gell-Mann  
213 called quarks. Now we know that these are the  $u$ ,  $d$  and  $s$  quarks. This original  
214 quark model was violating the Pauli exclusion principle. For example the  $\Omega^-$   
215 particle is comprised of three  $s$  quarks which would have exactly the same quantum  
216 states.

217 The first one to present the idea of colour was Greenberg already in 1964 [12].  
218 In 1971 Gell-Mann and Frtizsch presented their model, which solved the antisym-  
219 metry problem. They added a colour quantum number to quarks, which separated  
220 quarks of the same species. In the new colour model the baryonic wave function  
221 became

$$(qqq) \rightarrow (q_r q_g q_b - q_g q_r q_b + q_b q_r q_g - q_r q_b q_g + q_g q_b q_r - q_b q_g q_r), \quad (1)$$

222 The colour model was also supported by experimental evidence. The decay  
223 rate of a neutral pion with the addition of colours is

$$\Lambda(\pi^0 \rightarrow \gamma\gamma) = \frac{\alpha^2}{2\pi} \frac{N_c^2}{3^2} \frac{m_\pi^3}{f_\pi^2}. \quad (2)$$

224 For  $N_c = 3$  this gives 7.75eV and the measured value is  $(7.86 \pm 0.54)$  eV [13].

225 Another observable that combines the colour information also to the number  
226 of quark flavours is The Drell-Ratio  $R$  [14]

$$R = \frac{\sigma(e^+ + e^- \rightarrow \text{hadrons})}{\sigma(e^+ + e^- \rightarrow \mu^+ + \mu^-)} = N_c \sum_f Q_f^2. \quad (3)$$

227 This ratio has the numerical value 2 when including the three light quarks  $u$ ,  $d$   
228 and  $s$ . When the collision energy reaches the threshold of heavy quark ( $c$  and  
229  $b$ ) production processes this increases to  $^{10}/3$  (for  $f = u, d, s, c$ ) and  $^{11}/3$  (for  $f =$   
230  $u, d, s, c, b$ ). The threshold of  $t\bar{t}$  production,  $\sqrt{s} \approx 350$ GeV has not been reached  
231 so far by any  $e^+e^-$  colliders.

232 The colour model explained why no free quarks had been observed. Only colour  
233 neutral states are possible. The simplest ways of producing a colour neutral object  
234 are the combination of three quarks, and the combination of a quark-antiquark  
235 pair. These are known as baryons and mesons.

236 After the addition of colour the main ingredients of QCD had been established.  
237 The final quantum field theory of Quantum Chromodynamics formed quickly be-  
238 tween 1972 and 1974. Main part of this was the work Gross, Wilczek, Politzer  
239 and George did for non-abelian gauge field theories [15–19]. Gross, Wilczek and  
240 Politzer received the Nobel Prize in Physics for their work. The role of gluons was  
241 as a colour octet was presented by Fritzsch, Gell-Mann and Leutwyler in 1973 [20].  
242 The theory had now 8 massless gluons to mediate the strong interaction.

243 However, these gluons had not been discovered. Indirect evidence of the ex-  
244 istence had been seen as it was observed that only about half of the momentum  
245 of protons was transported by the quarks [21]. Direct evidence should be seen in  
246 electron-electron collisions as a third, gluonic, jet in addition to two quark jets.  
247 Three jet events were first seen in 1979 at the PETRA accelerator at DESY [22–24].

### 248 1.1.2 Asymptotic Freedom

249 In Quantum Electrodynamics (QED) The electric charge is screened. In the  
250 vicinity of a charge, the vacuum becomes polarized. Virtual charged particle-  
251 antiparticle pairs around the charge are arranged so that opposing charges face

each other. Since the pairs also include an equal amount opposite charge compared to the original charge the average charge seen by an observer at a distance is smaller. When the distance to the charge increases the effective charge decreases until the coupling constant of QED reaches the fine-structure constant  $\alpha = \frac{1}{137}$ .

Contrary to QED QCD is a non-abelian theory. In other words the generators of the symmetry group of QCD, SU(3), do not commute. This has the practical consequence that gluons interact also with other gluons, whereas in QED the neutral carrier particles, photons, only interact with charged particles. There is screening also in QCD because of the colour charges, but in addition to that there is antiscreening because of the gluon interactions. In QCD the antiscreening effect is stronger than screening. For larger distances to the colour charge the coupling constant is larger. This explains why no free colour charges can be observed. When the distance between charges increases the interaction strengthens until it is strong enough to produce a new quark-antiquark pair.

On the other hand, at very small distances the coupling constant approaches 0. This is called asymptotic freedom. For large energies and small distances the coupling constant is negligible. In 1975 Collins [25] predicted a state where individual quarks and gluons are no longer confined into bound hadronic states. Instead they form a bulk QCD matter that Edward Shuryak called Quark-Gluon plasma in his 1980 review of QCD and the theory of superdense matter [26]. QGP can be seen as a separate state of matter. A schematic view of a phase diagram for QCD matter is shown in Fig. 1.

In the early universe at the age of  $10^{-6}$ s after the Big Bang the conditions preferred the existence of QGP instead of hadronic matter. Nowadays bulk QCD matter, its properties and its phase transitions between hadronic matter and the quark-gluon plasma (QGP) can be explored in the laboratory, through collisions of heavy atomic nuclei at ultra-relativistic energies. The study of QCD matter at high temperature is of fundamental and broad interest. The phase transition in QCD is the only phase transition in a quantum field theory that can be probed by any present or foreseeable technology.

One important property of the QGP is the shear viscosity to entropy ratio,  $\eta/s$ . It is believed that this ratio has an universal minimum value of  $1/4\pi \approx 0.8$ , which holds for all substances. This limit would be reached in the strong coupling limit of certain gauge theories [28]. The temperature dependance of the ratio is shown in Fig. 2. The minimum value of  $\eta/s$  is found in the vicinity of the critical temperature,  $T_c$  [29]. Finding the  $\eta/s$  values in QGP matter would therefore also provide a way of determining the critical point of QCD matter.

The  $\eta/s$  value for the matter created in Au-Au collisions at RHIC ( $\sqrt{s_{NN}}$ ) has been estimated to be  $0.09 \pm 0.015$  [29], which is very close to the lowest value for a wide class of thermal quantum field theories [28] for all relativistic quantum field

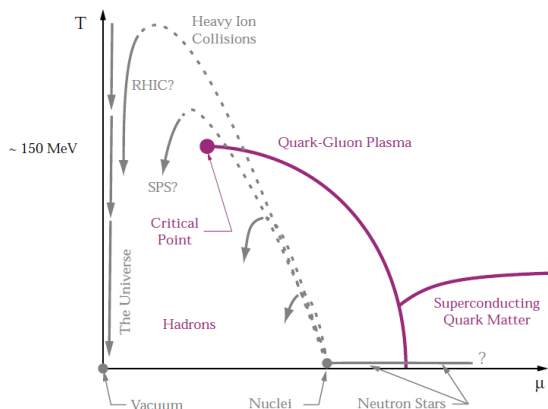


Figure 1: A schematic outline for the phase diagram of QCD matter at ultra-high density and temperature. The quark chemical potential  $\mu$  that is on the x-axis represents the imbalance between quarks and antiquarks. At zero temperature this corresponds to the number of quarks but at higher temperatures there are also additional pairs of quarks and antiquarks. Along the horizontal axis the temperature is zero, and the density is zero up to the onset transition where it jumps to nuclear density, and then rises with increasing  $\mu$ . Neutron stars are in this region of the phase diagram, although it is not known whether their cores are dense enough to reach the quark matter phase. Along the vertical axis the temperature rises, taking us through the crossover from a hadronic gas to the quark-gluon plasma. This is the regime explored by high-energy heavy-ion colliders. [27]

theories at finite temperature and zero chemical potential. This suggests that the matter created goes through a phase where it is close to the critical point of QCD.

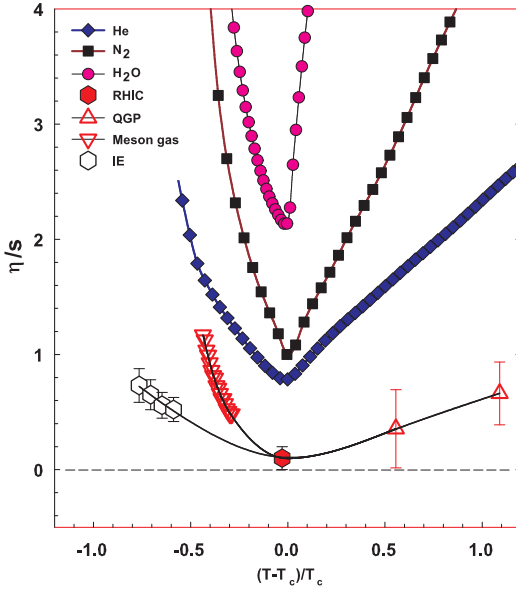


Figure 2:  $\eta/s$  as a function of  $(T - T_c)/T_c$  for several substances as indicated. The calculated values for the meson-gas have an associated error of  $\sim 50\%$ . The lattice QCD value  $T_c = 170$  MeV is assumed for nuclear matter. The lines are drawn to guide the eye. [29]

## **295 1.2 Heavy ion physics**

**296** The Quark Gluon Plasma (QGP) is experimentally accessible by colliding heavy  
**297** ions at high energies. Nowadays research of Heavy-Collisions is mainly performed  
**298** at two particle colliders; the The Relativistic Heavy Ion Collider (RHIC) at BNL  
**299** in New York, USA and he Large Hadron Collider (LHC) at CERN in Switzer-  
**300** land. Energy densities at these colliders should be enough to produce QGP and  
**301** convincing evidence of the creation has been seen at both colliders.

**302** The development of heavy ion physics is strongly connected to the development  
**303** of particle colliders. Experimental study of relativistic heavy ion collisions has been  
**304** carried out for three decades, beginning with the Bevalac at Lawrence Berkeley  
**305** National Laboratory (LBNL) [30], and continuing with the AGS at Brookhaven  
**306** National Laboratory (BNL) [31], CERN SPS [32], RHIC at BNL and LHC at  
**307** CERN. The first colliders could not produce enough energy to create QGP matter  
**308** so they could only probe the hadronic state.

**309** The collective motion of matter in a heavy-ion collision has been modeled using  
**310** several models e.g. the Blast wave Model [33] has been used successfully. Another  
**311** model growing in popularity is the hydrodynamical approach which is further  
**312** discussed in section 1.3.3.

### **313 1.2.1 History**

**314** The first heavy-ion collisions were done at the Bevalac experiment at the Lawrence  
**315** Berkeley National Laboratory [30] and at the Joint Institute for Nuclear Research  
**316** in Dubna [34] at energies up to 1GeV per nucleon. In 1986 the Super Proton  
**317** Synchrotron (SPS) at CERN started to look for QGP signatures in O+Pb col-  
**318** lisions. The center-of-mass energy per colliding nucleon pair ( $\sqrt{s_{NN}}$ ) was 19.4  
**319** GeV [32]. These experiments did not find any decisive evidence of the existence  
**320** of QGP. In 1994 a heavier lead (Pb) beam was introduced for new experiments  
**321** at  $\sqrt{s_{NN}} \approx 17$  GeV. At the same time the Alternating Gradient Synchrotron  
**322** (AGS) at BNL, Brookhaven collided ions up to  $^{32}\text{S}$  with a fixed target at energies  
**323** up to 28GeV [31]. Although the discovery of a new state of matter was reported  
**324** at CERN, these experiments provided no conclusive evidence of QGP. Now SPS  
**325** is used with 400 GeV proton beams for fixed-target experiments, such as the SPS  
**326** Heavy Ion and Neutrino Experiment (SHINE) [35], which tries to search for the  
**327** critical point of strongly interacting matter.

**328** The Relativistic Heavy Ion Collider (RHIC) at BNL in New York, USA started  
**329** its operation in 2000. The top center-of-mass energy per nucleon pair at RHIC, 200  
**330** GeV, was reached in the following years. The results from the experiments at RHIC  
**331** have provided a lot of convincing evidences that QGP was created [1,2,36,37]. The  
**332** newest addition to the group of accelerators capable of heavy-ion physics is the

<sup>333</sup> Large Hadron Collider (LHC) at CERN, Switzerland. LHC started operating in  
<sup>334</sup> November 2009 with proton-proton collisions. First Pb-Pb heavy ion runs started  
<sup>335</sup> in November 2010 with  $\sqrt{s_{NN}} = 2.76$  TeV, over ten times higher than at RHIC.  
<sup>336</sup> Among the six experiments at LHC, the Large Ion Collider Experiment (ALICE)  
<sup>337</sup> is dedicated to heavy ion physics. Also CMS and ATLAS have active heavy ion  
<sup>338</sup> programs.

339 **1.3 Features of Heavy-Ion Collisions**

340 **1.3.1 Collision Geometry**

341 In contrast to protons atomic nuclei are objects with considerable transverse size.  
342 The properties of a heavy-ion collision depend strongly on the impact parameter  
343  $b$  which is the vector connecting the centers of the two colliding nuclei at their  
344 closest approach. One illustration of a heavy-ion collision is shown in Fig. 3.

345 Impact parameter defines the reaction plane which is the plane spanned by  $b$   
346 and the beam direction.  $\Psi_{RP}$  gives the angle between the reaction plane and some  
347 reference frame angle. Experimentally the reference frame is fixed by the detector  
348 setup. Reaction plane angle cannot be directly measured in high energy nuclear  
 collisions, but it can be estimated with the event plane method [38].

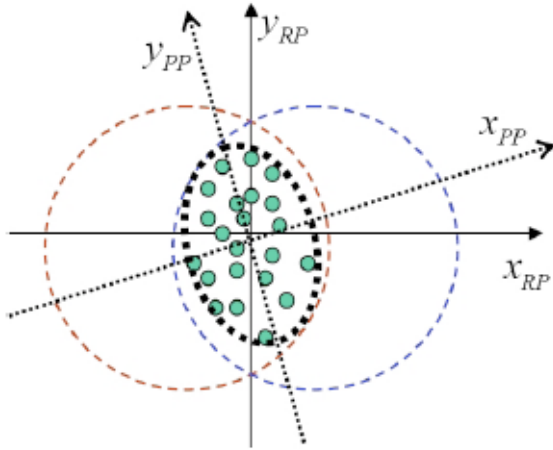


Figure 3: The definitions of the Reaction Plane and Participant Plane coordinate systems [39]. The dashed circles represent the two colliding nuclei and the green dots are partons that take part in the collision.  $x_{PP}$  and  $x_{RP}$  are the participant and reaction planes. The angle between  $x_{RP}$  and  $x_{PP}$  is given by Eq. (4).  $y_{PP}$  and  $y_{RP}$  are lines perpendicular to the participant and reaction planes.

349  
350 Participant zone is the area containing the participants. The distribution of  
351 nucleons in the nucleus exhibits time-dependent fluctuations. Because the nucleon  
352 distribution at the time of the collision defines the participant zone, the axis of  
353 the participant zone fluctuates and can deviate from the reaction plane. The angle  
354 between the participant plane and the reaction plane is defined by [40]

$$\psi_{PP} = \arctan \frac{-2\sigma_{xy}}{\sigma_y^2 - \sigma_x^2 + \sqrt{(\sigma_y^2 - \sigma_x^2)^2 + 4\sigma_{xy}^2}}, \quad (4)$$

355 where the  $\sigma$ -terms are averaged over the energy density.

$$\sigma_y^2 = \langle y^2 \rangle - \langle y \rangle^2, \sigma_x^2 = \langle x^2 \rangle - \langle x \rangle^2, \sigma_{xy} = \langle xy \rangle - \langle x \rangle \langle y \rangle \quad (5)$$

356 The impact parameter is one way to quantize the centrality of a heavy-ion  
 357 collision but it is impossible to measure in a collision. It can be estimated from  
 358 observed data using theoretical models, but this is always model-dependent and  
 359 to compare results from different experiments one needs an universal definition for  
 360 centrality. The difference between central and peripheral collisions is illustrated  
 361 in Fig. 4. In a central collision the overlap region is larger than in a peripheral  
 362 collision. Larger overlap region translates into a larger number of nucleons partici-  
 363 pating in the collision, which in turn leads to a larger number of particles produced  
 364 in the event.

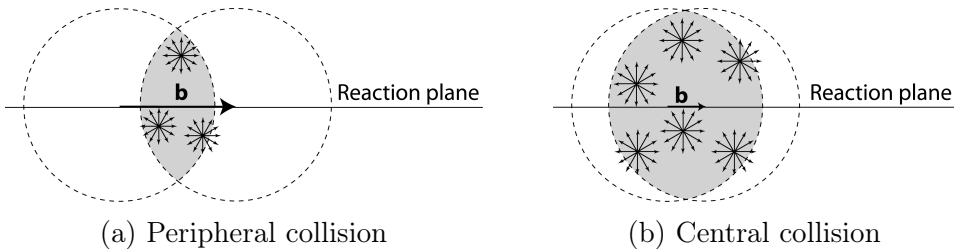


Figure 4: Interaction between partons in central and peripheral collisions. The snowflakes represent elementary parton-parton collisions. When the impact parameter  $b$  is large the number of elementary collisions is small. Particle production is small. Smaller impact parameter increases the number of elementary collisions. This increases particle production.

365 Usually centrality is defined by dividing collision events into percentile bins by  
 366 the number participants or experimentally by the observed multiplicity. Centrality  
 367 bin 0-5% corresponds to the most central collisions with the highest multiplicity  
 368 and higher centrality percentages correspond to more peripheral collisions with  
 369 lower multiplicities. A multiplicity distribution from ALICE measurements [41]  
 370 illustrating the centrality division is shown in Fig. 5. The distribution is fitted  
 371 using a phenomenological approach based on a Glauber Monte Carlo [42] plus a  
 372 convolution of a model for the particle production and a negative binomial distri-  
 373 bution.

### 374 1.3.2 Nuclear Geometry

375 To model heavy-ion collisions one must first have a description as good as possible  
 376 of the colliding objects. Atomic nuclei are complex ensembles of nucleons. The  
 377 nuclei used in heavy-ion physics have in the order of 200 nucleons. Mostly used

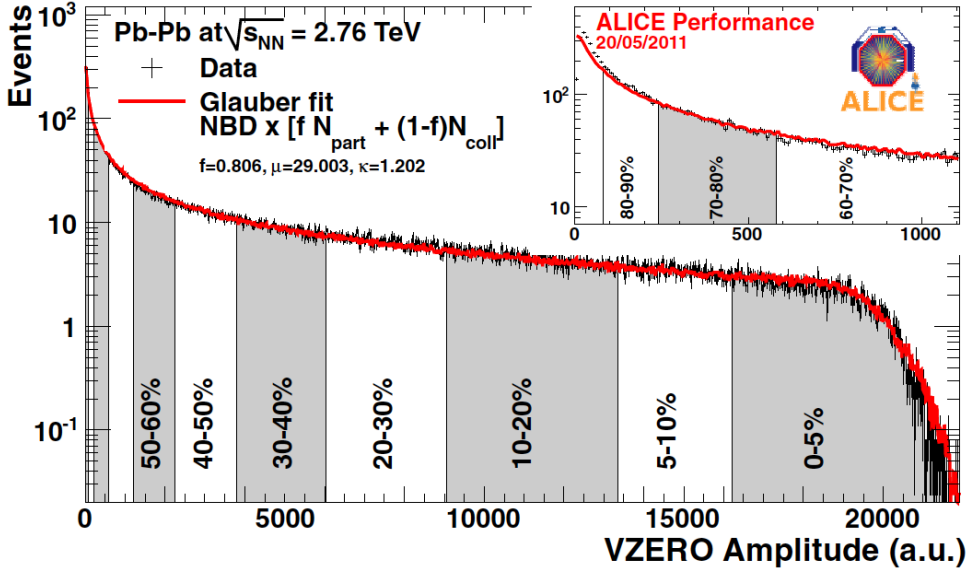


Figure 5: An illustration of the multiplicity distribution in ALICE measurements. The red line shows the fit of the Glauber calculation to the measurement. The data is divided into centrality bins [41]. The size of the bins corresponds to the indicated percentile.

<sup>378</sup> nuclei are <sup>208</sup>Pb at LHC and <sup>197</sup>Au at RHIC. The distribution of these nucleons  
<sup>379</sup> within a nucleus is not uniform and is subject to fluctuations in time.

<sup>380</sup> Nuclear geometry in heavy-ion collisions is often modelled with the Glauber  
<sup>381</sup> Model. The model was originally developed to address the problem of high energy  
<sup>382</sup> scattering with composite particles. Glauber presented his first collection of papers  
<sup>383</sup> and unpublished work in his 1958 lectures [43]. In the 1970's Glauber's work  
<sup>384</sup> started to have utility in describing total cross sections. Maximon and Czyz applied  
<sup>385</sup> it to proton-nucleus and nucleus-nucleus collisions in 1969 [44].

<sup>386</sup> In 1976 [45] Białas, Bleszyński, and Czyz applied Glauber's approach to  
<sup>387</sup> inelastic nuclear collisions. Their approach introduced the basic functions used in  
<sup>388</sup> modern language including the thickness function and the nuclear overlap function.  
<sup>389</sup> Thickness function is the integral of the nuclear density over a line going through  
<sup>390</sup> the nucleus with minimum distance  $s$  from its center

$$T_A(s) = \int_{-\infty}^{\infty} dz \rho(\sqrt{s^2 + z^2}). \quad (6)$$

<sup>391</sup> This function gives the thickness of the nucleus, i.e. the amount material seen by  
<sup>392</sup> a particle passing through it.

<sup>393</sup> Overlap function is an integral of the thickness functions of two colliding nuclei  
<sup>394</sup> over the overlap area. This can be seen as the material that takes part in the  
<sup>395</sup> collision. It is given as a function of the impact parameter  $b$

$$T_{AB}(b) = \int ds^2 T_A(\bar{s}) T_B(\bar{s} - \bar{b}) \quad (7)$$

<sup>396</sup> The average overlap function,  $\langle T_{AA} \rangle$ , in an A-A collisions is given by [46]

$$\langle T_{AA} \rangle = \frac{\int T_{AA}(b) db}{\int (1 - e^{-\sigma_{pp}^{inel} T_{AA}(b)}) db}. \quad (8)$$

<sup>397</sup> Using  $\langle T_{AA} \rangle$  one can calculate the mean number of binary collisions

$$\langle N_{coll} \rangle = \sigma_{pp}^{inel} \langle T_{AA} \rangle, \quad (9)$$

<sup>398</sup> where the total inelastic cross-section,  $\sigma_{pp}^{inel}$ , gives the probability of two nucleons  
<sup>399</sup> interacting. The number of binary collisions is related to the hard processes in a  
<sup>400</sup> heavy-ion collision. Each binary collision has equal probability for direct produc-  
<sup>401</sup> tion of high-momentum partons. Thus the number of high momentum particles is  
<sup>402</sup> proportional to  $\langle N_{coll} \rangle$ .

<sup>403</sup> Soft production on the other hand is related to the number of participants.  
<sup>404</sup> It is assumed that in the binary interactions participants get excited and further  
<sup>405</sup> interactions are not affected by previous interactions because the time scales are  
<sup>406</sup> too short for any reaction to happen in the nucleons. After the interactions ex-  
<sup>407</sup> cited nucleons are transformed into soft particle production. Production does not  
<sup>408</sup> depend on the number of interactions a nucleon has gone through. The average  
<sup>409</sup> number of participants,  $\langle N_{part} \rangle$  can also be calculated from the Glauber model

$$\begin{aligned} \langle N_{part}^{AB}(b) \rangle &= \int ds^2 T_A(\bar{s}) \left[ 1 - \left[ 1 - \sigma_{NN} \frac{T_B(\bar{s} - \bar{b})}{B} \right]^B \right] \\ &+ \int ds^2 T_B(\bar{s}) \left[ 1 - \left[ 1 - \sigma_{NN} \frac{T_A(\bar{s} - \bar{b})}{A} \right]^A \right]. \end{aligned} \quad (10)$$

<sup>410</sup> Glauber calculations require some knowledge of the properties of the nuclei.  
<sup>411</sup> One requirement is the nucleon density distribution, which can be experimen-  
<sup>412</sup> tally determined by studying the nuclear charge distribution in low-energy elec-  
<sup>413</sup> tron scattering experiments [42]. The nucleon density is usually parametrized by  
<sup>414</sup> a Woods-Saxon distribution

$$\rho(r) = \frac{\rho_0}{1 + \exp\left(\frac{r-R}{a}\right)}, \quad (11)$$

415 where  $\rho_0$  is the nucleon density in center of the nucleus,  $R$  is the nuclear radius  
 416 and  $a$  parametrizes the depth of the skin. The density stays relatively constant as  
 417 a function of  $r$  until around  $R$  where it drops to almost 0 within a distance given  
 418 by  $a$ .

419 Another observable required in the calculations is the total inelastic nucleon-  
 420 nucleon cross-section  $\sigma_{\text{inel}}^{\text{NN}}$ . This can be measured in proton-proton collisions at  
 421 different energies.

422 There are two often used approaches to Glauber calculations. The optical ap-  
 423 proximation is one way to get simple analytical expressions for the nucleus-nucleus  
 424 interaction cross-section, the number of interacting nucleons and the number of  
 425 nucleon-nucleon collisions. In the optical Glauber it is assumed that during the  
 426 crossing of the nuclei the nucleons move independently and they will be essentially  
 427 undeflected.

428 With the increase of computational power at hand the Glauber Monte Carlo  
 429 (GMC) approach has emerged as a method to get a more realistic description of  
 430 the collisions. In GMC the nucleons are distributed randomly in three-dimensional  
 431 coordinate system according to the nuclear density distributions. Also nuclear  
 432 parameters, like the radius  $R$  can be sampled from a distribution. A heavy-ion  
 433 collision is then treated as a series of independent nucleon-nucleon collisions, where  
 434 in the simplest model nucleons interact if their distance in the plane orthogonal  
 435 to the beam axis,  $d$ , satisfies

$$d < \sqrt{\sigma_{\text{inel}}^{\text{NN}}} \quad (12)$$

436 The average number of participants and binary collisions can then be determined  
 437 by simulating many nucleus-nucleus collisions. The results of one GMC Pb-Pb  
 438 event with impact parameter  $b = 9.8\text{fm}$  is shown in Fig. 6

### 439 1.3.3 Hydrodynamical Modelling

440 The relativistic version of hydrodynamics has been used to model the deconfined  
 441 phase of a heavy-ion collision with success. Heavy-ion collisions produce many  
 442 hadrons going into all directions. It is expected that tools from statistical physics  
 443 would be applicable to this complexity [47]. The power of relativistic hydrodynam-  
 444 ics lies in its simplicity and generality. Hydrodynamics only requires that there is  
 445 local thermal equilibrium in the system. In order to reach thermal equilibrium the  
 446 system must be strongly coupled so that the mean free path is shorter than the  
 447 length scales of interest [48].

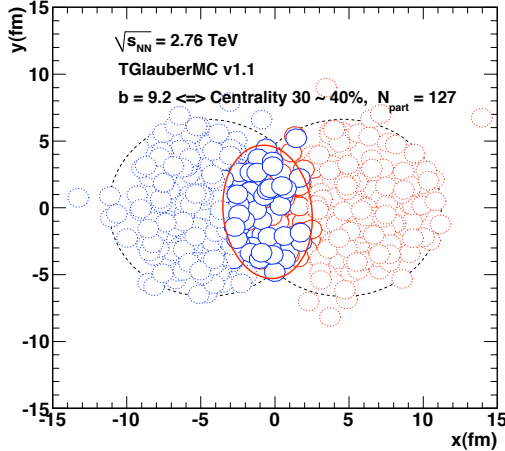


Figure 6: The results of one Glauber Monte Carlo simulation. Big circles with black dotted boundaries represent the two colliding nuclei. The participant zone is highlighted with the solid red line. Small red and blue circles represent nucleons. Circles with thick boundaries are participants i.e. they interact with at least one nucleon from the other nucleus. Small circles with dotted boundaries are spectators which do not take part in the collision.

448     The use of relativistic hydrodynamics in high-energy physics dates back to  
 449 Landau [49] and the 1950's, before QCD was discovered. Back then it was used  
 450 in proton-proton collisions. Development of hydrodynamics for the use of heavy-  
 451 ion physics has been active since the 1980's, including Bjorken's study of boost-  
 452 invariant longitudinal expansion and infinite transverse flow [?]. Major steps were  
 453 taken later with the inclusion of finite size and and dynamically generated trans-  
 454 verse size [?, ?], a part of which was done at the University of Jyväskylä. The role  
 455 of hydrodynamics in heavy-ion physics was strengthened when QGP was observed  
 456 to behave like a liquid by RHIC [1].

457     The evolution of a heavy-ion event can be divided into four stages. A schematic  
 458 representation of the evolution of the collisions is shown in Fig. 7. Stage 1 follows  
 459 immediately the collision. This is known as the pre-equilibrium stage. Hydrody-  
 460 namic description is not applicable to this regime because thermal equilibrium is  
 461 not yet reached. The length of this stage is not known but it is assumed to last  
 462 about  $1 \text{ fm}/c$  in proper time  $\tau$ .

463     The second stage is the regime where thermal equilibrium or at least near-  
 464 equilibrium is reached. In this stage hydrodynamics should be applicable if the  
 465 temperature is above the deconfinement temperature [48]. This lasts about  $5 - 10 \text{ fm}/c$  until the temperature of the system sinks low enough for hadronization to

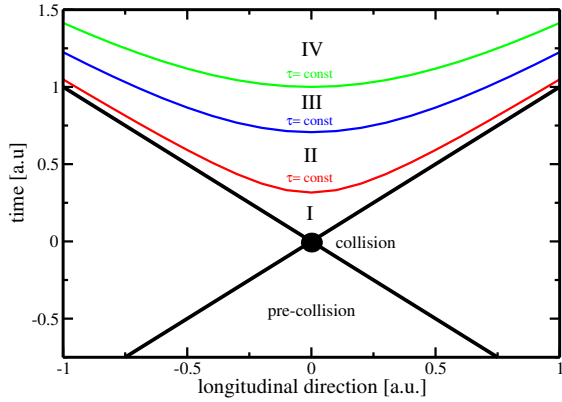


Figure 7: Schematic representation [48] of a heavy-ion collision as the function of time and longitudinal coordinates  $z$ . The various stages of the evolution correspond to proper time  $\tau = \sqrt{t^2 - z^2}$  which is shown as hyperbolic curves separating the different stages.

467 occur. Now the system loses its deconfined, strongly coupled, state and hydrodynamics  
 468 can no longer be used. The third stage is the hadron gas stage where the  
 469 hadrons still interact. This ends when hadron scattering becomes rare and they  
 470 no longer interact. In the final stage hadrons are free streaming and they fly in  
 471 straight lines until they reach the detector.

472 The hydrodynamical approach treats the ensemble of particles as a fluid. It  
 473 uses basic equations from hydrodynamics and thermodynamics but with a few  
 474 modifications to account for the relativistic energies. The calculation is based  
 475 on a collection of differential equations connecting the local thermal variables like  
 476 temperature, pressure etc. to local velocities of the fluid. One also needs equations  
 477 of state that connect the properties of the matter, e.g. temperature and pressure  
 478 to density. Given initial conditions and equations of state the calculation gives the  
 479 time-evolution of the system.

480 At first only ideal hydrodynamics was used. Ideal hydrodynamics does not  
 481 include viscosity but it is a relatively good approximation and it could predict  
 482 phenomena like elliptic flow. For more detailed calculations also viscosity must be  
 483 considered and viscosity itself is an interesting property of QGP.

484 In this thesis I compare my results of identified particle flow to calculations from  
 485 two hydrodynamical models; VISHNU model by Song *et al.* [50] and calculations  
 486 by Niemi *et al.* [51].

## 487 1.4 Flow

488 In a heavy-ion collision the bulk particle production is known as flow. The pro-  
 489 duction is mainly isotropic but a lot of studies including my thesis focus on the  
 490 small anisotropies. After the formation of the QGP, the matter begins to expand  
 491 as it is driven outwards by the strong pressure difference between the center of the  
 492 collision zone and the vacuum outside the collision volume. The pressure-driven  
 493 expansion is transformed into flow of low-momentum particles in the hadroniza-  
 494 tion phase. Since the expansion is mainly isotropic the resulting particle flow is  
 495 isotropic with small anisotropic corrections that are of the order of 10% at most.  
 496 The isotropic part of flow is referred to as radial flow.

497 The transverse momentum spectra  $dN/dp_T$  in heavy-ion collisions is shown

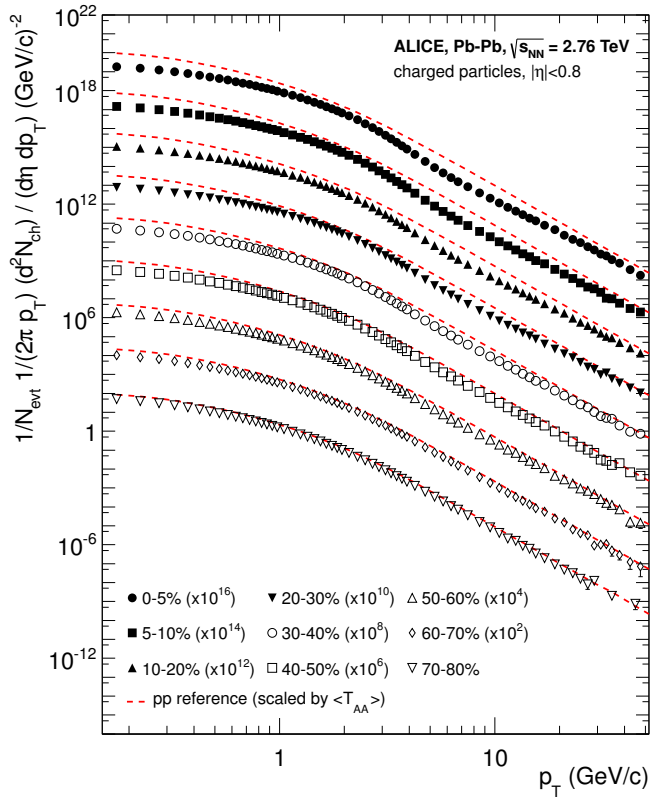


Figure 8: Charged particle spectra measured by ALICE [52] for the 9 centrality classes given in the legend. The distributions are offset by arbitrary factors given in the legend for clarity. The distributions are offset by arbitrary factors given in the legend for clarity. The dashed lines show the proton-proton reference spectra scaled by the nuclear overlap function determined for each centrality class and by the Pb-Pb spectra scaling factors [52].

in Fig. 8. The vast majority of produced particles have small  $p_T$ . The difference between the yield of 1 GeV/c and 4 GeV/c particles is already 2-3 orders of magnitude. Any observables that are integrated over  $p_T$  are therefore dominated by the small momentum particles.

#### 1.4.1 Anisotropic Flow

In a non-central heavy-ion collision the shape of the impact zone is almond-like. In peripheral collisions the impact parameter is large which means a strongly asymmetric overlap region. In a central collision the overlap region is almost symmetric in the transverse plane. In this case the impact parameter is small. Collisions with different impact parameters are shown in Fig. 4.

The pressure gradient is largest in-plane, in the direction of the impact parameter  $b$ , where the distance from high pressure, at the collision center, to low pressure, outside the overlap zone, is smallest. This leads to stronger collective flow into in-plane direction, which in turn results in enhanced thermal emission through a larger effective temperature into this direction, as compared to out-of-plane [3, 4, 53]. The resulting flow is illustrated in Fig. 9. Flow with two maxima in the direction of the reaction plane is called elliptic flow. This is the dominant

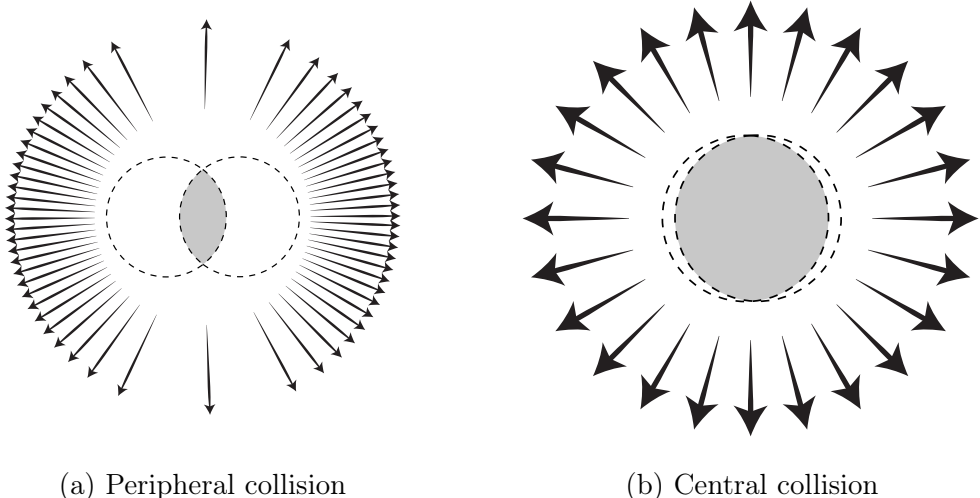


Figure 9: Illustration of flow in momentum space in central and peripheral collisions. The density of the arrows represent the magnitude of flow seen at a large distance from the collision in the corresponding azimuthal direction. In a peripheral collision momentum flow into in-plane direction is strong and flow into out-of-plane direction is weak. In a central collision anisotropy in flow is smaller, but the total yield of particles is larger.

515 part of anisotropic flow. Also more complex flow patterns can be identified. The  
516 most notable of these is the triangular flow, which is mainly due to fluctuations in  
517 the initial conditions.

518 Flow is nowadays usually quantified in the form of a Fourier composition

$$E \frac{d^3N}{dp^3} = \frac{1}{2\pi} \frac{d^2N}{p_T dp_T d\eta} \left( 1 + \sum_{n=1}^{\infty} 2v_n(p_T, \eta) \cos(n(\phi - \Psi_n)) \right), \quad (13)$$

519 where the coefficients  $v_n$  give the relative strengths of different anisotropic flow  
520 components and the overall normalisation gives the strength of radial flow. Elliptic  
521 flow is represented by  $v_2$  and  $v_3$  represents triangular flow. The first coefficient,  
522  $v_1$ , is connected to directed flow. This will however in total be zero because of  
523 momentum conservation. It can be nonzero in some rapidity or momentum regions  
524 but it must be canceled by other regions.

525 The first approaches to quantifying the anisotropy of flow did not use the  
526 Fourier composition. Instead they approached the problem with a classic event  
527 shape analysis using directivity [54] or sphericity [3, 55] to quantify the flow.

528 The first experimental studies of anisotropy were performed at the AGS [56]  
529 in 1993. They noted that the anisotropy of particle production in one region  
530 correlates with the reaction plane angle defined in another region.

531 The first ones to present the Fourier decomposition were Voloshin and Zhang in  
532 1996 [57]. This new approach was useful for detecting different types of anisotropy  
533 in flow, since the different Fourier coefficients give different harmonics in flow.  
534 They also show the relative magnitude of each harmonic compared to radial flow.

535 Some parts of the Fourier composition approach were used for Au-Au collisions  
536 at  $\sqrt{s_{NN}} = 11.4\text{GeV}$  at AGS in 1994 [58]. This analysis still focused on event  
537 shapes but they constructed these shapes using Fourier composition from different  
538 rapidity windows.

#### 539 1.4.2 High $p_T$ Phenomena

540 The measurement of anisotropic flow coefficients can be extended to very high  
541 transverse momenta  $p_T$ . High  $p_T$  measurements of  $v_2$  from CMS [59] are shown  
542 in Fig. 15. For high transverse momenta  $v_2$  values are positive and they decrease  
543 slowly as a function of  $p_T$ . At high transverse momentum the  $v_2$  values don't,  
544 however, represent flow.

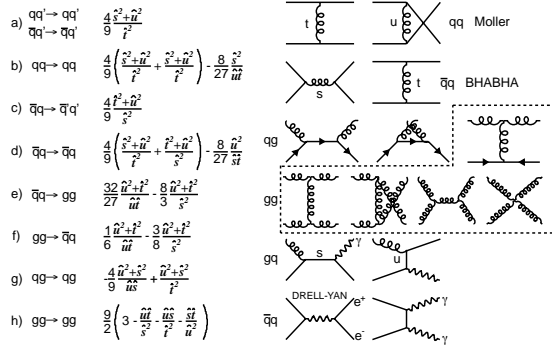


Figure 10: The basic pQCD processes and their quadratic matrix elements

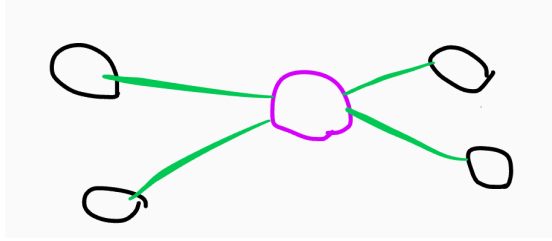


Figure 11: Schematic view of hard scattering process of  $p + p \rightarrow 2 \text{jets}$

## 545 1.5 Hard processes

### 546 1.5.1 pQCD factorization

547 The term Hard Scattering is used in connection with the scattering of two point-like constituents (partons) of colliding nucleons, when the momentum transfer  $Q^2$   
 548 is large ( $Q \gg \Lambda_{\text{QCD}}$ ). Figure ?? shows the incoming partons, quarks or gluons, as  
 549 they exchange a space-like virtual gluon and produce two highly virtual outgoing  
 550 partons. The outgoing partons will eventually fragment into collimated showers of  
 551 partons, referred to as jets

552 Jet fragmentation can be factorised into three components; the parton distribution functions  $f_a, f_b$  that give the probability of getting a parton with momentum fraction  $x$  of the proton, the cross section of the elementary scattering  $ab \rightarrow cd$  (Fig. 10) and the fragmentation functions that give the probability of getting hadron  $h$  from the parton.

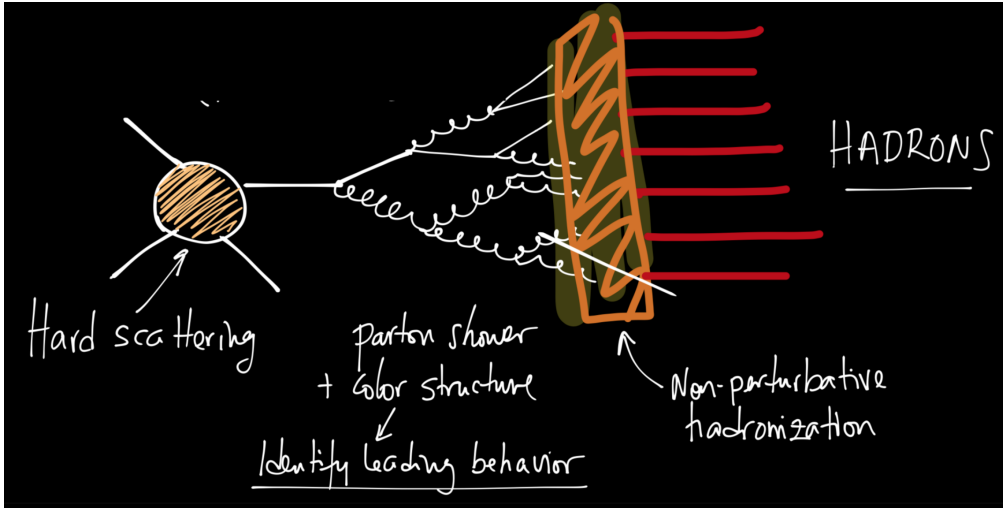


Figure 12: REPLACE FIGURE An illustration of jet showering. The highly virtual parton from the hard scattering will produce a shower of softer partons. When the virtuality is low enough the shower will go through a hadronisation process that produces the hadrons, which will be eventually observed in the detector.

$$\frac{d\sigma_{pp}^h}{dy d^2 p_T} = K \sum_{abcd} \int dx_a dx_b f_a(x_a, Q^2) f_b(x_b, Q^2) \frac{d\sigma}{dt} (ab \rightarrow cd) \frac{D_{h/c}^0}{\pi z_c}$$

$$x_a = \frac{|p_a|}{|p_{proton}|}$$

### 558 Parton Distribution Function

559 Parton Distribution Functions (PDFs) are essential to calculate the scattering cross  
560 section. They are extracted from comprehensive global analysis of experimental  
561 results from a variety of fixed-target and collider experiments. PDFs  $f_a(x)$  give the  
562 differential probability for parton  $a$  to carry momentum fraction  $x$  of the proton  
563 momentum.

564 PDFs cannot be calculated from first principles. In practice the PDFs are  
565 measured in Deeply Inelastic Scattering (DIS) experiments and are extrapolated  
566 to the relevant momentum scales at LHC using the Dokshitzer-Gribov-Lipatov-  
567 Altarelli-Parisi (DGLAP) evolution scheme [?] 14.

$$\mu_F^2 \frac{\partial f_i(x, \mu_F^2)}{\partial \mu_F^2} = \sum_j \frac{\alpha_s(\mu_F)}{2\pi i} \int_x^1 \frac{dz}{z} P_{ij}(z) f_j\left(\frac{x}{z}, \mu_F^2\right), \quad (14)$$

568 where  $\mu_F$  is a factorization scale. The splitting functions  $P_{ij}$  describe a probability to radiate parton  $i$  from parton  $j$  as a function of the momentum fraction  $z$  carried away by the offspring parton.

571 The final component in the factorization, fragmentation functions, describe  
572 the distribution of the fractional momenta of particles radiated from the outgoing  
573 parton. Fragmentation function are given with respect to the momentum fraction  
574  $z$  which is defined as the longitudinal momentum fraction of jet momentum  $p_{\text{jet}}$   
575 carried away by the jet fragment  $p_{\text{part}}$

$$z = \frac{\bar{p}_{\text{part}} \cdot \bar{p}_{\text{jet}}}{p_{\text{jet}}^2} = \frac{p_{\text{part}}}{p_{\text{jet}}} \Big|_{\bar{p}_{\text{part}} \times \bar{p}_{\text{jet}} = 0} \quad (15)$$

576 Fragmentation function  $D(z)$  then gives the average multiplicity  $m$  of jet frag-  
577 ments having  $z > z_0$  [].

$$m(z_0) = \int_{z_0}^1 D(z) dz \Rightarrow m(0) \equiv \langle m \rangle = \int_0^1 D(z) dz \quad (16)$$

578 Because of momentum conservation the sum of all jet fragments must be equal  
579 to the jet momentum, i.e.

$$\sum p_{i,\text{part}} = p_{\text{jet}} \Rightarrow \sum z_i = 1 \Rightarrow \int_0^1 z D(z) dz = 1 \quad (17)$$

580 A natural consequence is that the average momentum fraction is the inverse of  
581 the average multiplicity

$$\langle z \rangle = \frac{\int_0^1 z D(z)}{\int_0^1 D(z)} = \frac{1}{\langle m \rangle} \quad (18)$$

### 582 1.5.2 Jet hadronisation

583 When the parton shower reaches a scale close to  $\Lambda_{\text{QCD}}$ , the perturbative descrip-  
584 tion is no longer valid. Thus the hadronisation stage must be described in a  
585 non-perturbative manner. One simple scenario that is used in several theory calcu-  
586 lations is the so-called local parton-hadron duality [?]. In the local parton-hadron  
587 duality hypothesis it is assumed that there exists a low virtuality scale  $Q_0$  in which  
588 the hadronisation happens, that is independent of the scale of the primary hard  
589 process. At this scale the partons are transformed into hadrons, assuming that the  
590 flow of momentum and quantum numbers for the hadrons can be directly obtained  
591 from those of partons introducing only small normalising constants.

592 Hadronisation is assumed to be universal, i.e. it shouldn't depend on the  
593 collision energy or system.

594 **Lund string model**

595 One common implementation in MC generators is the Lund string fragmentation  
596 algorithm [?]. The string model is based on the fact that in QCD linear confinement  
597 is expected over large distances [?]. This can be modelled by imagining a colour  
598 flux tube being stretched between the outgoing partons. The left side of Fig. 13  
599 illustrates this point for a  $q\bar{q}$ -pair. The tube is assumed to have a uniform fixed  
600 transverse size of about 1 fm along its length, which leads to a linearly rising  
601 potential  $V(r) = \kappa r$ , where the string constant  $\kappa$  describes the amount of energy  
602 per unit length. A value of  $\kappa \approx 1\text{GeV}/\text{fm} \approx 0.2\text{GeV}^2$  can be obtained from hadron  
603 mass spectroscopy.

604 The evolution of string fragmentation is illustrated schematically on the right  
605 side of Fig. 13. This figure is drawn in a light cone presentation, so the initial  
606 quark and antiquark are going to separate directions at the speed of light, which  
607 assumes them as massless. The string between them, illustrated in the figure by  
608 the red line, stretches until its potential energy becomes high enough that it can  
609 break, forming a new quark-antiquark pair. If the original pair was  $q\bar{q}$  and the  
610 new pair  $q'\bar{q}'$ , now two new pairs  $q\bar{q}'$  and  $q'\bar{q}$  have formed. As these particles  
611 are also moving away from each other, the strings between them can stretch and  
612 break, creating yet more pairs. The process continues until the invariant mass of  
613 the system connected by the string becomes small enough and a final state meson  
614 is formed.

615 To mathematically model the string one can use a massless relativistic string  
616 with no transverse degrees of freedom. The gluons are represented as energy and  
617 momentum carrying kinks on the string with incoherent sums of one colour charge  
618 and one anticolour charge. When this string breaks, it is classically required that  
619 the created quark and antiquark are produced at a certain distance if they are to  
620 have any mass or transverse momentum. However, taking into account quantum  
621 mechanics, the pair must be created at one point and then tunnel out to the  
622 classically allowed region. Thus the probability to create a new quark-antiquark  
623 pair becomes proportional to the tunnelling probability [?].

$$P_{\text{tunnelling}} \propto \exp\left(\frac{-\pi m_\perp^2}{\kappa}\right) = \exp\left(\frac{-\pi m^2}{\kappa}\right) \left(\frac{-\pi p_\perp^2}{\kappa}\right), \quad (19)$$

624 where the transverse mass  $m_\perp$  is defined as  $m_\perp^2 = m^2 + p_\perp^2$ . The transverse  
625 momentum is now defined to be transverse to the string axis. This formula gives  
626 flavour-independent Gaussian  $p_\perp$ -distribution for the created  $q\bar{q}$  pairs.

627 As explained above the string fragmentation would only produce mesons in  
628 the final state, but we know that also baryons are created in the process. In the  
629 string fragmentation model baryon production is included by adding a probability  
630 that a diquark-antidiquark pair is created instead of a quark-antiquark pair when

631 a string breaks.

632 The kinematics of each string breaking are determined iteratively. Since there  
633 is no natural ordering, the string breaking can be considered in any order and  
634 the answer obtained must be the same. One can start from the q leg and work  
635 one's way to the  $\bar{q}$  leg, or vice versa. This give a left-right symmetry of the  
636 string fragmentation. In the Lund model this is taken into account by defining a  
637 symmetric fragmentation function

$$f(z) \propto \frac{1}{z} (1-z)^a \exp\left(-\frac{bm_{\perp}^2}{z}\right) \quad (20)$$

638 to break the string into a hadron and a remainder system. In the function  $z$  is  
639 the fraction of light-cone momentum  $p^+$  given to the hadron in the string breaking,  
640  $m_{\perp}$  is the transverse mass of the hadron and  $a$  and  $b$  are tuneable parameters of  
641 the model. For heavy quarks this has to be modified as

$$f(z) \propto \frac{1}{z^{1+bm_Q^2}} (1-z)^a \exp\left(-\frac{bm_{\perp}^2}{z}\right) \quad (21)$$

642 The process can be thought as follows: first start from the q-leg of a  $q\bar{q}$  system  
643 and choose to consider the breaking to new  $q'\bar{q}'$  pair closest to this leg. Now the  
644 breaking will produce a hadron  $q\bar{q}'$  and a remainder system spanning from  $q'\bar{q}$ .  
645 Then the process is continued until the  $\bar{q}$ -leg is reached. A small detail here is  
646 that in equation (20) it is assumed that the mass of the remainder system is large.  
647 Thus some patching up is needed for the last two hadrons coming from a string.  
648 The patching up is done such that the place where it happens looks as closely like  
649 any other string break as possible.

650 One additional possibility one must consider is that a string can have such a  
651 low mass that it cannot break at all. In this case a single hadron is generated out  
652 of the string and if necessary energy and momentum are exchanged with other  
653 partons in the event.

654 After all the hadrons are produced, the short-lived ones can still decay before  
655 the set of final state particles in the simulation is obtained []

## 656 Cluster model

657 Instead of a string model HERWIG [] uses a cluster model [?] for hadronisation.  
658 The model is based on the preconfinement property of parton showers, i.e. the  
659 colour structure of the shower at any evolution scale  $Q_0$  is such that colour singlet  
660 combinations of partons can be formed with an asymptotically universal invariant  
661 mass distribution. The invariant mass does not depend on the initial hard process  
662 scale  $Q$ , but only on  $Q_0$  and the QCD scale  $\Lambda_{\text{QCD}}$ , when  $Q \gg Q_0$ .

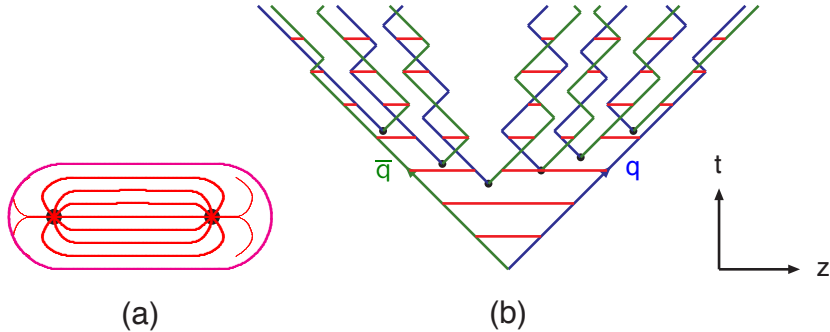


Figure 13: (a) A flux tube spanned between a quark and an antiquark. (b) The motion and breakup of a string system, with the two transverse degrees of freedom suppressed (diagonal lines are (anti)quarks, horizontal ones snapshots of the string field). [?]

663 The cluster model starts from transforming all gluons non-perturbatively into  
 664  $q\bar{q}$  pairs, which requires that the gluons get a mass, which must be at least twice  
 665 the lightest quark mass. After the gluons are transformed into quarks, the adjacent  
 666 colour lines can be clustered together to colour singlet states with mesonic quantum  
 667 numbers. The momentum of these clusters is defined to be the sum of the momenta  
 668 of the clustering partons. According to preconfinement, the mass distribution of  
 669 these clusters is independent of the details of the hard scattering. Additionally the  
 670 clusters can be regarded as highly excited hadron resonances and decayed into the  
 671 final state hadrons.

672 Some of these initial clusters are too heavy to reasonably describe an excited  
 673 state of a hadron. These must be split before they are allowed to decay. The  
 674 cluster  $C$  is split if its mass fulfills the condition ||

$$M_C^p \geq M_{\max}^p + (m_1 + m_2)^p, \quad (22)$$

675 where  $m_{1,2}$  are the masses of the constituents partons of the cluster and  $M_{\max}$   
 676 and  $p$  are the main parameters of the model. These have to be chosen separately  
 677 for clusters containing light, charmed and bottom quarks. When a cluster is split,  
 678 a pair of light quarks is generated from the vacuum and two new clusters are made,  
 679 both containing one quark from the original cluster and one from the newly gen-  
 680 erated pair. The splitting is continued until no clusters with masses  $M_C$  fulfilling  
 681 the equation ?? remains.

682 When clusters are light enough, they decay into final state hadrons. If  
 683 the mass of the cluster is high enough for decaying into a baryon-antibaryon pair,  
 684 there is a parameter deciding whether the cluster undergoes mesonic or baryonic  
 685 decay. For a mesonic decay a quark-antiquark pair is created from the vacuum

and for the baryonic decay a diquark-antidiquark pair is made. Then the exact decay products are chosen and the cluster decays isotropically in the rest frame of the cluster. If there are partons produced in the perturbative phase involved in the decay, they retain their original direction in the cluster rest frame, up to some Gaussian smearing. If the cluster mass is too low to decay into a pair of mesons, it decays into the lightest possible hadron and some energy and momentum is exchanged with the adjacent clusters. At the end we are left with the final state hadrons, some of which might still decay until the end of the simulation if they are very short-lived. []

### 1.5.3 Jet energy loss

"Jet quenching in heavy-ion collisions evolves multi-scale problems [?, ?]. The elementary scattering and the subsequent branching process down to non-perturbative scales are dominated by hard scales in the vacuum as well as in the medium. Soft scales, of the order of the temperature of the medium, characterise the interactions of soft partons produced in the shower with the QGP. Soft scales also rule hadronisation, which is expected to take place in vacuum for sufficiently energetic probes, even though some modifications can persist from modifications of color flow [?, ?, ?]. Understanding the contributions from the different processes to the jet shower evolution in medium and their scale dependence is crucial to constrain the dynamics of jet energy loss in the expending medium, the role of colour coherence [?], and fundamental medium properties like temperature dependent transport coefficient [?, ?]. "

High momentum particles are very rare and they are only produced in the initial collisions. After they are created they escape the medium before a thermal equilibrium is reached. Thus they are not part of the pressure-driven collective expansion. Instead high momentum yield is suppressed because of energy loss in the medium. When propagating through the medium these partons lose energy as they pass through the medium. This is referred to as jet quenching. Jet quenching depends on the path lengths through the medium. Thus anisotropy in this region is mainly dependent on the collision geometry and density of medium.

The energy loss of partons in medium is mainly due to QCD bremsstrahlung and to elastic scatterings between the parton and the medium.

The radiative energy loss mechanism is given in terms of the transport coefficient  $\langle \hat{q} \rangle$ , which describes the average momentum transfer between the medium and parton [?]. The exact definition of this depends on the theoretical formalism used to describe the energy loss mechanism.

Many of the energy loss models exploit the analogy between the QCD interaction of parton propagating through the colored medium and the QED energy loss of electron propagating through material. An electron propagating through

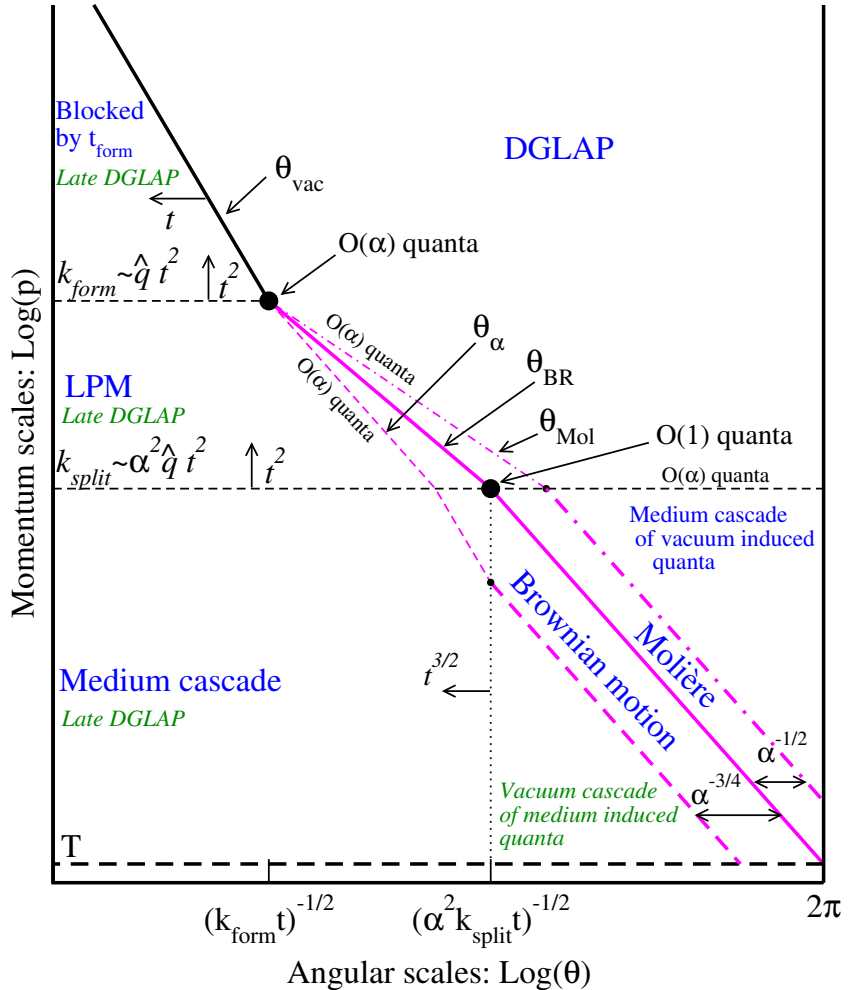


Figure 14: Parametrically accurate picture of how a medium-modified parton cascade fills the phase space. At time  $t$ , quanta can be formed up to momentum scale  $k_{\text{form}}$  and they are formed with  $O(1)$  probability per  $\log p$  at lower scale  $k_{\text{split}}$ . Quanta below  $k_{\text{split}}$  split further and their energy cascades to the thermal scale  $T$  in less than an epoch  $t$ . Transverse Brownian motion moves quanta up to the angle  $\theta_{\text{BR}}(p)$  denoted by the thick purple line. The Molière region at larger  $\theta$  is dominated by rare large angle scattering. At even larger angle, there are  $O(\alpha_s)$  quanta per double logarithmic phase space from DGLAP ‘vacuum’ radiation, and for momenta below  $k_{\text{split}}$  these cascade within time  $t$  to  $T$ . After the jet escapes the medium, the jet and the emitted fragments will undergo vacuum radiation. This late time vacuum radiation emitted by the original parton dominates at sufficiently small  $\log \theta$  (regions marked “late DGLAP” and bounded by  $\theta_{\text{vac}}$  and  $\theta_\alpha$ ), whereas the late time radiation of the fragments dominates in the region denoted by “Vacuum cascade of the medium induced quanta”. [?].

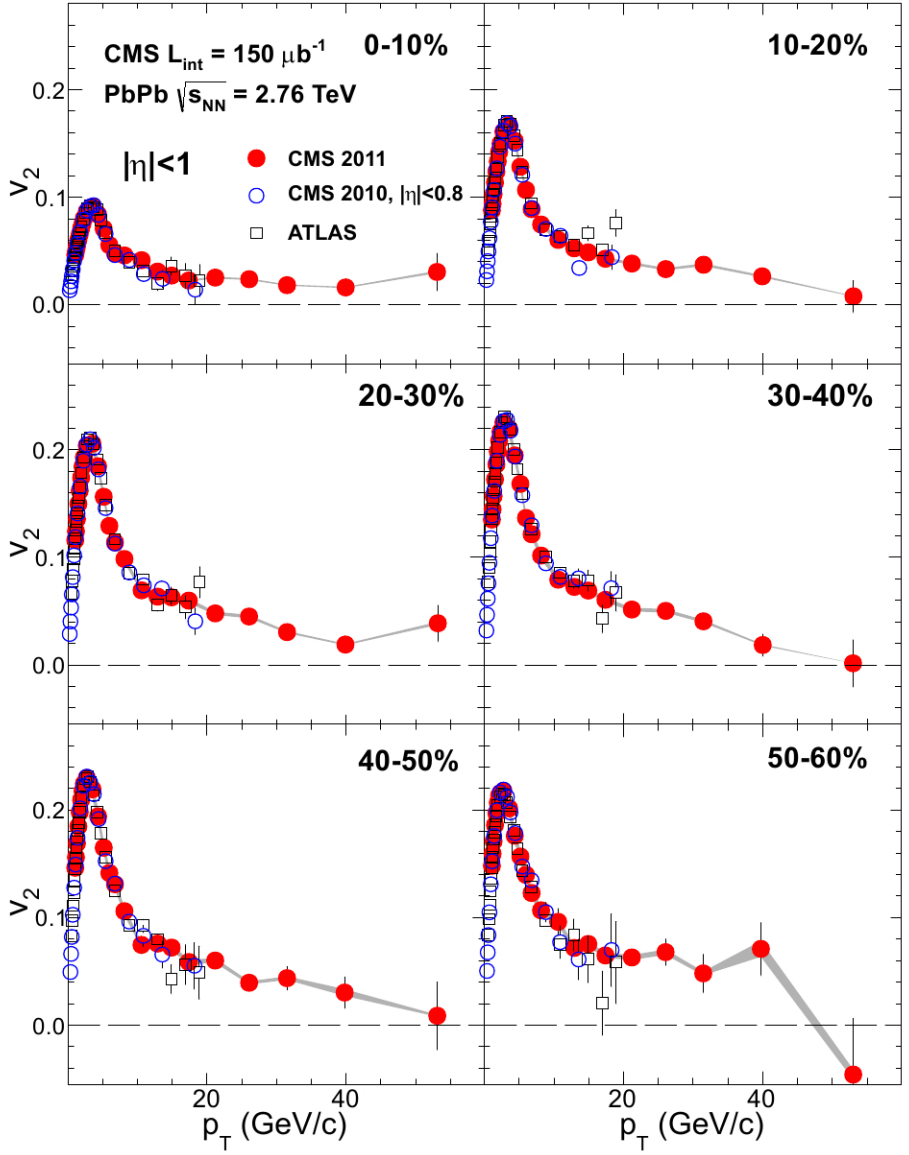


Figure 15: Elliptic flow,  $v_2$ , as a function of the charged particle transverse momentum from 1 to 60  $\text{GeV}/c$  with  $|\eta| < 1$  for six centrality ranges in Pb-Pb collisions at  $\sqrt{s_{NN}} = 2.76 \text{ TeV}$ , measured by the CMS experiment. [59].

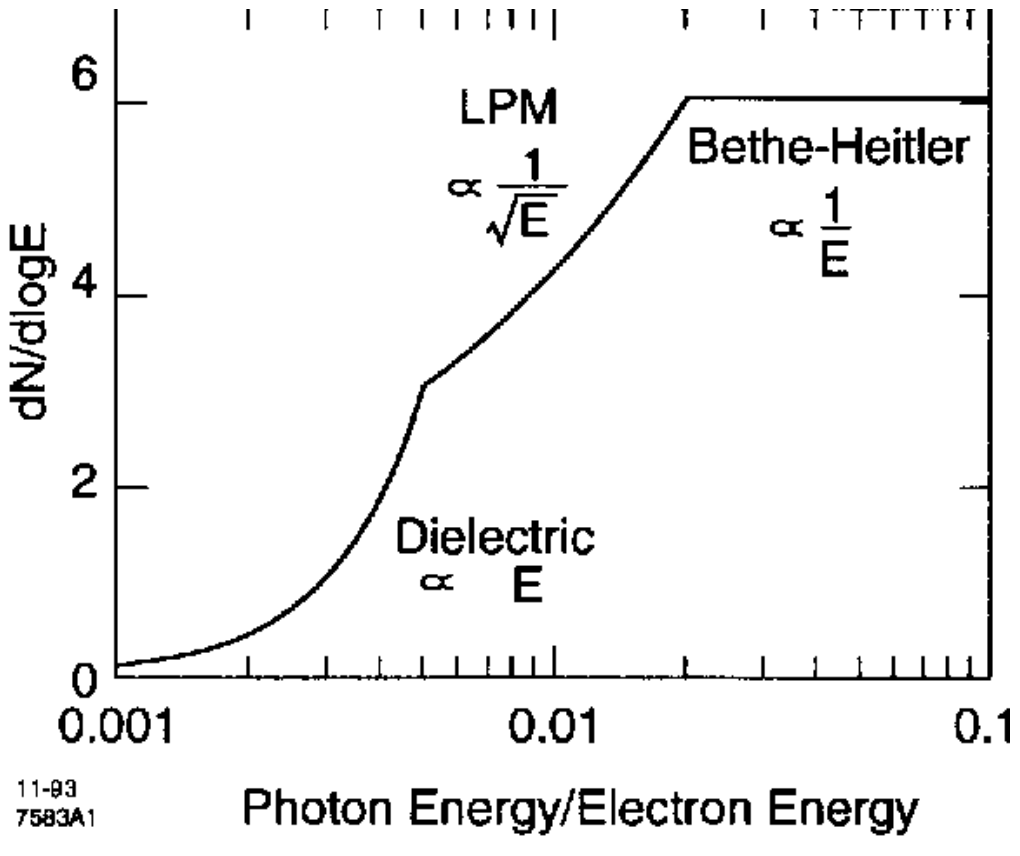


Figure 16: The expected bremsstrahlung spectrum for a electron propagating through material. [?].

matter loses its energy by photon Bremsstrahlung radiation. In the simplest case, each individual scattering center results in a single emission of a photon. This is known as the Bethe-Heitler regime [?]. The energy spectrum of radiated photons  $dN/dE$  is, in this case, proportional to  $1/E$ . However, the Bremsstrahlung photon, can be radiated only when the distance between the scattering centers is larger than the formation length. In the limit, when the scattering centers are closer than the formation length, the Bremsstrahlung process is suppressed. This phenomenon is known as the Landau-Pomeranchuk-Migdal (LPM) [?, ?] suppression. The radiated spectrum in this regime is proportional to  $1/\sqrt{E}$ .

Lower energy photons are further suppressed by the destructive interference leading to the suppression of Bremsstrahlung photons of  $E < \gamma\omega_p$ , where  $\omega_p$  is the plasma frequency of the radiator. This is known as Dielectric suppression. The photon energy distribution in this regime is proportional to the energy of the photon. A schematic view of the effect of these three regimes is shown in Fig. 16.

The simplest energy loss process is elastic QCD scattering off the medium par-

<sup>740</sup> tons. In elastic scatterings the recoil energy of the scattered partons are absorbed  
<sup>741</sup> by the thermal medium, which reduces the energy of the initial parton. The mean  
<sup>742</sup> energy loss from elastic scatterings can be estimated by

$$\langle \Delta E \rangle_{\text{el}} = \sigma \rho L \langle E \rangle_{\text{scatt}} \propto L, \quad (23)$$

<sup>743</sup> where  $\sigma$  is the interaction cross section and  $\langle E \rangle_{\text{scatt}}$  is the mean energy transfer  
<sup>744</sup> of one individual scattering [60]. This assumption holds if the mean energy is  
<sup>745</sup> independent of the total energy of the parton ( $E$ ). The transport coefficient of  
<sup>746</sup> elastic scattering,  $\langle \hat{q}_{\text{el}} \rangle = \langle \Delta E \rangle / L$ , is defined as the mean energy los per unit path  
<sup>747</sup> length.

<sup>748</sup> Another energy loss mechanism is medium-induced radiation. In QCD this  
<sup>749</sup> radiation is mainly due to the elementary splitting processes,  $q \rightarrow qg_r$  and  $g \rightarrow gg_r$ .  
<sup>750</sup> Assuming that the parton is moving with the speed of light radiation energy loss  
<sup>751</sup> can be estimated by

$$\langle \Delta E \rangle_{\text{rad}} \propto T^3 L^2, \quad (24)$$

<sup>752</sup> where  $L$  is the length of the medium and  $T$  is its temperature [61]. The differ-  
<sup>753</sup> ent exponents of  $L$  in equations 22 and 23 indicate that radiative energy loss is  
<sup>754</sup> dominant over elastic energy loss.

<sup>755</sup> There are several models that attempt to describe the nature of the energy loss  
<sup>756</sup> mechanism. The most used models can be divided into four formalisms.

<sup>757</sup> In the Gyulassy-Levai-Vitev (GLV) [62] opacity expansion model the radiative  
<sup>758</sup> energy loss is consiered on a few scattering centers  $N_{\text{scatt}}$ . The radiated gluon  
<sup>759</sup> is constructed by pQCD calculation as summing up the relevant scattering am-  
<sup>760</sup> plitudes in terms of the number of scatterings. Another approach into opacity  
<sup>761</sup> expansion is the ASW model by Armesto, Salgado and Wiedermann [63].

<sup>762</sup> Thermal effective theory formulation by Arnold, Moore and Yaffe (AMY) [64]  
<sup>763</sup> uses dynamical scattering centers. It is based on leading order pQCD hard thermal  
<sup>764</sup> loop effective field theory. This model assumes that because of the high temper-  
<sup>765</sup> ature of the plasma the strong coupling constant can be treated as small. The  
<sup>766</sup> parton propagating through the medium will lose energy from soft scatterings and  
<sup>767</sup> hard scatterings.

<sup>768</sup> The above models calculate the energy loss while the parton propagates through  
<sup>769</sup> the medium, focusing on the pQCD part. The higher twist (HT) approach by Wang  
<sup>770</sup> and Guo [65] implements the energy loss mechanism in the energy scale evolution  
<sup>771</sup> of the fragmentation functions.

<sup>772</sup> The last category is formed by the Monte Carlo methods. The PYTHIA event  
<sup>773</sup> generator [66] is widely used in high-energy particle physics. Two Monte Carlo  
<sup>774</sup> models based on PYTHIA describing the energy loss mechanism are PYQUEN [67]

<sup>775</sup> and Q-Pythia [68]. Other Monte Carlo models include JEWEL [69] and Ya-  
<sup>776</sup> JEM [70].

<sup>777</sup> Jet quenching in heavy-ion collisions is usually quantized with the nuclear  
<sup>778</sup> modification factor  $R_{AA}$ , which is defined as

$$R_{AA}(p_T) = \frac{(1/N_{AA}^{evt}) dN^{AA}/dp_T}{\langle N_{coll} \rangle (1/N_{pp}^{evt}) dN^{pp}/dp_T} \quad (25)$$

<sup>779</sup> where  $dN^{AA}/dp_T$  and  $dN^{pp}/dp_T$  are the yields in heavy-ion and proton-proton  
<sup>780</sup> collisions, respectively and  $\langle N_{coll} \rangle$  is the average number of binary nucleon-nucleon  
<sup>781</sup> collisions in one heavy-ion event. The number of binary collisions can be calculated  
<sup>782</sup> from the Glauber model as shown in Sec. 1.3.2. From the point of view of direct  
<sup>783</sup> production a heavy-ion collision can be estimated relatively well to be only a series  
<sup>784</sup> of proton-proton collisions.

<sup>785</sup> If the medium has no effect on high  $p_T$  particles the nuclear modification factor  
<sup>786</sup> should be 1. At RHIC and LHC this has been observed to be as low as 0.2 because  
<sup>787</sup> of jet quenching. Measurements of  $R_{AA}$  from different sources are shown in Fig. 17

<sup>788</sup> The nuclear modification factor can also be used to quantify anisotropy. In  
<sup>789</sup> the study of anisotropy  $R_{AA}$  in-plane and out-of-plane can be compared. The  
<sup>790</sup> distance traveled through medium is largest out-of-plane which leads to stronger  
<sup>791</sup> suppression in this direction. The nuclear modification factor as a function of  
<sup>792</sup>  $\Delta\phi = \phi - \psi_n$  is given by

$$\begin{aligned} R_{AA}(\Delta\phi, p_T) &= \frac{(1/N_{AA}^{evt}) d^2N^{AA}/d\Delta\phi dp_T}{\langle N_{coll} \rangle (1/N_{pp}^{evt}) dN^{pp}/dp_T} \approx \frac{dN^{AA}/dp_T (1 + 2 \cdot v_2 \cos(2\Delta\phi))}{\langle N_{coll} \rangle dN^{pp}/dp_T} \\ &= R_{AA}^{incl}(p_T) (1 + 2 \cdot v_2 \cos(2\Delta\phi)). \end{aligned} \quad (26)$$

<sup>793</sup> The yield of proton-proton collisions is independent of the reaction plane and  
<sup>794</sup> the yield in heavy-ion collisions is modulated by the second harmonics. In Eq. (25)  
<sup>795</sup>  $R_{AA}$  is approximated only up to the second harmonics. From Eq. (25) it follows  
<sup>796</sup> that

$$\frac{R_{AA}(0, p_T) - R_{AA}(\pi/2, p_T)}{R_{AA}^{incl}(p_T)} \approx \frac{R_{AA}^{incl}(p_T) (1 + 2 \cdot v_2 - (1 - 2 \cdot v_2))}{R_{AA}^{incl}(p_T)} = 4 \cdot v_2 \quad (27)$$

<sup>797</sup> The observed  $R_{AA}(\Delta\phi, p_T)$  from PHENIX measurements in Au-Au collisions at  
<sup>798</sup>  $\sqrt{s} = 200\text{GeV}$  [82] is compared to  $R_{AA}$  using  $v_2$  via Eq. (25) in Fig. 18. They  
<sup>799</sup> agree very well within the statistical errors for all centrality and  $p_T$  bins.

<sup>800</sup> At high- $p_T$ , the pQCD processes are dominant, hence the  $v_n$  (or  $R_{AA}(\Delta\phi, p_T)$ )  
<sup>801</sup> characterize the pathlength-dependence of the energy loss process.

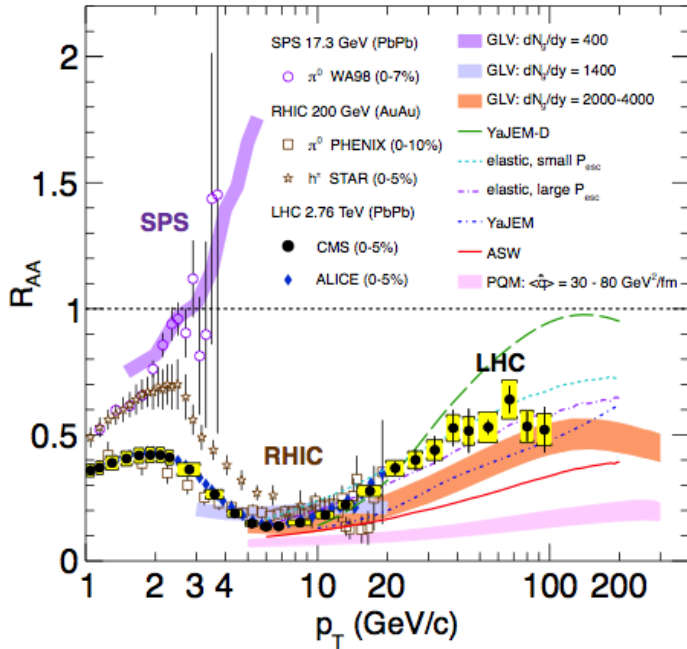


Figure 17: Measurements of the nuclear modification factor  $R_{AA}$  in central heavy-ion collisions at three different center-of-mass energies, as a function of  $p_T$ , for neutral pions ( $\pi^0$ ), charged hadrons ( $h^\pm$ ), and charged particles [71–75], compared to several theoretical predictions [32, 76–80]. The error bars on the points are the statistical uncertainties, and the yellow boxes around the CMS points are the systematic uncertainties. The bands for several of the theoretical calculations represent their uncertainties [81].

Jet quenching is not the only high  $p_T$  phenomenon studied in heavy-ion collisions. Another property is jet fragmentation. The high momentum parton created in the initial collision fragments into a number of partons with smaller  $p_T$ . Jet fragmentation occurs also in proton-proton collisions in the vacuum, but it can be modified due to the presence of the medium. In order to study the jet fragmentation function ( $D(z)$ , where  $z = p_T^h/p_T^{part}$ ) modification due the medium, we use the two-particle correlations. The particle yield can be extracted from the correlation function. The background from the flow processes is correlated and needs to be subtracted to get the particle yield associated only with the jet. The ratio of the jet yields in Au-Au and p-p collision  $I_{AA} = Y^{Au+Au}/Y^{p+p}$  characterizes the jet fragmentation modification [83].  $I_{AA}$  probes the interplay between the parton production spectrum, the relative importance of quark-quark, gluon-gluon and quark-gluon final states, and energy loss in the medium.

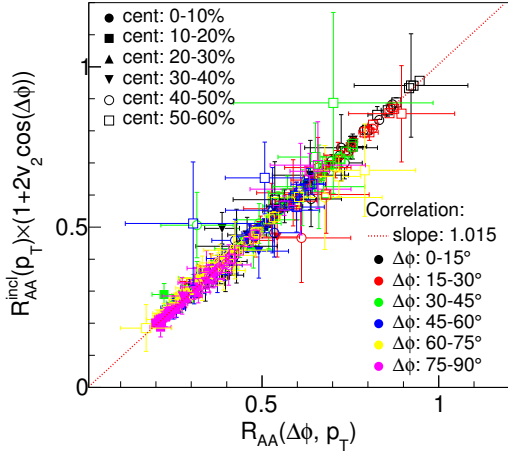


Figure 18: A comparison between observed  $R_{AA}(\Delta\phi, p_T)$  and  $R_{AA}$  using  $v_2$  from PHENIX measurements of Au-Au collisions at  $\sqrt{s} = 200\text{GeV}$ . On the X-axis is the measured  $R_{AA}(\Delta\phi, p_T)$ . On the y-axis is the inclusive  $R_{AA}$  multiplied by  $1 + 2v_2 \cos(\Delta\phi)$  [82].

#### 815 1.5.4 Monte Carlo Implementations

### 816 1.6 QGP in Small systems

817 After the existence of QGP in heavy ion collisions has been established, attention  
 818 has been turned to small systems. Proton-proton (pp) and proton-Lead (pPb)  
 819 collisions have been studied at LHC and RHIC has studied a host of different  
 820 collision systems; namely proton-Gold (pAu), deuteron-Gold (dAu) and Helium<sup>3</sup>-  
 821 Gold (He<sup>3</sup>Au) collisions starting in 2000.

822 Already before the era of modern colliders, collective behaviour in proton-  
 823 proton collisions was considered by names like Heisenberg, Fermi and Bjorken. [84]  
 824 Eventually there were some experimental searches of QGP in pp and  $p\bar{p}$  collisions  
 825 in E735 at Tevatron [85] and MiniMAX [86]. However no conclusive evidence was  
 826 found.

827 In the early years of RHIC these small systems were mostly considered as con-  
 828 trol measurement, for example in constraining nuclear modified parton distribution  
 829 functions (nPDFs) that determine the initial gluon distributions that determine  
 830 the first epoch of heavy ion collisions [87, 88].

831 In 2010 ultrahigh-multiplicity pp collisions were studied at CMS. The study  
 832 found that particles had a weak but clear preference to be emitted along a common  
 833 transverse  $\phi$  angle across all rapidities [89]. This seemed like behaviour were sim-

ilar to AA collisions, but it was argued that it could as well come from momentum correlations present in the earliest moments of the collision.

In 2012 LHC ran its first pPb data taking period. Around the same time dAu data was reexamined at RHIC. Now it was revealed that most of the flow signatures attributed to hydrodynamic expansion in AA collisions also existed in smaller systems.

-Sub nucleonic structure needed to describe intial conditions in pA, pp

### 1.6.1 Collective phenomena

The most rugged analysis of collective behaviour concerns the two (or more) particle correlations, often parametrised via the relative azimuthal angle and pseudorapidity differences,  $\Delta\phi$  and  $\Delta\eta$  respectively. Figure 20 shows two-particle correlations measurements in PbPb, pPb and pp collisions at the LHC. In PbPb collisions long-range correlations dominate over short-range phenomena. This shows in the two ridges at  $\Delta\phi = 0$  and  $\Delta\phi = \pi$ . At  $\Delta\phi \approx \Delta\eta \approx 0$ , there is a peak coming from single jet fragmentation. Since the away-side jet can be spread out in  $\Delta\eta$ , this contribution disappears when compared to the flow contribution at the away side ridge. In pPb, and pp the near side peak is more distinguished and the away-side jet contribution starts to show. Still, one can see long-range correlations that seem like flow-like collective behaviour in both systems.

In addition to the two particle correlations, correlations have been observed in the form of  $v_n$  coefficients both at LHC and at RHIC. The results have also been described with hydrodynamical models, although the applicability of said models is questionable, because of the large Reynolds numbers in small systems. Figure

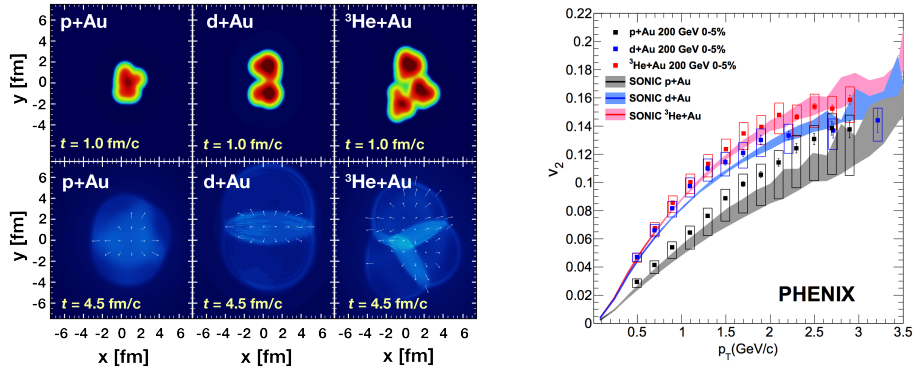


Figure 19: Calculations of the intial energy density in small collision systems at RHIC and the resulting hydrodynamic evolution.

19 shows results for  $v_2$  in different collisions systems at RHIC as measured by PHENIX. These different systems provide also different initial geometries. dAu collisions naturally have an ellipsoidal form, while a He3 collision has a triangular form and thus produces larger triangular flow,  $v_3$  components.

Other observations that produce flow-like results include mass ordered  $v_2$  coefficients and higher order harmonics coming from fluctuations in the initial geometry. Thus all the major collective flow phenomena observed in heavy-ion collisions have been also identified in small systems.

One open question is identifying the point the point, where flow-like correlations end. The question has proved challenging since low multiplicity events are dominated by non-flow phenomena. This makes observations in low multiplicity events model/method dependant. Different methods assess non-flow contributions differently. Thus some methods fail to observe a signal in cases, where others do and it is unclear whether this is true collective motion or it comes from non-flow contributions.

### 1.6.2 Absence of jet quenching

In A+A collisions, an important confirmation of the standard model comes from the energy loss of high  $p_T$  partons traversing the medium, referred to as jet quenching [90–92]. In 2003 the jet quenching effect was observed to disappear in d+Au collisions. This was taken as an indication that no QGP was created. Similarly at LHC no jet modification has been observed in pPb collisions. Fig. 21 shows the nuclear modification factor  $R_{pA}$  in pPb collisions as measured at the LHC.

The lack of jet modification seems surprising considering the multitude of flow observations supporting the existence of QGP in small systems. One possible explanation is simply the size of medium. In PbPb collision partons traversing through the medium lose energy to the medium. If the medium is very small there is limited time for interaction with the medium.

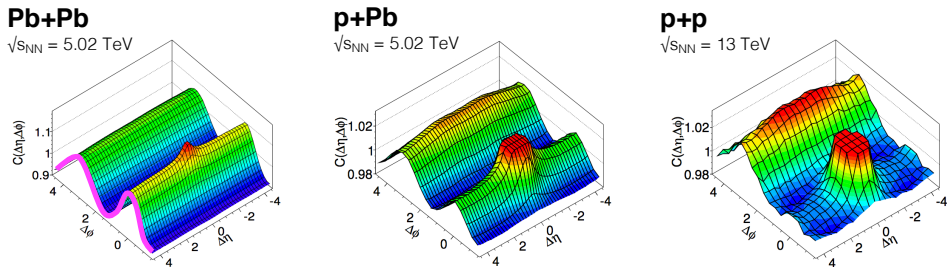


Figure 20: Two-particle correlation results in PbPb, pPb, and pp collisions at the LHC [].

884 Calculations indicate that there should be modification in the most central  
 885 pPb collisions, but selecting these in the analysis is complicated. In PbPb collisions  
 886 most of the particle production comes from the medium and thus the total  
 887 multiplicity is a good indicator of centrality. In pPb collisions, however the total  
 888 multiplicity is smaller and is more strongly influenced by jet phenomena. Events  
 889 with jets have naturally larger multiplicities and are more likely to be classified as  
 890 central events.

891 So far the only observable indicative of jet quenching in pPb collisions is the  
 892 high  $p_T v_2$ . In heavy-ion collisions this is not explained by hydrodynamics. Instead  
 893 it is assumed to come from jet quenching with different path lengths through the  
 894 medium in different directions. In Fig.21 ATLAS and CMS measurements of  $v_2$  in  
 895 pPb and PbPb collisions are shown. The pPb results seem to follow a very similar  
 896 pattern. But

Table 1: Summary of observations in small system

Observable	PbPb	pPb	pp
Jet RpA/RAA	Modified	No modification	-
Hadron RpA/RAA	Modified	No modification	-
Heavy flavors			
Jet shape	Broadening	No observations	-
Two-particle correlations	Ridge	Ridge	Ridge
$v_2$	Observed	Observed	Observed
Mass ordered flow			
Higher ordered harmonics			
High $p_T v_2$	Observed	Maybe	-

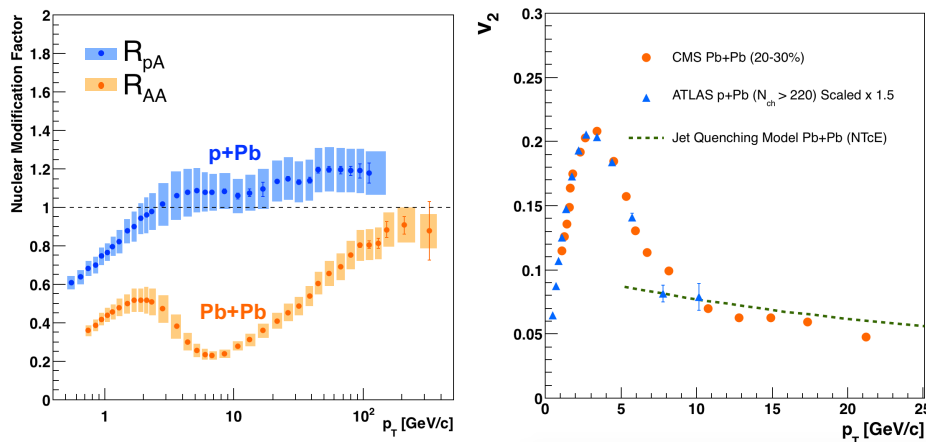


Figure 21: RpA in proton-lead collisions

## 897 2 Experimental setup and data samples

898 The  $\sqrt{s_{\text{NN}}} = 5.02$  TeV p–Pb ( $1.3 \cdot 10^8$  events,  $\mathcal{L}_{\text{int}} = 620 \text{ nb}^{-1}$ ) collisions were  
899 recorded in 2013 by the ALICE detector [93]. The details of the performance of  
900 the ALICE detector during LHC Run 1 (2009–2013) are presented in Ref. [94].

901 The analysis uses charged tracks that are reconstructed with the Inner Tracking  
902 System (ITS) [95] and the Time Projection Chamber (TPC) [96]. These detectors  
903 are located inside the large solenoidal magnet, that provides a homogeneous mag-  
904 netic field of 0.5 T. Tracks within a pseudorapidity range  $|\eta| < 0.9$  over the full  
905 azimuth can be reconstructed. The ITS is made up of the innermost Silicon Pixel  
906 Detector (SPD), the Silicon Drift Detector (SDD) and the outermost Silicon Strip  
907 Detector (SSD). Each of these consists of two layers. The TPC is a cylinder filled  
908 with gas. Gas is ionised along the path of charged particles. Liberated electrons  
909 drift towards the end plates of the cylinder where they are detected. Combining  
910 the information from the ITS and the TPC provides a resolution ranging from 1  
911 to 10 % for charged particles with momenta from 0.15 to 100 GeV/c. For tracks  
912 without the ITS information, the momentum resolution is comparable to that  
913 of ITS+TPC tracks below transverse momentum  $p_T = 10$  GeV/c, but for higher  
914 momenta the resolution reaches 20 % at  $p_T = 50$  GeV/c [94, 97].

915 Neutral particles used in jet reconstruction are reconstructed by the Electro-  
916 magnetic Calorimeter (EMCAL) [98]. The EMCAL covers an area with a range  
917 of  $|\eta| < 0.7$  in pseudorapidity and 100 deg in azimuth. EMCAL is complimented  
918 with the Dijet Calorimeter (DCal) [99] and Photon Spectrometer (PHOS) [100]  
919 that are situated opposite of the EMCAL in azimuth. PHOS covers 70 degrees  
920 in azimuth and  $|\eta| < 0.12$ . The DCal is technologically identical to EMCal. The  
921 DCal coverage spans over 67 degrees in azimuth, but in pseudorapidity the mid  
922 region is occupied by the PHOS. In between PHOS and DCal active volumes, there  
923 is a gap of 10 cm. DCal is fully back-to-back with EMCal.

924 The combination of charged tracks with  $p_T > 0.15$  GeV/c and neutral particles  
925 with  $p_T > 0.30$  GeV/c is used to construct jets.

926 The V0 detector [101] provides the information for event triggering. The V0  
927 detector consists of two scintillator hodoscopes that are located on either side of  
928 the interaction point along the beam direction. It covers the pseudorapidity region  
929  $-3.7 < \eta < -1.7$  (V0C) and  $2.8 < \eta < 5.1$  (V0A). For the 2013 p–Pb collisions  
930 events are required to have signals in both V0A and V0C. This condition is used  
931 later offline to reduce the contamination of the data sample from beam-gas events  
932 by using the timing difference of the signal between the two stations [94].

933 EMCAL is also used to provide the jet trigger used in triggered datasets. EM-  
934 CAL can be used to trigger on single shower deposits or energy deposits integrated  
935 over a larger area. Latter case is used for jet triggers. The EMCAL trigger defini-  
936 tion in the 2013 p–Pb collisions requires an energy deposit of either 10 GeV for the

937 low threshold trigger or 20 GeV for the high threshold trigger in a  $32 \times 32$  patch  
938 size.

939 In p–Pb collisions the tracks are selected following the hybrid approach [102]  
940 which ensures a uniform distribution of tracks as a function of azimuthal angle  
941 ( $\varphi$ ). The momentum resolutions of the two classes of particles are comparable up  
942 to  $p_T \approx 10$  GeV/ $c$ , but after that, tracks without ITS requirements have a worse  
943 resolution [94, 97].

## 944 3 Experimental Details

### 945 3.1 CERN

946 The European Organization for Nuclear Research (CERN) is the largest particle  
947 physics laboratory in the world. CERN was founded in 1954. In 2019 CERN  
948 consists of 22 member states. Additionally CERN has contacts with a number  
949 of associate member states and various individual institutions. Some 12000 vis-  
950 iting scientists from over 600 institutions in over 70 countries come to CERN for  
951 their research. CERN itself is located near Geneva at the border of France and  
952 Switzerland and itself employs about 2500 people.

953 The laboratory includes a series of accelerators, which are used to accelerate  
954 the particle beams used. A schematic view of the complex as of 2019 is shown  
955 in Figure ???. In the framework of this thesis the main component is the Large  
956 Hadron Collider (LHC), the largest collider at CERN. LHC will be discussed in  
957 the chapter in more detail. Other accelerators in the series are used to inject the  
958 particle beam into LHC, but they are also used in itself for various experimental  
959 studies.

960 The second largest accelerator is the super proton synchrotron (SPS). It is final  
961 step before the particle beam is injected into LHC. Commissioned in 1976, it was  
962 the largest accelerator at CERN until the the Large Electron-Positron Collider  
963 (LEP) was finished in 1989. Originally it was used as a proton-antiproton collider  
964 and as such provided the data for the UA1 and UA2 experiments, which resulted in  
965 the discovery of the W and Z bosons. At the moment there are several fixed target  
966 experiments utilising the beam from SPS. These study the structure (COMPASS)  
967 and properties (NA61/SHINE) of hadrons, rare decays of kaons (NA62) and radi-  
968 ation processes in strong electromagnetic fields (NA63). Additionally the AWAKE  
969 and UA9 experiments are used for accelerator research and development.

970 -PS

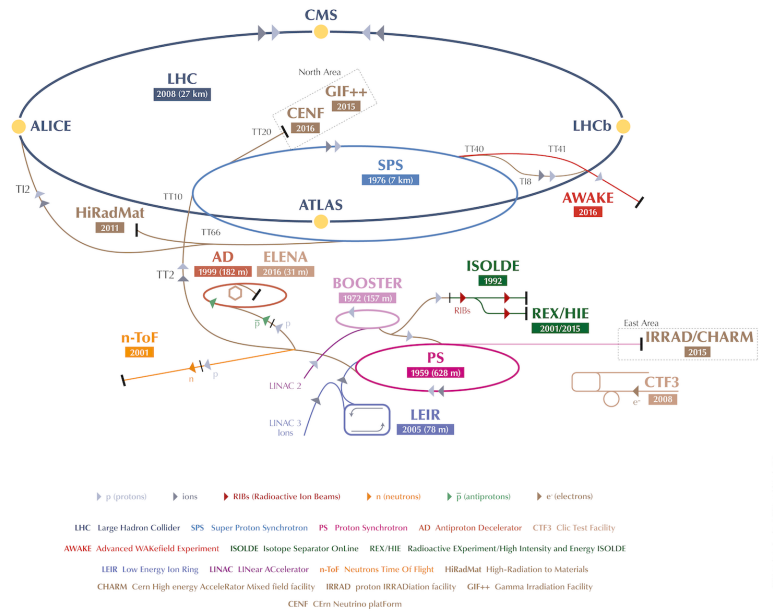


Figure 22: A schematic view of the accelerator complex at CERN. Before particles can be injected into the LHC they require a series of preliminary? acceleterarors. Until 2018 protons start their journey in LINAC2 (Linear Accelerator) and continue through the Booster, Proton Synchrotron (PS) and Super Proton Synchrotron (SPS). Between 2019 and 2020 LINAC2 will be replaced by LINAC4 [?]

## **971 3.2 Large Hadron Collider**

**972** The Large Hadron Collider (LHC) is the largest accelerator at CERN and the  
**973** largest particle collider ever built. The LHC is designed to accelerate protons  
**974** up to an energy of 8 TeV and lead ions up to 2.76 TeV per nucleon [?]. The design  
**975** luminosity of the LHC is  $10^{34} \text{ cm}^{-2} \text{ s}^{-1}$ . In 20xx it achieved a record peak luminosity  
**976** of xxx. For lead beams the design luminosity is xxx. All this is achieved with a  
**977** ring of 26.7 km, that consists of 1232 superconducting dipole magnets that keep  
**978** particles in orbit.

**979** The particles are accelerated through the use of radio-frequency (RF) cavities.  
**980** The RF are build such that the electromagnetic waves become resonant and build  
**981** up inside the cavity. Charges passing through the cavity feel the overall force  
**982** and are pushed forward along the accelerator. As they consist of electromagnetic  
**983** waves, the field in the RF cavity oscillates. Thus particles must enter the cavity at  
**984** the correct phase of oscillation to receive a forward push. When timed correctly,  
**985** the particles will feel zero accelerating voltage when they have exactly the correct  
**986** energy. Particles with higher energies will be decelerated and particles with lower  
**987** energies will be accelerated. This focuses particles in distinct bunches. The RF  
**988** oscillation frequency at the LHC is 400.8 MHz. Thus RF "buckets" are separated  
**989** by 2.5 ns. However only 10 % are actually filled with particles, so the bunch  
**990** spacing in the LHC is 25 ns, at a bunch frequency of 40 MHz.

**991** With 7 TeV proton beams the dipole magnets used to bend the beam must  
**992** produce a magnetic field of 8.33 T. This can be only achieved through making  
**993** the magnets superconducting, which requires cooling them down with helium to a  
**994** temperature of 1.9 K. The 1232 dipole magnets make up roughly 2/3 of the LHC  
**995** circumference. The remaining part is made up of RF cavities, various sensors and  
**996** higher multipole magnets used to keep the beam focused. The most notable of  
**997** these are the 392 quadrupole magnets.

**998** The LHC is divided into octants, where each octant has a distinct function.  
**999** Octants 2 and 8 are used to inject beam into the LHC from SPS. The 2 beams  
**1000** are crossed in octants 1,2,5 and 8. The main experiments are built around these  
**1001** crossing points. Octants 3 and 7 are used for beam cleansing. This is achieved  
**1002** through collimators that scatter particles with too high momentum or position  
**1003** offsets off from the beam. The RF cavities used for acceleration are located in  
**1004** octant 4 and octant 6 is used for dumping the beam. The beam dump is made  
**1005** up of two iron septum magnets, one for each beam, that will kick the beam away  
**1006** from machine components into an absorber when needed.

1007 **3.2.1 LHC experiments**

1008 As of 2018 there are four main experiments at the LHC; ALICE, ATLAS, CMS  
1009 and LHCb and three smaller ones LHCf, TOTEM and MoEDAL. ALICE will be  
1010 covered in section 3.3.

1011 ATLAS (A Toroidal LHC ApparatuS) and CMS (Compact Muon Solenoid) are  
1012 the two largest experiments at the LHC. They are both multipurpose experiments  
1013 designed to be sensitive to many different possible new physics signals. The biggest  
1014 discovery made by these so far is the discovery of the Standard Model Higgs boson,  
1015 which was simultaneously published by the experiments in 2012 [?, ?].

1016 The LHCb (LHC beauty) experiment [?] is made for studying the bottom  
1017 (beauty) quark. Main physics goals include measurement of the parameters of CP  
1018 violation with decays of hadron containing the bottom quark. One of the most  
1019 important results published by LHCb is the first measurement of  $B_s^0 \rightarrow \mu^+ \mu^-$   
1020 decay, which was found to be in line with the Standard Model.

1021 In addition to the four large experiments there are three smaller experiments  
1022 along the LHC ring. LHCf (LHC forward) is located at interaction point 1 with  
1023 ATLAS. It aims to simulate cosmic rays by the particles thrown forwards by the  
1024 collisions in ATLAS.

1025 TOTEM (TOTal Elastic and diffractive cross section Measurement) is located  
1026 near the CMS experiment at point 5. This allows it to measure particles emerging  
1027 from CMS with small angles. The main goals is to measure the total, elastic and  
1028 inelastic cross-sections in pp collisions [?].

1029 The MoEDAL (Monopole and Exotics Detector At the LHC) experiment is  
1030 located at the interaction point 8 together with the LHCb experiment. MoEDAL  
1031 tries to measure signatures of hypothetical particles with magnetic charge, mag-  
1032 netic monopoles.

1033 **3.3 ALICE**

1034 ALICE (A Large Ion Collider Experiment) [?] is the dedicated heavy ion exper-  
1035 iment at the LHC. ALICE was designed to cope with the expected very high  
1036 multiplicity environment of heavy ion collisions. The design allows measurement  
1037 of a large number of low momentum tracks. The different detector subsystems are  
1038 optimised to provide high momentum resolution and excellent particle identifica-  
1039 tion capabilities over a broad range of momentum.

1040 A schematic view of the ALICE detector in 2018 is presented in Figure 23.  
1041 This section will go through the composition of ALICE as it has been during  
1042 run 2 between 2014 and 2018. The detector will go through significant upgrades  
1043 during Long Shutdown 2 in 2019-2020. As in all the major high energy physics  
1044 experiments the positioning of the detectors follows a layered structure. Closest to

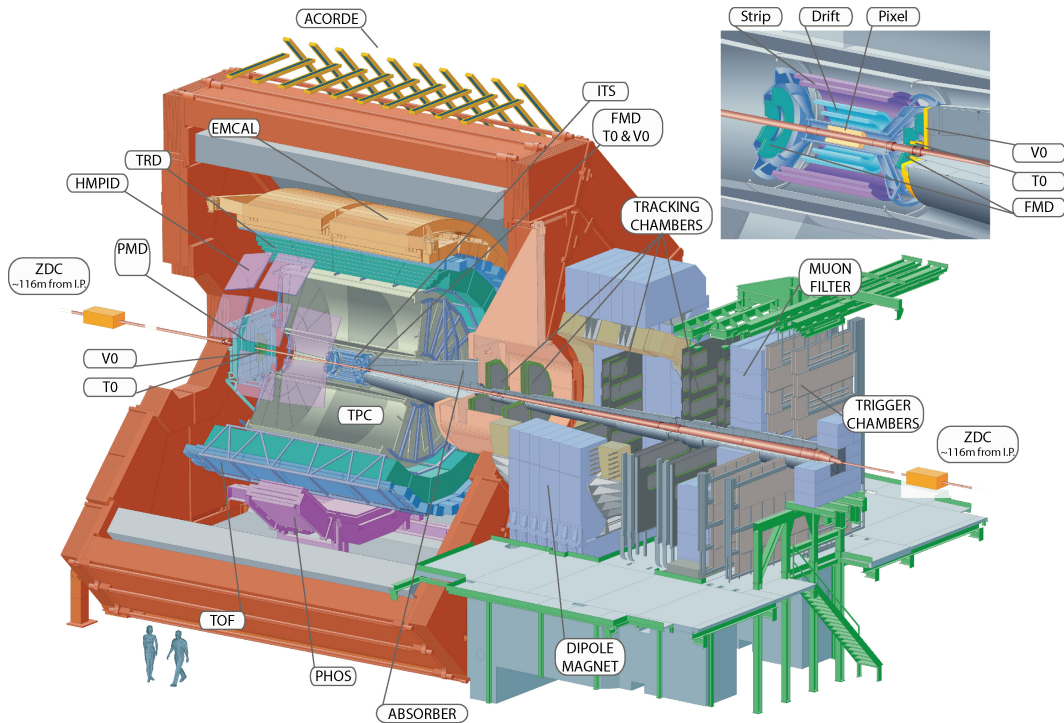


Figure 23: Schematic view of ALICE

the interaction point are the tracking detectors. The main task of these detectors is to locate the position of the primary interaction vertex accurately and to record the tracks of charged particles. To achieve this they need a very good spatial resolution close to the interaction point. Tracking detectors do not significantly alter the tracks of traversing particles. Thus they can be located in the innermost layers.

Calorimeters are designed to stop any particles hitting them and use the absorption to measure the energy of the particles. Thus they must be located behind the tracking detectors. ALICE has two separate calorimeter systems, the electromagnetic calorimeters measure mainly electrons and photons, while the muon detection system measures muons.

### 3.3.1 Tracking

The main design guideline for the tracking detectors in ALICE was the requirement to have good track separation and high granularity in the high multiplicity environment of heavy ion collisions. Before LHC was built the wildest estimates put the particle density at 8000 charged particles per unit of rapidity [1]. In reality the particle density turned out to be significantly smaller, about 1600 charged

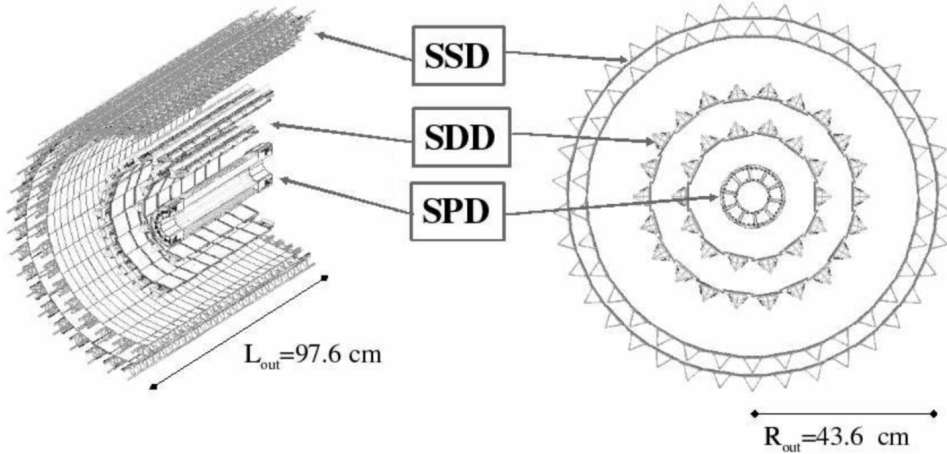


Figure 24: Schematic view of ALICE Inner Tracking System

1062 particles per rapidity unit. []

1063 The main tracking detector in ALICE is the Time Projection Chamber (TPC),  
1064 discussed in more detail in section 3.3.2

1065 Between TPC and the beam pipe there is an array of six layers of silicon detec-  
1066 tors, called the inner tracking system (ITS) [?]. The main tasks of the ITS are to  
1067 locate the primary vertex with a resolution better than  $100 \mu m$ , to reconstruct the  
1068 secondary vertices from decaying particles, to track and identify particles with mo-  
1069 menta below 200 MeV and to compliment the momentum and angle measurements  
1070 of TPC. During long shutdown 2 in 2019-2020 the entire ITS will be replaced [?].  
1071 As of 2018 the two innermost layers are made of the silicon pixel detector (SPD).  
1072 As it's the closest detector to the interaction point it requires are very high spatial  
1073 resolution. Thus the choice of pixel technology is natural. In heavy ion collisions  
1074 the particle density is around 50 particles per  $cm^2$ .

1075 The next two layers are the silicon drift detector (SDD), which is made out of  
1076 homogeneous neutron transmutation doped silicon. It is ionized when a charged  
1077 particle goes through the material. The generated charge then drifts to the col-  
1078 lection anodes, where it is measured. The maximum drift time in SDD is about 5  
1079  $\mu s$ . This design gives very good multitrack capabilities and provides two out of the  
1080 four  $dE/dx$  samples in the ITS.

1081 The two remaining layers in the ITS are the silicon strip detector (SSD). The  
1082 strips work in a similar way as silicon pixels, but by itself one layer only provides  
1083 good resolution in one direction. Combining two crossing grids of strips provides 2  
1084 dimensional detection. Each charged particle will hit two intervening strips. The  
1085 position of the hit can be deduced from the place where the strips cross each other.

1086 **3.3.2 TPC**

1087 Time projection chamber (TPC) is a cylindrical detector filled with  $88m^3$  of  
1088 Ne – CO<sub>2</sub> (90/10 %) gas mixture. The gas is contained in a field cage that provides  
1089 an uniform electric field of  $400V/cm$  along the z-axis (along the beam direction).  
1090 Charged particles traversing through the TPC volume will ionise the gas along  
1091 their path. This liberates electors that drift towards the end plates of the cylin-  
1092 der.

1093 The field cage is separated into two detection volumes by the central high  
1094 voltage electrode. Both sides have a drift length of 2.5 m and inner/outer diameters  
1095 of 1.2/5 m. This means the central electrode must provide a maximum potential  
1096 of 100 kV to achieve the design field magnitude. The maximum time required for  
1097 electrons to drift through the chamber is about  $90 \mu s$ .

1098 When electrons reach the end of the main cylinder they enter the readout  
1099 chambers. The readout section of both sides consists of 18 outer chambers and  
1100 18 inner chambers. Each of them are made of multiwire proportional chambers  
1101 with cathode pad readout. This design is used in many TPCs before. During  
1102 Long Shutdown 2 in 2019-2020, the multiwire chambers will be replaced by Gas  
1103 Electron Multipliers (GEMs, see section 3.3.3).

1104 The relatively slow drift time of  $90 \mu s$  is the limiting factor for the luminosity  
1105 ALICE can take. The occupancy of the TPC must be kept in a manageable level.

1106 **3.3.3 TPC upgrade**

1107 During long shutdown 2 in 2019-2020 ALICE will go through significant modifica-  
1108 tions. The goal is to be able have continuous readout [?] in heavy ion collisions at  
1109 an interaction rate of 50 kHz. I have made a personal contribution to the quality  
1110 assurance of the new GEM readout of TPC.

1111 ALICE will add a new Forward Interaction trigger (FIT) to replace the V0 and  
1112 T0 detectors.

1113 Additionally the current inner tracking system (ITS) will be completely re-  
1114 placed. The current layered structure with three different technologies will be  
1115 replaced by an all pixel detector with significantly reduced pixel size. Additionally  
1116 the first layer will be brought closer to the beam pipe. The new ITS will have  
1117 better tracking efficiency and better impact parameter resolution.

1118 The muon detection will be complimented by the Muon Forward Tracker (MFT) [?].  
1119 Based on the same technology as the new ITS, MFT will be placed before the  
1120 hadron absorber that sits in front of the existing muon spectrometer. MFT should  
1121 significantly increase the signal/background ratio in heavy quark measurements.

1122 Many subdetectors will make small improvements to enhance the readout rate.  
1123 The central trigger processor will be replaced and ALICE will introduce a new

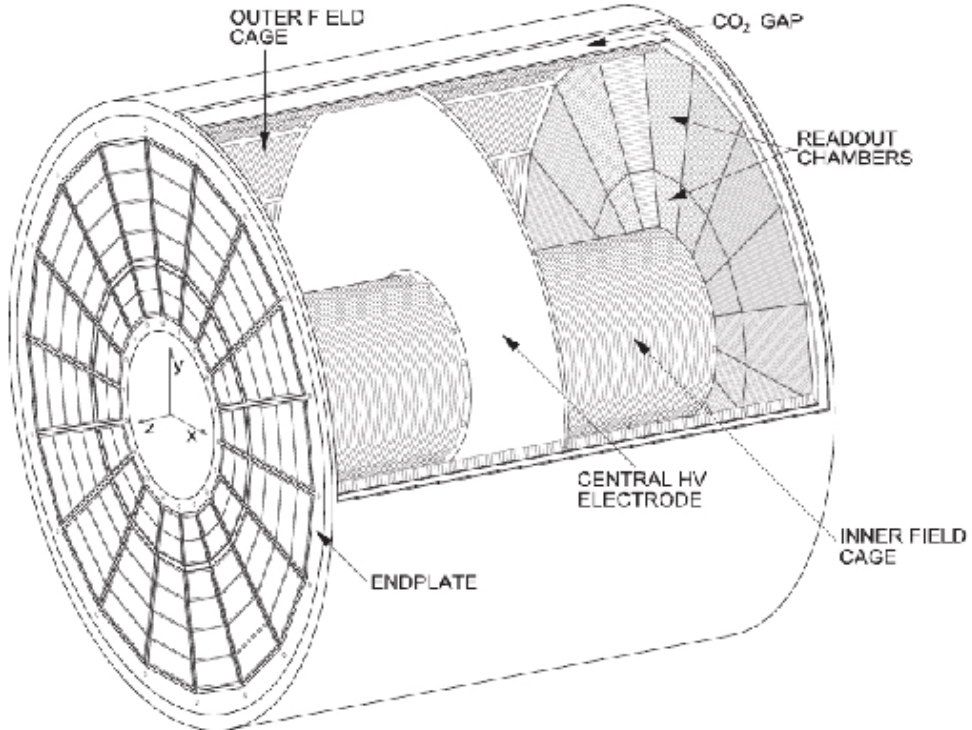


Figure 25: Schematic view of ALICE Time Projection Chamber

1124 framework  $O^2$  that combines both online data acquisition and offline analysis.

1125 The detector restricting the readout the most at the moment is the TPC. The  
1126 current wire chamber based system limits the readout rate to 3.5 kHz. To achieve  
1127 the 50 kHz readout rate goal the wire chambers will be replaced by a Gas Electron  
1128 Multiplier (GEM) based system.

1129 TPC has a total of 36 inner and 36 outer readout chambers. Each of these will  
1130 consist of 4 layers of GEM foils. The inner chambers will only have one foil for  
1131 each layer. The outer chambers are separated into three sections, each with its  
1132 own layer of foils. Each gem foil is made up of a  $50\ \mu\text{m}$  thick resistive capton layer,  
1133 coated on both sides by  $5\ \mu\text{m}$  thick layers of copper. Each foils is separated into a  
1134 number (20-24) of distinct active areas. The active areas are pierced quite densely,  
1135 they have 50-100 holes in the area of a single  $\text{mm}^2$ . The density of holes changes  
1136 from layer to layer. The two middle layers of foils have a larger (double) pitch  
1137 (smaller hole density) while the top and bottom layers have a smaller (normal)  
1138 pitch (larger hole density).

1139 The holes have a conical shape which they acquire during a two step chemical  
1140 etching process.

1141 The working principle of these foils is based on electrodynamics. **elaborate** There  
1142 is a large potential difference (140-400 V) applied to the two sides of the foil, which  
1143 results in large field in each hole. This acts both as a lens and an amplifier for  
1144 the electrons. The amplification happens inside the holes where the field is the  
1145 strongest.

1146 The GEMs are designed to minimize ion backflow to allow continuous, ungated  
1147 and untriggered readout.

### 1148 3.3.4 Particle identification

1149 One guiding principle in the design of ALICE was to achieve good particle iden-  
1150 tification (PID) over a large part of phases space and for several different particle  
1151 types. In ALICE there are several detectors taking part in the identification of  
1152 particles.

1153 One of the particle identification detectors is the transition radiation detector  
1154 (TRD) [?]. Its main task is identifying electors with momenta larger than 1 GeV.  
1155 Transition radiation is produced when highly relativistic particles traverse the  
1156 boundary between to media having different dielectric constants. The average  
1157 energy of the emitted photon is approximately proportional to the Lorentz factor  $\gamma$   
1158 of the particle, which provides an excellent way of discriminating between electrons  
1159 and pion. ALICE TRD is made of a composite layer of foam and fibres. The  
1160 emitted photons are then measured in six layers of Xe/CO<sub>2</sub> filled time expansion  
1161 wire chambers.

1162 The time of flight (TOF) detector uses a very simple physics principle, i.e.  
1163 calculating the velocity of the particle using the time of flight between two points.  
1164 Combining this with the momentum of particle, obtained from the tracking de-  
1165 tectors, one can calculate the mass of the particle, which identifies particles. The  
1166 TOF detector consists of multigap resistive wire chambers. These are stacks of  
1167 resistive plates spaced equally. They allow time of flight measurements in large  
1168 acceptance with high efficiency and with a resolution better than 100 ps.

1169 The third specific particle identification detector is the high momentum particle  
1170 identification (HMPID) detector. The HMPID uses a ring imaging Cherenkov  
1171 counter to identify particles with momenta larger than 1 GeV. Particles moving  
1172 through a material faster than the speed of light in the material will produce  
1173 Cherenkov radiation. The velocity of the particle determines the angle at which  
1174 the radiation is emitted. Measuring this angle gives the velocity of the particle.  
1175 This can be again used to calculate the mass of the particle, if the momentum is  
1176 known. In HMPID the material is a liquid radiator and the photons are measured  
1177 with multiwire proportional chambers in conjunction with photocathodes.

1178 In addition to the specific particle identification detectors, the general purpose  
1179 tracking detectors can be used for identification through the use of specific energy

loss of charged particles traversing through a medium and the transition radiation emitted by charged particles when crossing the boundary between two materials.

$dE/dx$  measurements are provided by the last four layers of the ITS detector, i.e. the SDD and the SSD, thanks to their analog readout. [?] ITS provides particle identification in the low  $p_T$  region, up to 1GeV, and pions reconstructed in the standalone mode can be identified down to 100 MeV. Similar to ITS the TPC detector provides specific energy loss measurements. TPC can identify charged hadrons up to  $p_T$  1 – 2GeV as well as light nuclei, He3 and He4.

### 3.3.5 Electromagnetic Calorimeter

Calorimeters are designed to measure the energy of particles. Electromagnetic calorimeters specialise in detecting particles that interact primarily through the electromagnetic interaction, namely photons and electrons. They are required in many neutral meson and direct photon analyses. In addition the energy information enhance jet measurements.

ALICE has two electromagnetic calorimeters, the photon spectrometer (PHOS) [?] and the electromagnetic calorimeter (EMCal) [?]. PHOS is a homogeneous calorimeter that consists of scintillating PbWO<sub>4</sub> crystals, which generate a bremsstrahlung shower and produce scintillation light. The energy of the particle determines the amount of light produced. To improve the charged particle rejection, PHOS includes a charged particle veto detector (CPV) [?]. PHOS is built to have a very fine granularity, making it well suited for measuring direct photons and neutral mesons.

EMCal is a sampling calorimeter. It consists of layers of lead and scintillator tiles. The lead tiles produce the shower and scintillator tiles the light. The signal is then read with wavelength shifting fibres. The acceptance of EMCal in the azimuthal angle is 80 deg <  $\phi$  < 187 deg. During long shutdown 1 in 2013-2015, EMCal was extended with the di-jet calorimeter (DCal) [?], giving an additional acceptance region of 260 deg <  $\phi$  < 320 deg. This provides partial back-to-back coverage. In comparison to PHOS, EMCal has coarser granularity, but a significantly larger acceptance, making it suitable for jet physics.

### 3.3.6 Forward detectors

ALICE includes a few small and specialised detectors of importance. The event time is determined with very good precision (< 25 ns) by the T0 detector [?]. T0 consists of two sets of Cherenkov counters that are mounted around the beam pipe on both sides of the interaction point. T0 gives the luminosity measurement in ALICE.

Another small detector in the forward direction is the V0 detector [?]. This

1217 consists of two arrays of segmented scintillator counters located at  $-3.7 < \eta <$   
1218  $-1.7$  and  $2.8 < \eta < 5.1$ . V0 is used as a minimum bias trigger and for rejection  
1219 of beam-gas background. Particle multiplicity in the forward direction can be  
1220 related to the event centrality. Thus V0 is the main detector used in centrality  
1221 determination in PbPb collisions.

1222 The multiplicity measurement of V0 is complimented by the forward multi-  
1223 plicity detector (FMD) [?]. FMD includes five rings of silicon strip detectors that  
1224 make up the FMD. FMD gives acceptance in the range  $-3.4 < \eta < -1.7$  and  
1225  $1.7 < \eta < 5.0$ .

1226 During long shutdown 2 in 2019-2020, V0 and T0 will be replaced by the Fast  
1227 Interaction Trigger (FIT) detector [?]. For historical reasons elements of FIT are  
1228 also referred to as V0+ and T0+. FIT will allow centrality, event plane, luminosity  
1229 and interaction time determination in the continuous readout mode, that ALICE  
1230 will operate in after 2020.

1231 For photon multiplicity measurement ALICE has the photon multiplicity de-  
1232 tector (PMD) [?]. PMD uses two planes of gas proportional counters with a  
1233 cellular honeycomb structure. PMD gives the multiplicity and spatial distribution  
1234 of photons in the region  $2.3 < \eta < 3.7$ .

1235 On top of the ALICE magnet there is an array of 60 large scintillators called  
1236 the ALICE cosmic ray detector (ACORDE) [?]. ACORDE is used as a trigger  
1237 for cosmic rays for calibration and alignment.

1238 The only hadronic calorimeters in ALICE are the zero degree calorimeters  
1239 (ZDC) [?], which are located next to the beam pipe in the machine tunnel about  
1240 116 m from the interaction point. There are two sets of calorimeters. One is  
1241 made of tungsten, specialising in measuring neutrons, while the other, made of  
1242 brass, is specialised in measuring protons. In heavy ion and especially in proton-  
1243 lead collisions, ZDC gives information about the centrality of the event. ZDC is  
1244 meant to detect spectators, i.e. parts of the colliding ions that do not take part  
1245 in the interaction. If there are more spectators, the collisions is likely to be more  
1246 peripheral.

1247 A new detector installed during the long shutdown 1 is the ALICE diffractive  
1248 detector (AD) [?]. AD consists of two assemblies, one in each side of the interaction  
1249 point, both made of two layers of scintillators. These assemblies are situated about  
1250 17 m and 19.5 m away from the interaction points. The pseudorapidity coverage is  
1251  $-6.96 < \eta < -4.92$  and  $4.78 < \eta < 6.31$ . AD greatly enhances ALICE's capability  
1252 for diffractive physics measurements that require a large pseudorapidity gap.

### 1253 3.3.7 Muon spectrometer

1254 Outside the main magnet, ALICE has a spectrometer dedicated to measuring  
1255 muons [?]. In heavy ion physics muons are mainly used to measure the production

1256 of the heavy quark resonances  $J/\psi$ ,  $\Psi'$ ,  $\Upsilon$ ,  $\Upsilon'$  and  $\Upsilon''$ .

1257      The muon spectrometer consists of three parts, the absorber, the muon tracker  
1258 and the muon trigger. The absorber is meant to remove the hadronic background  
1259 as efficiently as possible. After the absorber there are ten plates of thin cathode  
1260 strip tracking stations with high granularity, the muon tracker. After the muon  
1261 tracker there is a layer of iron to filter out any remaining particles, other than  
1262 muons. The muon trigger is located behind this layer. The trigger consists of four  
1263 resistive plate chambers.

1264 **3.3.8 Trigger**

<sub>1265</sub> **4 Event and track selection**

<sub>1266</sub> **5 Analysis method**

<sub>1267</sub> **5.1 Jet Finding**

<sub>1268</sub> The analysis is performed by analysing jet constituents. In each collision event, the  
<sub>1269</sub> jets are reconstructed using FastJet [103] with the anti- $k_T$  algorithm [104]. Jets for  
<sub>1270</sub>  $R=0.4$  are selected in  $|\eta| < 0.25$  to satisfy the fiducial acceptance of the EMCAL. In  
<sub>1271</sub> jet reconstruction both charged tracks with  $p_T > 0.15 \text{ GeV}/c$  and neutral cluster  
<sub>1272</sub> with  $p_T > 0.30 \text{ GeV}/c$  are considered. In the analysis, results are presented in  
<sub>1273</sub> terms of the jet transverse momentum  $p_{T,\text{jet}}$ .

<sub>1274</sub> **5.1.1 Anti  $k_T$  algorithm**

<sub>1275</sub> Jets are reconstructed using the anti- $k_T$  algorithm [104]. The algorithm works by  
<sub>1276</sub> trying to undo the splittings through combining pseudojets/tracks.

$$k_{T,i}^2 = p_{T,i}^{2p}$$

<sub>1277</sub> For each pair of protojets the distance measure is calculated as

$$k_{T,(i,j)}^2 = \min(p_{T,i}^{2p}, p_{T,j}^{2p}) \frac{\Delta R_{i,j}^2}{D^2},$$

<sub>1278</sub> where

$$R_{i,j} = (\phi_i - \phi_j)^2 + (y_i - y_j)^2$$

<sub>1279</sub> If  $k_{T,i}$  is the smallest quantity then the protojet is a jet and it is removed  
<sub>1280</sub> from further consideration. If  $k_{T,(i,j)}$  is the smallest quantity the two protojets are  
<sub>1281</sub> merged. Iterate until no protojets are left.

<sub>1282</sub> The choice of the power  $p$  in the distance measure depends on the algorithm  
<sub>1283</sub> used

- <sub>1284</sub> •  $p = 1$ :  $k_T$  algorithm
- <sub>1285</sub> •  $p = 0$ : Cambridge Aachen algorithm
- <sub>1286</sub> •  $p = -1$ : anti- $k_T$  algorithm

<sub>1287</sub> With the choice  $p = -1$  in anti- $k_T$  algorithm, the softest splittings are undone  
<sub>1288</sub> first.

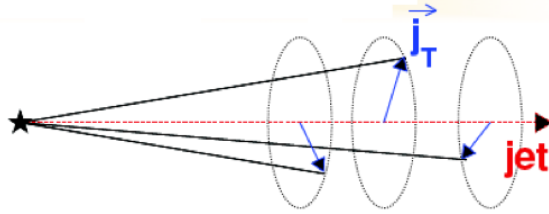


Figure 26: Illustration of  $\vec{j}_T$ . The jet fragmentation transverse momentum,  $\vec{j}_T$ , is defined as the transverse momentum component of the track momentum,  $\vec{p}_{\text{track}}$ , with respect to the jet momentum,  $\vec{p}_{\text{jet}}$ .

## 1289 5.2 $j_T$

1290 The jet fragmentation transverse momentum,  $j_T$ , is defined as the component of  
1291 the constituent particle momentum,  $\vec{p}_a$ , transverse to the jet momentum,  $\vec{p}_{\text{jet}}$ . The  
1292 resulting  $\vec{j}_T$  is illustrated in Fig. 26. The length of the  $\vec{j}_T$  vector is

$$j_T = \frac{|\vec{p}_{\text{jet}} \times \vec{p}_{\text{track}}|}{|\vec{p}_{\text{jet}}|}. \quad (28)$$

1293 It is commonly interpreted as a transverse kick with respect to the initial hard  
1294 parton momentum that is given to a fragmenting particle during the fragmentation  
1295 process, which is a measure of the momentum spread of the jet fragments [].

1296 The reconstructed jet axis is used for  $j_T$  reference. Any charged track within  
1297 a fixed cone with radius  $R$  is taken as a jet constituent, as opposed to using the  
1298 constituent list provided by the jet algorithm. Anti- $k_T$  produces jets that are  
1299 very circular in shape. Thus this doesn't change the constituent list considerably.  
1300 Neutral tracks are used only in jet reconstruction.

### 1301 5.2.1 1 over $j_T$

$j_T$  results are shown as

$$\frac{1}{j_T} \frac{dN}{dj_T}$$

1302 distributions. The logic behind this is that  $j_T$  is inherently a two-dimensional  
1303 observable, comprised of  $j_{Tx}$  and  $j_{Ty}$  components. So the actual physical observable  
1304 would be

$$\frac{d^2N}{dj_{Tx} dj_{Ty}}$$

1305 Changing into polar coordinates with  $j_{\text{Tr}} = j_{\text{T}}$  and  $\theta$  gives

$$\frac{d^2N}{j_{\text{T}} dj_{\text{T}} d\theta},$$

1306 where  $j_{\text{T}}$  over the azimuth  $\theta$  should stay constant and it can be integrated over  
1307 giving

$$\frac{1}{2\pi} \frac{dN}{j_{\text{T}} dj_{\text{T}}}.$$

### 1308 5.3 Unfolding

#### 1309 Extend unfolding

1310 The resulting  $j_{\text{T}}$  distributions are corrected for the detector inefficiency using  
1311 the unfolding method. The response matrix for the unfolding is obtained from a  
1312 PYTHIA [105] simulation.

Measured distributions are affected by two main factors; Limited acceptance -  
The probability to observe a given event is less than one and limited resolution -  
Quantity  $x$  cannot be determined exactly, but there is a measurement error. True  
 $f(x)$  and measured  $g(y)$  distributions are connected by a convolution integral.  
Including statistical fluctuations this becomes

$$\hat{g}(y) = \int_a^b A(y, x) f(x) dx + \epsilon(y),$$

where  $A$  is the detector response obtained by Monte Carlo simulations and  $\epsilon(y)$   
is the term coming from statistical fluctuations. If  $x$  and  $y$  are discrete variables  
we have

$$\hat{g}_i = \sum_{j=1}^m A_{ij} f_j + \epsilon_i,$$

Or in matrix form

$$\hat{g} = Af + \epsilon$$

If the only detector effect is limited acceptance,  $A$  is a diagonal matrix. In a  
general discrete case the (naive) solution is obtained by the inverse matrix

$$\hat{f} = A^{-1} \hat{g}$$

1313 However this usually leads to oscillating solutions and determining the inverse  
1314 matrix can be difficult.

1315 Two common methods to perform this inversion are Bayesian and SVD unfold-  
1316 ing methods. Often the solution requires some additional *a priori*. For example  
1317 the solution should be smooth in most cases.

<sub>1318</sub> **5.3.1 Bayesian unfolding**

The bayesian (iterative) method is based on the Bayes formula [].

$$P(C_i|E_j) = \frac{P(E_j|C_i) P_0(C_i)}{\sum_{l=1}^{n_C} P(E_j|C_l) P_0(C_l)},$$

<sub>1319</sub> i.e. Probability of Cause ("truth")  $C_i$  given Effect ("observed")  $E_j$  is proportional to the probability of observing  $E_j$  given  $C_i$  (response matrix) and the truth distribution  $P_0(C_i)$ .

At first  $P_0$  is given some starting distribution, either a uniform distribution or some guess of the final distribution. Taking into account the inefficiency this gives

$$\hat{n}(C_i) = \frac{1}{\epsilon_i} \sum_{j=1}^{n_E} n(E_j) P(C_i|E_j),$$

where

$$P(C_i|E_j) = \frac{P(E_j|C_i) P_0(C_i)}{\sum_{l=1}^{n_C} P(E_j|C_l) P_0(C_l)},$$

and

$$\hat{n}(C_i) = \frac{1}{\epsilon_i} \sum_{j=1}^{n_E} n(E_j) P(C_i|E_j).$$

First  $P(C_i|E_j)$  is calculated with the uniform distribution or best guess of the shape of the distribution. This is then used to calculate the new distribution  $\hat{P}(C_i)$

$$\hat{N}_{true} = \sum_{i=1}^{n_C} \hat{n}(C_i), \hat{P}(C_i) = P(C_i|n(E)) = \frac{\hat{n}(C_i)}{\hat{N}_{true}}$$

<sub>1322</sub>  $P_0$  is then replaced with  $\hat{P}$  and the procedure is repeated until an acceptable <sub>1323</sub> solution is found.

<sub>1324</sub> **5.3.2 Toy Monte Carlo**

**remove?** A toy Monte Carlo simulation was performed to see the performance in an ideal case. Sample jet  $p_T$  values from observed  $p_T$  distribution. Starting from this  $p_T$  start creating tracks with

$$p_{track} = z_{track} p_{T,jet}$$

<sub>1325</sub> where  $z_{track}$  is sampled from the observed  $z$  distribution. All tracks below 0.15GeV <sub>1326</sub> are discarded. Sampling is continued until the sum of the track transverse momenta

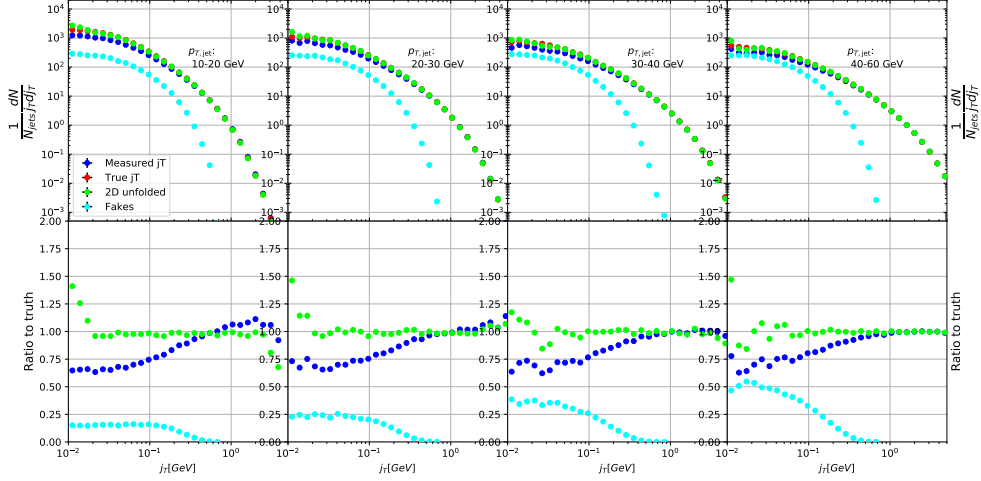


Figure 27: Results from unfolding in Toy Monte Carlo

1327 exceeds the jet transverse momentum. Jet is then defined as the sum of the track  
 1328 momenta.

1329 Simultaneously a  $p_T$  dependant observation efficiency is applied to the tracks  
 1330 and a separate observed jet is calculated using only the observed tracks. Addi-  
 1331 tionally a set of fake tracks is added to the observed jet. Tracks are always either  
 1332 observed or not at the true momentum. No smearing is added to the observed  
 1333 momentum.

Afterwards the tracks are looped over for  $j_T$  calculation. For observed tracks we calculate  $j_T$  with respect to both the true jet axis and the observed jet. 2D Response matrix is filled with

$$(j_{T,\text{obs}}, p_{T,\text{jet},\text{obs}}, j_{T,\text{true}}, p_{T,\text{jet},\text{true}})$$

1334 In practice this is done with a set of 3D histograms, where  $p_{T,\text{jet},\text{true}}$  determines  
 1335 the histogram index and the remaining three values the bin in the 3D histogram.

1336 After creating the response matrices, an identical procedure is carried out the  
 1337 create testing data. Now instead of filling response matrices, 2D histograms are  
 1338 filled with  $(j_{T,\text{obs}}, p_{T,\text{jet},\text{obs}})$  and  $(j_{T,\text{true}}, p_{T,\text{jet},\text{true}})$

1339 The observed distributions are unfolded using RooUnfold's 2D Bayesian (iter-  
 1340 ative) algorithm. Results are shown in figure 27.

### 1341 5.3.3 Pythia Response matrices

1342 Response matrices are filled through correlation between MC detector and particle  
 1343 level jets and tracks.

Table 2:  $j_T$  and  $p_T$  ranges used in unfolding. The same ranges are used for detector and truth level.

	$j_T$	$p_{T\text{jet}}$
Min	0.01	5
Max	20	500

1344 The ranges of both  $j_T$  and  $p_{T\text{jet}}$  extend the ranges in end results. These are  
 1345 shown in Tab. 2. The ranges are the same in detector and particle level.

1346 When calculating  $j_T$  for MC particles the code checks whether a corresponding  
 1347 detector level track exists and if that track had a  $j_T$  value. Additionally check  
 1348 for detector level tracks that don't have corresponding particle level track or that  
 1349 track does not have  $j_T$  value.

1350 Possible cases:

- 1351 • We find a corresponding track with a  $j_T$  value, response matrix is filled  
 1352 normally with  $(j_T^{obs}, p_T^{obs}, j_T^{true}, p_T^{true})$
- 1353 • We don't find a corresponding track. Record  $(j_T^{true}, p_T^{true})$  as a miss
- 1354 • We find a corresponding track, but it didn't have  $j_T$  value. Most likely  
 1355 because it was not part of a jet. Similary record  $(j_T^{true}, p_T^{true})$  as a miss
- 1356 • For detector level tracks with no correspondence in particle level set record  
 1357 cord  $(j_T^{obs}, p_T^{obs})$  as a fake

### 1358 5.3.4 2D response matrices

1359 In the analysis code the response matrix is made of an array of 3 dimensional  
 1360 histograms, with  $(j_{T,obs}, p_{T,obs}, j_{T,true})$  as axes. The histogram index gives the  $p_{T,true}$   
 1361 value.

### 1362 5.3.5 Unfolding algorithm

1363 As a primary method unfolding is performed with an iterative (bayesian) algorithm  
 1364 using the RooUnfold [106] package. The number of iterations used is 4.

### 1365 5.3.6 Effect of number of iterations

1366 The iterative unfolding algorithm permits the change of number of iterations.  
 1367 The unfolding was carried out using different numbers of iterations. The results  
 1368 from these different cases are shown in Fig. 28. The results are compared to the  
 1369 default unfolding algorithm with 4 iterations. The difference in results between  
 1370 the different cases is mostly less than 2.5%.

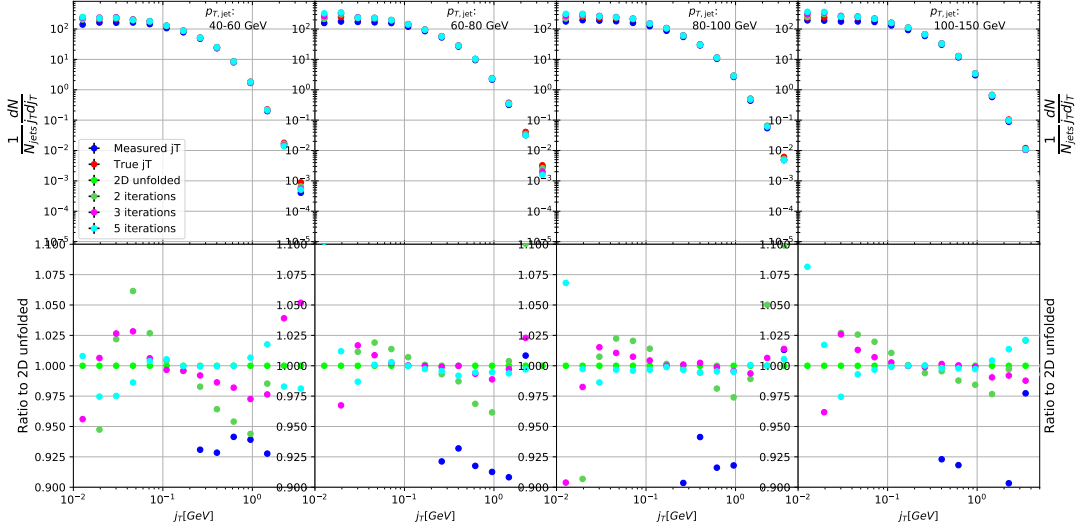


Figure 28: Unfolding with different number of iterations

### 1371 5.3.7 Effect of different prior

1372 The iterative algorithm requires a prior estimate of the shape of the distribution.  
 1373 As a default prior the truth (particle level) distribution is used. To test the effect  
 1374 of changing the prior we instead use the unfolded  $j_T$  distribution as prior. The  
 1375 results are compared to the unfolding algorithm with the default prior. This is  
 1376 shown in Fig. 29 The difference in results between the different cases is mostly less  
 1377 than 2.5%.

### 1378 5.3.8 Effect of $p_T$ truncation

### 1379 5.3.9 Unfolding closure test

1380 Pythia set is divided in 2 halves. First is used to fill the response matrices, as well  
 1381 as record missed and fake tracks. Second half is used to test the effectiveness of  
 1382 the unfolding method. Jet  $p_T$  distributions are shown in figure 31a and response  
 1383 matrix are shown in figure 31b.

1384 Response matrices within single jet  $p_T$  bins are shown in figure 32. Results  
 1385 from the closure test are shown in figure 33. In the lowest jet  $p_T$  bins unfolding  
 1386 fails to recover the true distribution. The lowest jet  $p_T$  bins are dominated by  
 1387 combinatorial jets and thus the true detector response is likely not retrieved.

1388 Above jet  $p_T$  30-40 GeV the distribution is recovered well in the mid  $j_T$  region.  
 1389 At  $j_T < 0.1$  there is clear discrepancy. The final results are shown only for  $j_T > 0.1$ .  
 1390 Additionally there is some discrepancy at very high  $j_T$ . This is taken into account

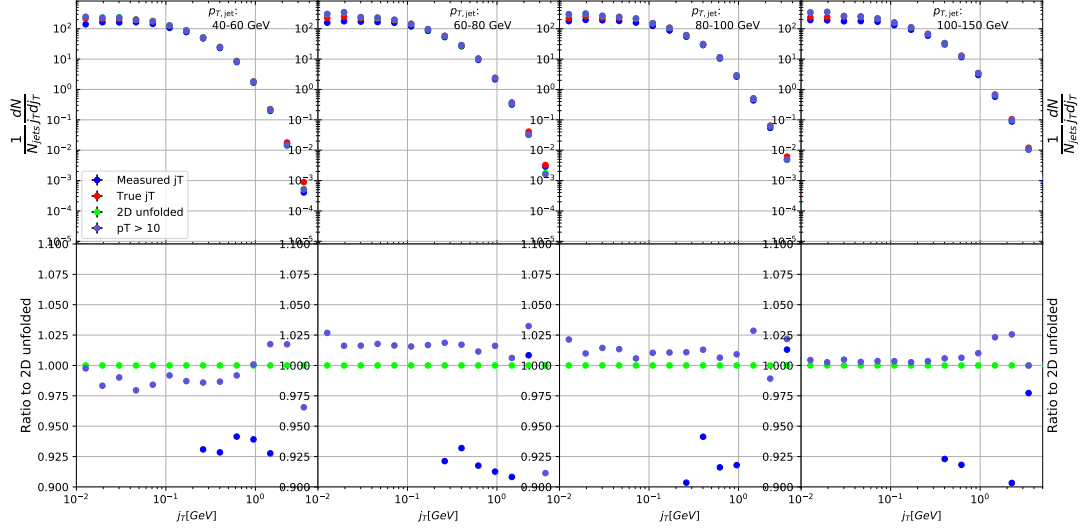


Figure 29: Effect of changing minimum jet  $p_T$  used in unfolding from 5 to 10 GeV

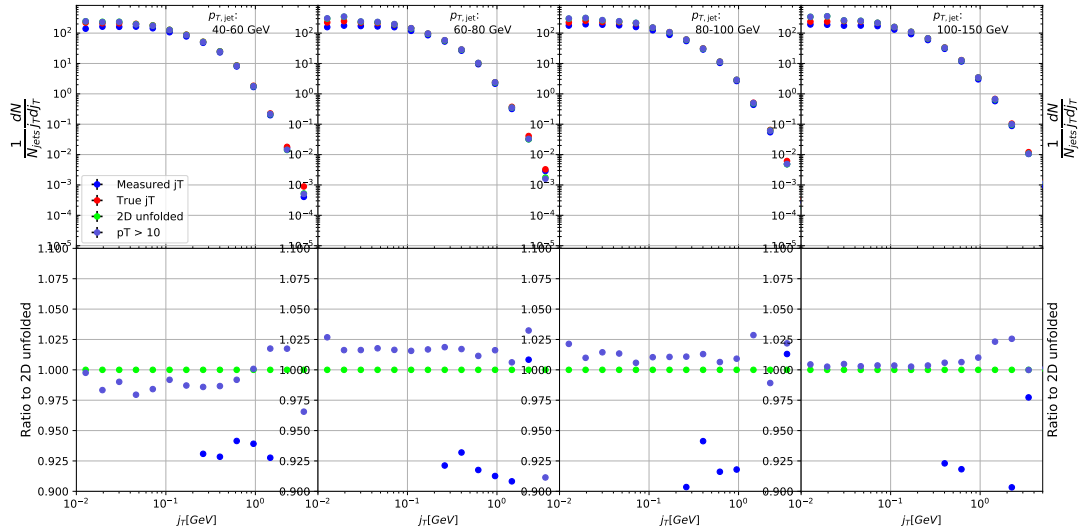
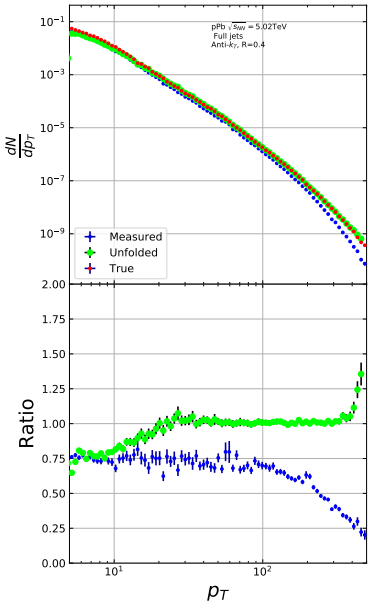
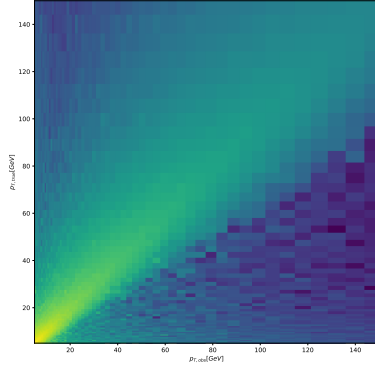


Figure 30: Effect of changing minimum jet  $p_T$  used in unfolding from 5 to 10 GeV



(a) Unfolded jet  $p_T$  distribution in Pythia  
closure test



(b) Jet  $p_T$  response matrix from unfolding  
closure test

1391 in the unfolding systematics. (TODO: Show this)

## 1392 5.4 Background

1393 When calculating  $j_T$  distribution for jet constituents there is a contribution from  
1394 underlying event (UE), i.e. tracks that just happen to be close to the jet axis.  
1395 To find the signal coming from the actual jet we need to subtract the background  
1396 (UE) contribution. On a jet-by-jet basis this is impossible, so we try to estimate  
1397 the background by looking at regions of the detector where there are no tracks  
1398 from jets, but only uncorrelated tracks from the underlying event.

1399 The underlying event is estimated by looking at an imaginary jet cone perpen-  
1400 dicular to the observed jet axis ( $\frac{\pi}{2}$  Rotation in  $\phi$ ).  $j_T$  is calculated for any tracks  
1401 found within this cone. The vector sum of the individual track momentum and  
1402 the imaginary jet axis is used as reference for  $j_T$ . The background obtained in  
1403 this manner is subtracted from the unfolded inclusive  $j_T$  distribution, which gives  
1404 the resulting signal distribution. To make sure there is no jet contribution in the  
1405 background, any events with jets inside the perpendicular cone are not used for  
1406 background estimation.

1407 We have two methods for background estimation. In the first we look at the  
1408 direction perpendicular to the jet. This is assumed to be the region least likely to  
1409 contain jet contributions.

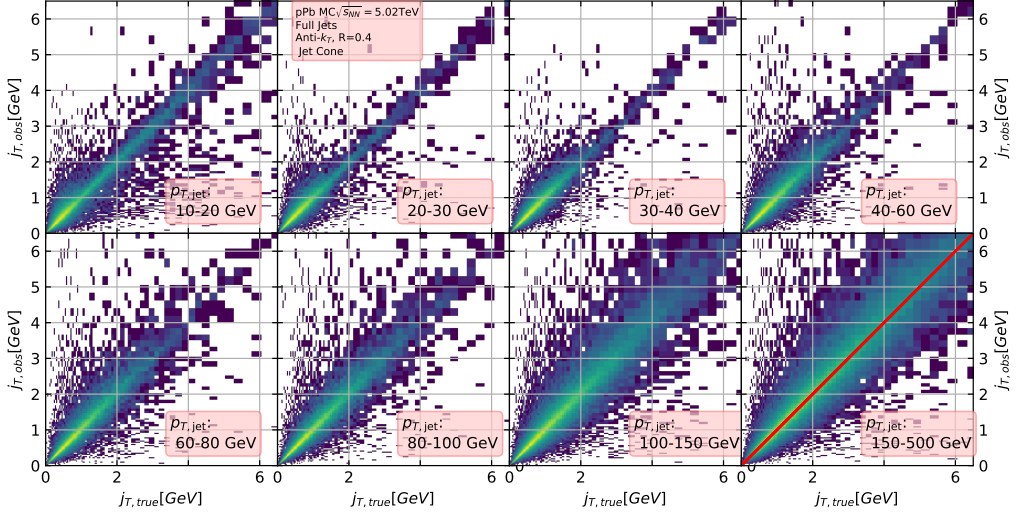


Figure 32:  $j_T$  Response matrices in single jet  $p_T$  bins

1410 In the second method we randomly assign the tracks of event new  $\phi$  and  $\eta$   
1411 values. The result is guaranteed to be uncorrelated.

#### 1412 5.4.1 Perpendicular cone background

1413 After calculating the  $j_T$  values for tracks in the jet, we rotate the jet axis by  $\frac{\pi}{2}$   
1414 in positive  $\phi$  direction. We check that there are no other jets closer than  $2R$  to  
1415 the rotated axis. If there are then background calculation is skipped for this jet.  
1416 Probability of this happening is 1-2% depending on the jet  $p_T$  bin.

1417 If we don't find other jets in the vicinity we move on to estimate the background.  
1418 We find all tracks within a cone of radius  $R$  around the rotated axis and calculate  
1419  $j_T$  of these tracks with respect to the rotated axis. Auto-correlations are added to  
1420 match effect to jet. (see 5.4.3)

#### 1421 5.4.2 Random background

1422 In the random background method we look at all tracks in the event, except for  
1423 tracks close to jets found by the jet algorithm. We randomly assign new  $\eta$  and  $\phi$   
1424 values to all tracks using uniform distribution.  $|\eta| < 1.0$   $p_T$  values are kept the  
1425 same. To increase statistics there is a possibility to create a number of random  
1426 tracks for each actual track. In the analysis we currently do this 10 times for each  
1427 track. Again the track  $p_T$  value is kept the same.

1428 We create a random jet cone from uniform  $\eta$  and  $\phi$  distributions. Here  $|\eta| <$   
1429 0.25. Now we calculate  $j_T$  of the random tracks with respect to the random cone

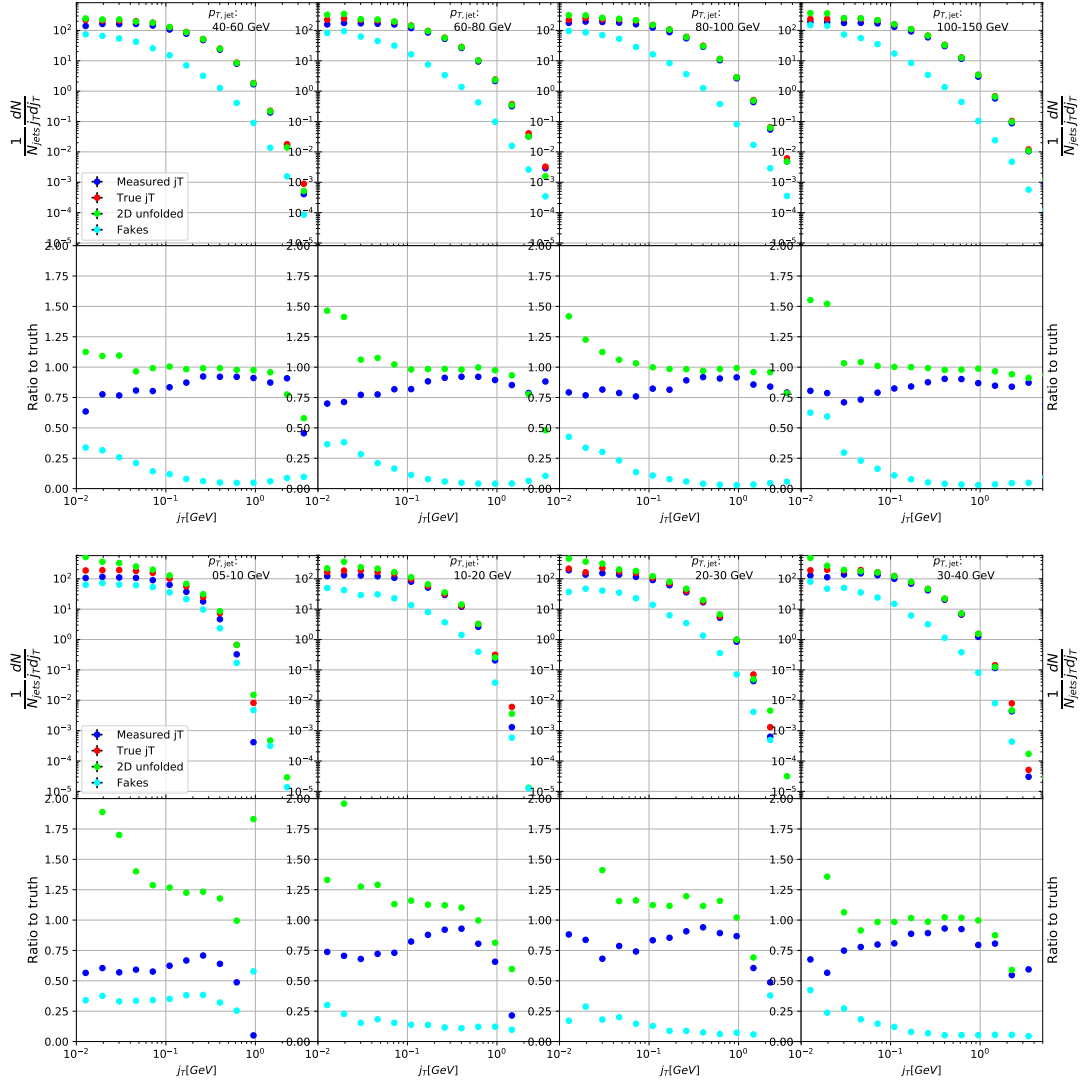
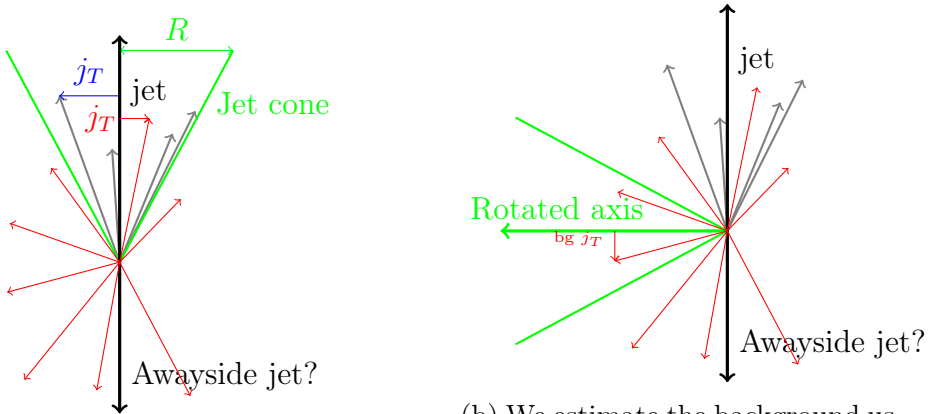
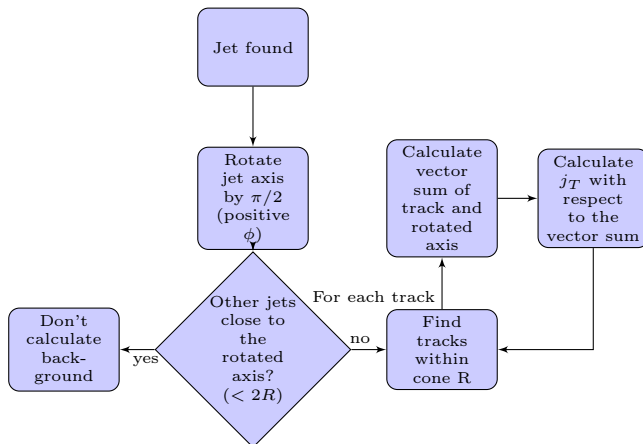


Figure 33: Pythia closure test results. Fake tracks include also tracks that do exist in the true dataset, but for one reason or another were not given  $j_T$  values.  $j_T$  is only calculated for tracks that are associated with jets



(a) Red is underlying event while gray tracks represent the signal  
(b) We estimate the background using a cone where the axis is perpendicular to the jet axis



1430 axis. Auto-correlations are added before calculating  $j_T$  (see 5.4.3)

### 1431 5.4.3 Auto-correlations

1432 Jet axis is simply a vector sum of all its constituents. Thus having an additional  
1433 track in the jet from the underlying event moves the jet axis towards this track.  
1434 Since the axis is now closer to the track, it has a smaller  $j_T$  value. Assuming a 1  
1435 GeV background track at the edge of a  $R = 0.4$  the  $j_T$  value would be 0.4GeV.  
1436 If this is added to a 5GeV jet, the  $j_T$  value becomes 0.33GeV. In a 50GeV jet it  
1437 would be 0.39GeV. This is a region where the inclusive  $j_T$  distribution is domi-  
1438 nated by background. The distribution is also steeply falling. Overestimating the  
1439 background can lead to a situation where the background estimation exceeds the  
1440 inclusive distribution.

1441 To take this effect into account we can't use a fixed axis for background, but  
1442 it has to behave like a jet would when additional tracks are added. Thus before  
1443 calculating  $j_T$  values we make a vector sum of the track and the axis used for back-  
1444 ground, which is either the perpendicular cone axis or the random axis depending  
1445 on the background method. In each case the momentum of this background axis  
1446 is assumed to be the same as the jet which initiated the background estimation.

1447 In pPb data there is on average about one underlying event track in a  $R = 0.4$   
1448 cone.

1449 Extend Background, Perp. cone vs. Random

## 1450 5.5 Fitting

1451 The resulting signal distribution are fitted with a 2 component function shown in  
1452 Eq. 28. Gaussian distribution is used for low  $j_T$  and an inverse gamma function is  
1453 used for high  $j_T$ . The gaussian is taken to have the center at  $j_T = 0$ . In total this  
1454 gives 5 parameters.

$$\frac{1}{N_{\text{jets}} j_T \text{d}j_T} \frac{\text{d}N}{\text{d}j_T} = \frac{B_2}{B_1 \sqrt{2\pi}} e^{-\frac{j_T^2}{2B_1^2}} + \frac{B_3 B_5^{B_4}}{\Gamma(B_4)} \frac{e^{-\frac{B_5}{j_T}}}{j_T^{B_4+1}} \quad (29)$$

1455 To achieve stable results the fitting is performed in two steps. First each  
1456 component is fitted separately. Gaussian component is fitted to the low end in  $j_T$ .  
1457 Inverse gamma component is fitted to  $j_T$  above 1 GeV/c. After getting the results  
1458 from the individual fits they are combined into a single function with initial values  
1459 from the individual results and an additional fit is performed. Fitting only the  
1460 gaussian component to the entire distribution produces approximately the same  
1461 result as the gaussian component in the two-component model.

1462 After getting the fit function  $\sqrt{\langle j_T^2 \rangle}$  (RMS) and yield values are extracted  
1463 separately from each component. The narrow component RMS is

$$\sqrt{\langle j_T^2 \rangle} = \sqrt{2}B_1,$$

1464 and the wide component RMS value is calculated as

$$\sqrt{\langle j_T^2 \rangle} = \frac{B_5}{\sqrt{(B_4 - 2)(B_4 - 3)}},$$

1465 where it is required that  $B_4 > 3$ .

## 1466 6 Systematic uncertainties

### 1467 Extend Systematics

1468 The systematic uncertainties in this analysis come from the background esti-  
1469 mation, the unfolding procedure and the cuts used to select the tracks. Tracking  
1470 uncertainties are estimated from variations of the track selection cuts defined in  
1471 Sec. 2. The resulting variations in RMS are shown in Table 4. The uncertainties  
1472 from unfolding and background subtraction are of the same magnitude.

1473 The systematics in background estimation were studied using an alternative  
1474 method to extract the background, mainly the random background method. The  
1475 resulting uncertainty is below 5% for the wide component RMS and below 9% for  
1476 the narrow component RMS.

1477 The systematic uncertainty that arises from the unfolding procedure is esti-  
1478 mated by performing the unfolding with two separate methods. Data corrected  
1479 by the iterative unfolding method are used as the results and the SVD unfolding  
1480 method is employed to estimate the uncertainty. In a PYTHIA closure test the  
1481 true distribution was in general found to be between the unfolded distributions  
1482 from the iterative and SVD method. The difference between the methods when  
1483 unfolding data should give a reasonable estimate of the unfolding uncertainty. The  
1484 resulting uncertainty is below 8% for both wide and narrow component RMS.

1485 The different source of the systematic uncertainty are considered as uncorre-  
1486 lated and the values of each source are summed in quadrature. The resulting  
1487 uncertainty is 9 % for the wide component RMS and 12 % for the narrow compo-  
1488 nent RMS.

1489 There is no tracking and no unfolding uncertainty in the Monte Carlo simula-  
1490 tions.

Table 3: Summary of systematic errors

Systematic	Wide RMS	Narrow RMS
Background	5 %	9 %
Unfolding	8 %	8 %
Tracking	? %	? %
Total	9 %	12%

<sub>1491</sub> 7 TPC Upgrade?

## 1492 8 Systematic errors

### 1493 8.1 Background subtraction

1494 Fits are performed on both perpendicular cone and random background signals.  
 1495 Difference between them is taken as the systematic error. The fits for individ-  
 1496 ual bins from the random background method are shown in figure 37. Resulting  
 1497 differences between the methods for different components are shown in figure 36.

### 1498 8.2 Unfolding

1499 Unfolding is performed using both SVD and Bayesian unfolding. Difference be-  
 1500 tween the methods is taken as the systematic error. Since SVD unfolding does  
 1501 not have a 2 dimensional options, the unfolding is done bin by bin. The resulting  
 1502 distributions after SVD unfolding and background subtraction with the perpendic-  
 1503 ular cone method are shown in fig ???. Resulting differences between the methods  
 1504 for different components are shown in figure 38.

### 1505 8.3 Tracking

### 1506 8.4 Combining systematics

1507 Resulting systematic errors are shown in table 4. Systematic errors are combined  
 1508 bin-by-bin in quadrature to get the total systematic errors.

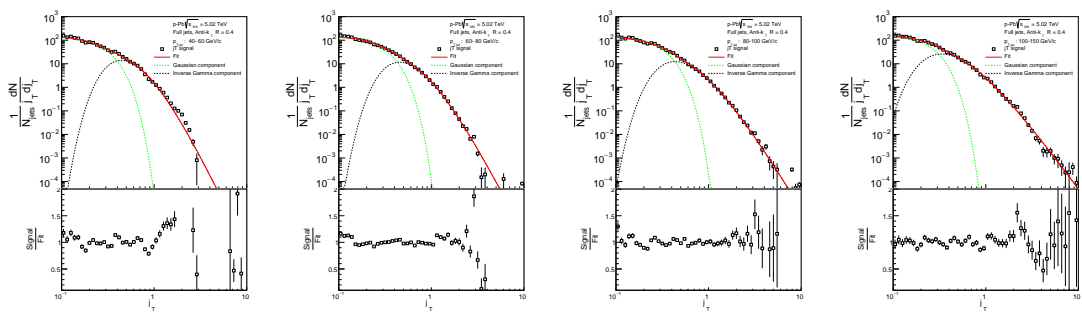


Figure 35:  $j_T$  signal with random background subtraction fits in different jet  $p_T$  bins

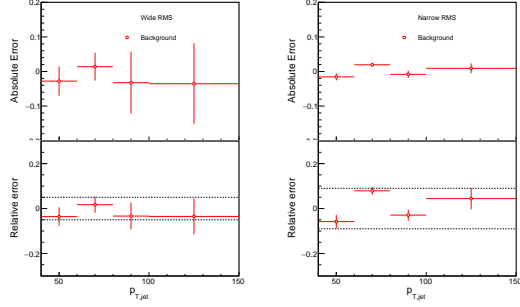


Figure 36: Differences between perpendicular cone and random background subtraction in the resulting RMS values.

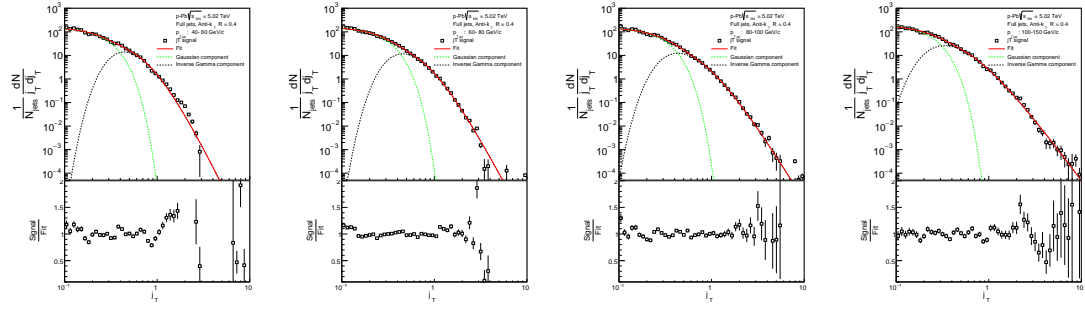


Figure 37:  $j_T$  signal with random background subtraction fits in different jet  $p_T$  bins

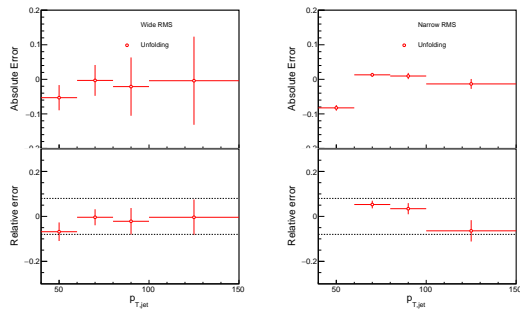


Figure 38: Differences between Bayesian and SVD unfolding in the resulting RMS values

Table 4: Summary of systematic errors

Systematic	Wide RMS	Narrow RMS
Background	5 %	9 %
Unfolding	8 %	8 %
Total	9 %	12%

## 1509 9 Results

### 1510 9.1 statistics

1511 Number of jets in different datasets and with different jet finders is shown in table  
 1512 5. Background statistics for number of background cones (number of jets minus  
 1513 number of discarded cones) are shown in table 6. Ratio of background cones to  
 1514 number of jets is shown in table 7. The likelihood of having to discard a jet from  
 background calculation is about 1-2%.

Table 5: Number of found jets by dataset and jet  $p_T$  bin

Jet $p_T$	5-10	10-20	20-30	30-40	40-60	60-80	80-100	100-150	150-500
MBFullR04	4969393	621753	32552	5584	1974	310	90	37	5
MBFullR05	4750567	826598	42373	5543	1719	276	73	29	3
MBChargedR04	3144538	673419	37783	4121	1009	148	36	12	1
MBChargedR05	2229247	175763	7961	1270	410	61	12	3	
TriggeredFullR04	187557	115927	78138	51317	39262	8621	2409	1167	171
TriggeredFullR05	99991	77147	48612	34325	28104	6342	1726	794	104
TriggeredChargedR04	37411	29945	18186	13148	11142	2517	675	326	44
TriggeredChargedR05	433155	175031	54789	19776	10626	1983	457	194	15

1515

Table 6: Number of background cones used in perpendicular cone background calculation

Jet $p_T$	5-10	10-20	20-30	30-40	40-60	60-80	80-100	100-150	150-500
MBFullR04	4947583	617895	32357	5548	1965	310	90	37	5
MBFullR05	4710217	815461	41584	5439	1698	273	73	29	3
MBChargedR04	3117495	661106	36739	4014	988	144	36	12	1
MBChargedR05	2195286	172919	7860	1249	406	61	12	3	
TriggeredFullR04	186574	115376	77949	51216	39196	8603	2405	1167	171
TriggeredFullR05	99102	76462	48320	34216	28038	6334	1722	794	103
TriggeredChargedR04	37160	29543	17988	13099	11129	2515	675	326	44
TriggeredChargedR05	313421	140707	45229	16243	8709	1604	377	154	14

Table 7: Ratio of background cone number to number of jets

MBFullR04	99.56%	99.38%	99.40%	99.36%	99.54%	100.00%	100.00%	100.00%	100.00%
MBFullR05	99.15%	98.65%	98.14%	98.12%	98.78%	98.91%	100.00%	100.00%	100.00%
MBChargedR04	99.14%	98.17%	97.24%	97.40%	97.92%	97.30%	100.00%	100.00%	100.00%
MBChargedR05	98.48%	98.38%	98.73%	98.35%	99.02%	100.00%	100.00%	100.00%	100.00%
TriggeredFullR04	99.48%	99.52%	99.76%	99.80%	99.83%	99.79%	99.83%	100.00%	100.00%
TriggeredFullR05	99.11%	99.11%	99.40%	99.68%	99.77%	99.87%	99.77%	100.00%	99.04%
TriggeredChargedR04	99.33%	98.66%	98.91%	99.63%	99.88%	99.92%	100.00%	100.00%	100.00%
TriggeredChargedR05	72.36%	80.39%	82.55%	82.13%	81.96%	80.89%	82.49%	79.38%	93.33%

## 1516 9.2 Data

### 1517 9.3 Background

1518 Comparison between perpendicular cone and random background in figure 39.

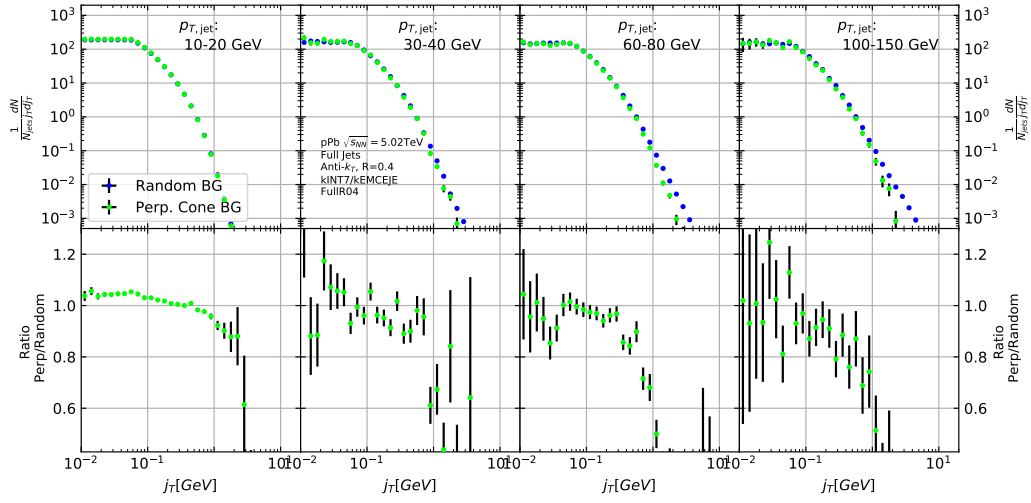


Figure 39:  $j_T$  background with two different methods

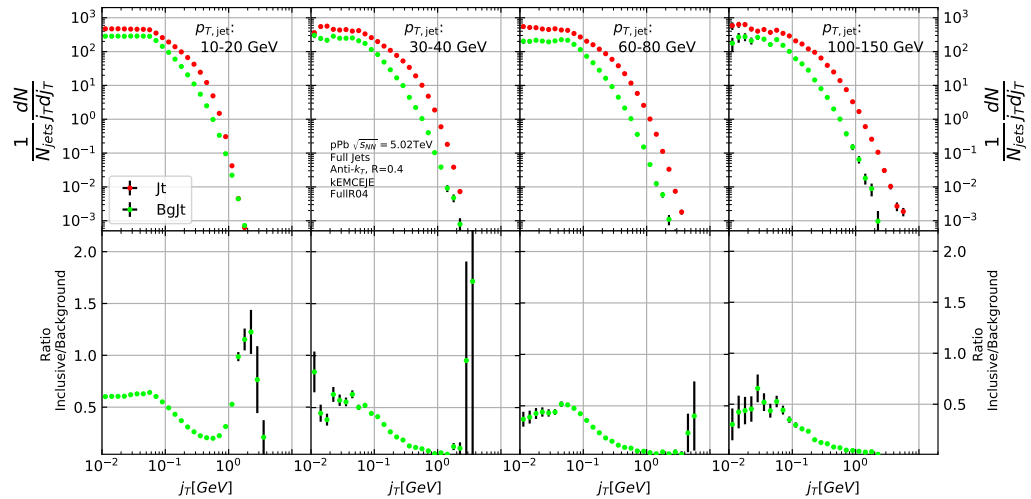


Figure 40: Inclusive  $j_T$  with background

1519 **9.4 Inclusive results**

1520 Results in figure 40

1521 **9.5 Comparison between A and C side**

1522 In 2013 there were some issues with tracking. To rule out effects on  $j_T$  distributions  
1523 a study was performed comparing  $j_T$  distributions between A and C side. No  
1524 systematic differences were observed.

1525 **9.6 Subtracted signal**

1526 Results in figure 42. Comparison between signals with different backgrounds in  
1527 figure 43

1528 **9.7 Fitting**

1529 Fits of  $j_T$  distributions in different jet  $p_T$  bins with  $p_T > 40\text{GeV}$  are shown in figure  
1530 44. Additional jet  $p_T$  bins are shown in appendix ???. In lowest jet  $p_T$  bins the  
1531 jets are mainly combinatorial which makes background subtraction and unfolding  
1532 difficult and thus the signal can't be trusted.

1533 The fits describe the data well. There is some fluctuation of the order of 10 %  
1534 around the fit function. At hight  $j_T$  the statistical errors in the signal are large.

1535 **9.7.1 Results**

1536 RMS and yield results with systematic errors are shown separately in figure 45.  
1537 Figure 46 shows RMS values for both components combined. The figure also  
1538 includes results from a PYTHIA simulation.

1539 **9.8 Comparison to dihadron results**

1540 Comparison to RMS values in dihadron analysis [?] are shown in figure Dihadron  
1541 results from [?]. For comparison the dihadron trigger  $p_T$  bins are converted to jet  
1542  $p_T$  bins and vice versa. Bin-by-bin comparison is still not possible, but dihadron  
1543 analysis gives systematically larger RMS values. This could be caused by several  
1544 kinematical factors. In jet  $j_T$  analysis the jet cone limits possible  $j_T$  values and  
1545 thus the width and RMS of the  $j_T$  distributions. The effect of this limitation can  
1546 be studied by changing the cone size as is described in section 9.9.

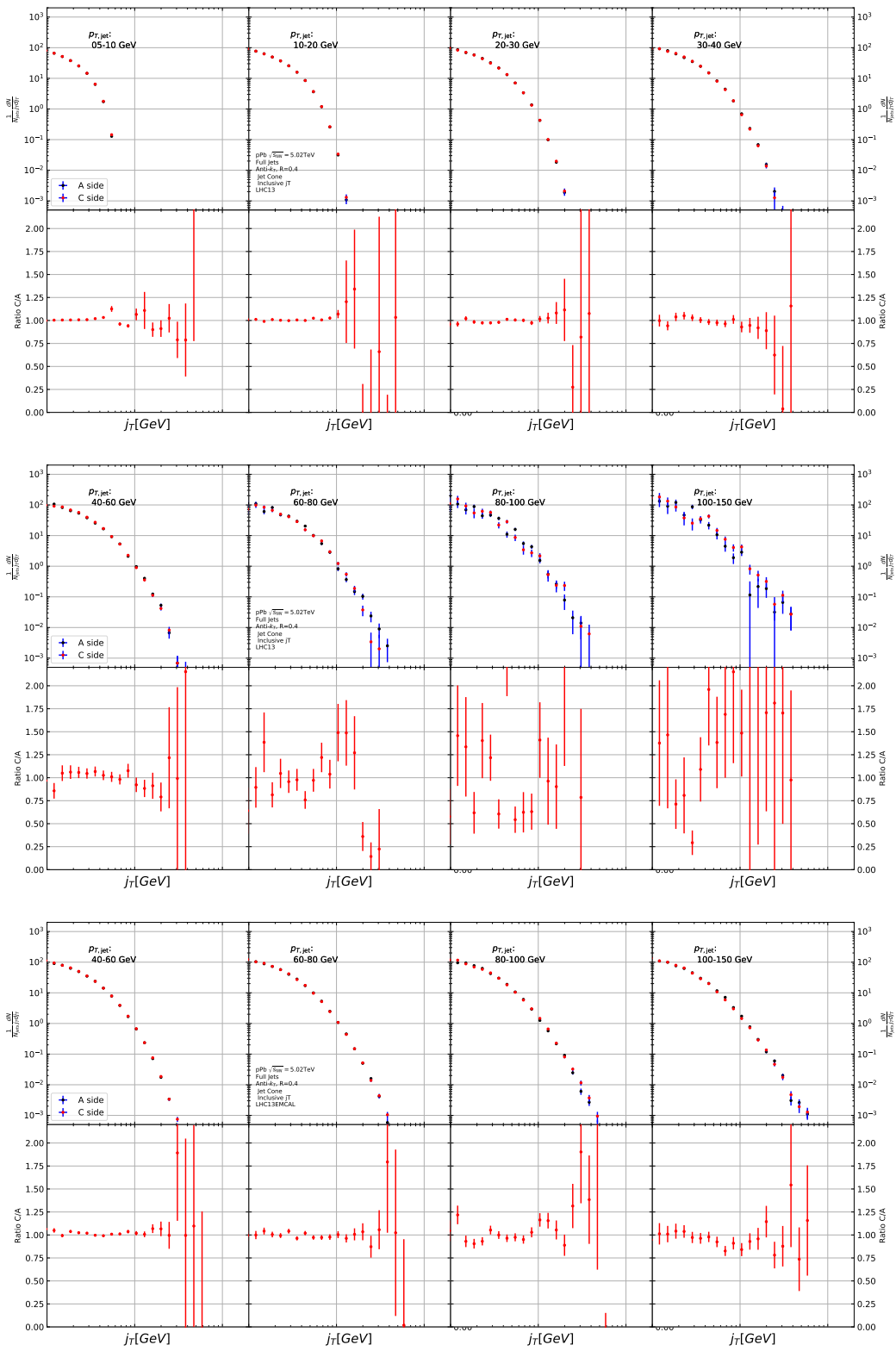


Figure 41: Comparison of inclusive  $j_T$  distributions between A and C side for minimum bias and EMCAL triggered data.

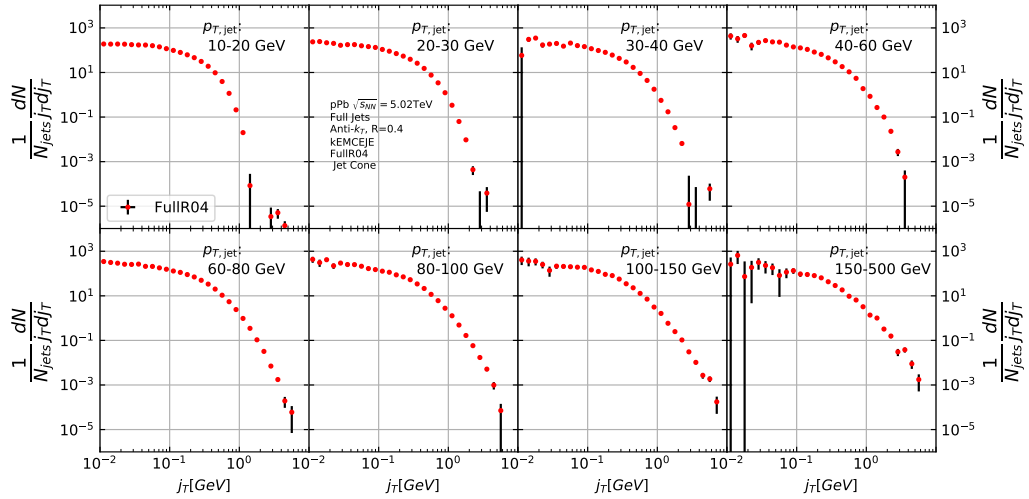


Figure 42:  $j_T$  signal with background subtracted

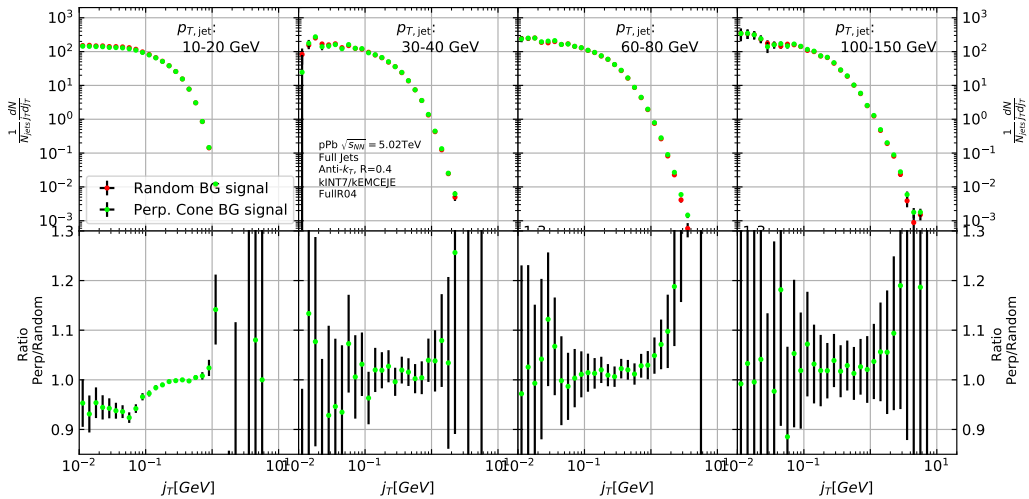


Figure 43: Comparison of the effect of background method on  $j_T$  signal.

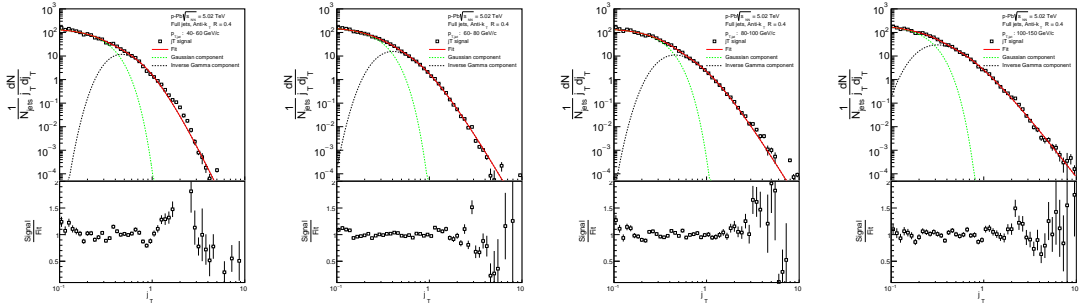


Figure 44:  $j_T$  signal fits in different jet  $p_T$  bins

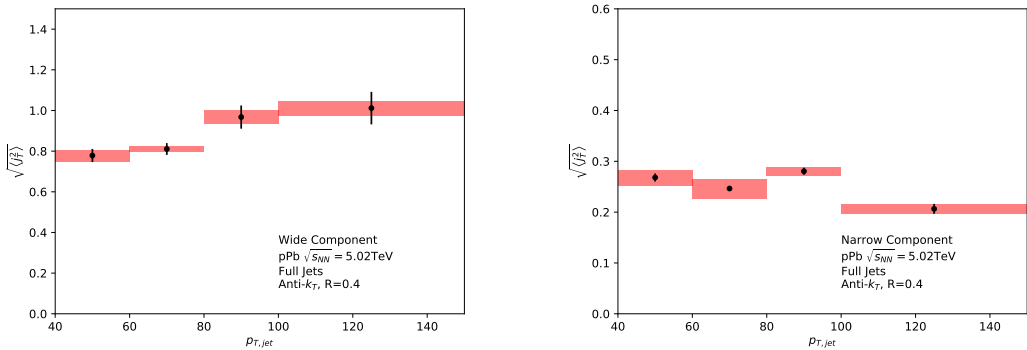


Figure 45: RMS values extracted from the fits for the gaussian (narrow) and inverse gamma (wide) components

1547 Comparison to  $j_T$  results from dihadron analysis [?] is shown in figure 50.  
 1548 Trigger  $p_T$  bins used in dihadron analysis are converted to jet  $p_T$  bins using ob-  
 1549 served average jet  $p_T$  values in leading track momentum bins. Similarly jet  $p_T$  bins  
 1550 are converted to  $p_{T,\text{trigger}}$  bins using average leading track  $p_T$  values in  $p_{T,\text{jet}}$  bins.

1551 The trends are similar in dihadron and jet  $j_T$  results. Wide component RMS  
 1552 values tend to increase with increasing  $p_{T,\text{trigger}}/p_{T,\text{jet}}$ . Narrow component RMS  
 1553 increases slightly in dihadron analysis but not in jet  $j_T$ , WHY? (Depends on  $x_{||}$   
 1554 bin in dihadron)

1555 In general dihadron  $j_T$  gives wider distributions with larger RMS values. In  
 1556 jet analysis the cone size limits width and thus the RMS values. The effect of this  
 1557 limitation can be studied by changing the cone size as is described in section 9.9.

1558 Additionally the leading track is an imperfect estimate of the jet/original par-  
 1559 ton. Because the leading track in general is at an angle compared to the jet axis,  
 1560 the resulting  $j_T$  values are different. In practice the jet axis found by the jet finding  
 1561 algorithm tends to minimize the average  $j_T$  of jet constituents. Thus the yield at

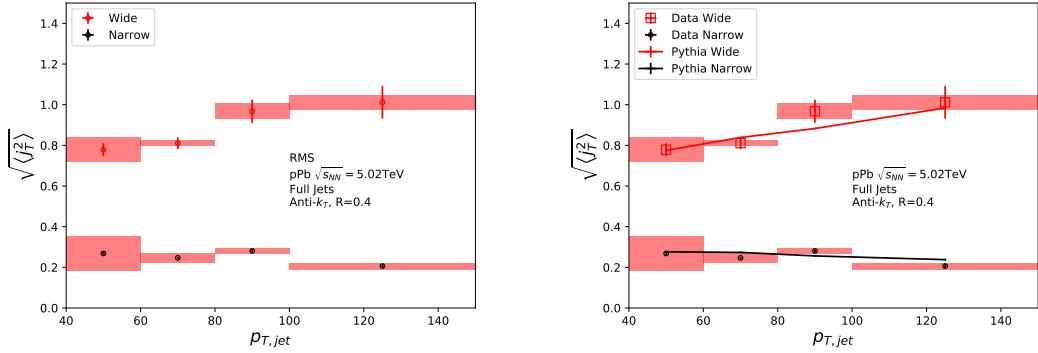


Figure 46: RMS values extracted from the fits for the gaussian (narrow) and inverse gamma (wide) components

high  $j_T$  is limited and the RMS values are smaller.

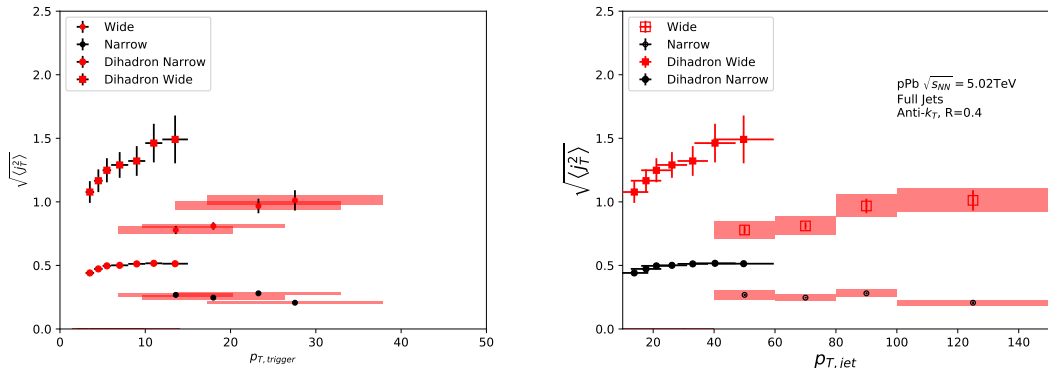


Figure 47: Jet  $j_T$  results are compared to results obtained in the dihadron analysis. This is done both in jet  $p_T$  and trigger  $p_T$  bins by converting between them.

## 9.9 Different $R$ parameters

Study the effect of cone sizes on  $j_T$  distribution in particle level Pythia.

Increasing the cone size of jets gives more room for high  $j_T$  tracks. This is seen in the individual  $j_T$  distributions as increased high  $j_T$  production. At low  $j_T$  there is no change.

When looking at RMS values from wide component we see an increase/decrease of about 10% when going from  $R = 0.4$  to  $R = 0.5/R = 0.3$ .

1570 The message from narrow component RMS values is less clear. At low jet  $p_T$   
 the behaviour is similar, but at high  $p_T$  the order is reversed.

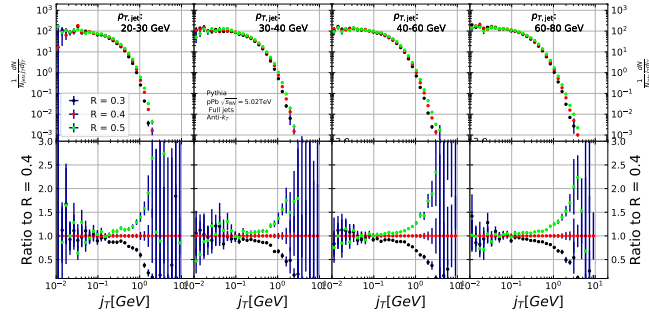


Figure 48: Effect of changing  $R$  parameter in jet finding on  $j_T$  distributions

1571

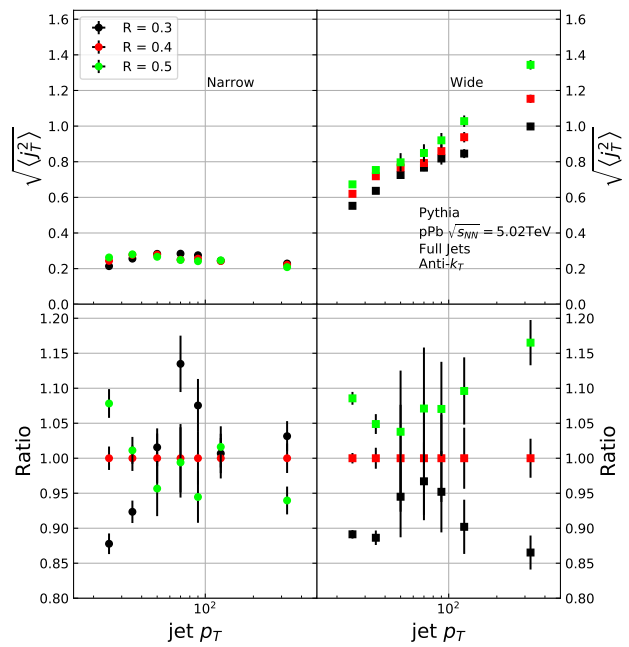


Figure 49: Effect of changing  $R$  parameter in jet finding on narrow and wide component RMS values. Wide component RMS values increase with increasing cone size.

## 1572 10 Discussion

### 1573 10.1 Discussion

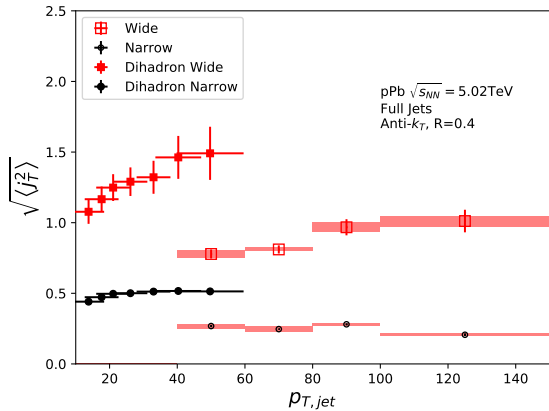


Figure 50: Comparison of results with dihadron  $j_T$  results. Dihadron trigger  $p_T$  bins are converted to jet  $p_T$  bins using observed mean  $p_{T,jet}$  values in  $p_{T,trigger}$  bins. Dihadron results are for  $0.2 < x_{||} < 0.4$

1574 Comparison to  $j_T$  results from dihadron analysis [107] is shown in Fig. 50.  
 1575 Trigger  $p_T$  bins used in dihadron analysis are converted to jet  $p_T$  bins using ob-  
 1576 served average jet  $p_T$  values in leading track momentum bins. Similarly jet  $p_T$  bins  
 1577 are converted to  $p_{T,trigger}$  bins using average leading track  $p_T$  values in  $p_{T,jet}$  bins.

1578 The trends are similar in dihadron and jet  $j_T$  results. Wide component RMS  
 1579 values tend to increase with increasing  $p_{T,trigger}/p_{T,jet}$ . Narrow component RMS  
 1580 increases slightly in dihadron analysis but not in jet  $j_T$ , WHY? (Depends on  $x_{||}$   
 1581 bin in dihadron)

1582 In general dihadron  $j_T$  gives wider distributions with larger RMS values. In  
 1583 jet analysis the cone size limits width and thus the RMS values. With increasing  
 1584 cone size one gets increasing wide RMS values as seen in Fig. 51. This should be  
 1585 the dominant factor.

1586 Effect of the  $R$  parameter choice is studied in PYTHIA. Having a fixed cone  
 1587 puts hard limits on the possible  $j_T$  values. Increasing the cone size loosens these  
 1588 limits and allows higher  $j_T$  values. The results are shown in Fig. 51. Left hand  
 1589 side shows the  $j_T$  distributions. There is very little change in low  $j_T$  but at high  
 1590  $j_T$  the yield increases.

1591 This is also seen in the RMS values shown in the right hand side of Fig. 51,  
 1592 where the change in wide component RMS is about 10% when going from  $R = 0.4$   
 1593 to  $R = 0.3$  or  $R = 0.5$ . With the narrow component values the situation is less



Figure 51: Effect of changing  $R$  parameter in jet finding on  $j_T$  distributions

clear. At low jet  $p_T$  larger  $R$  parameter leads to larger RMS values, but at high  $p_{T\text{jet}}$  the situation is reversed; increasing the  $R$  parameter decreases RMS values.

Additionally the leading track is an imperfect estimate of the jet/original parton. Because the leading track in general is at an angle compared to the jet axis, the resulting  $j_T$  values are different. In practice the jet axis found by the jet finding algorithm tends to minimize the average  $j_T$  of jet constituents. Thus the yield at high  $j_T$  is limited and the RMS values are smaller.

A PYTHIA study was performed where  $j_T$  was calculated with respect to the leading track momentum, instead of the jet axis. The results are shown in Fig. 52. The resulting  $j_T$  distributions are significantly wider than  $j_T$  distributions from the typical method. The effect seems to be larger than the effect seen in comparing different  $R$  values.

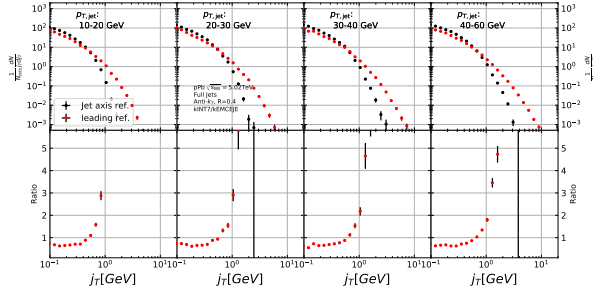


Figure 52: Results of calculating  $j_T$  with respect to the jet axis or the leading hadron. The assumption is that because the leading hadron is an imperfect estimate of the jet axis, low  $j_T$  tracks should on average be shifted to higher  $j_T$

## 1606 11 Summary

1607 In this work two distinct  $j_T$  components were extracted for narrow and wide contri-  
1608 butions using jet reconstruction. RMS values for both components were obtained.  
1609 The width of the wide component is found to increase for increasing  $p_{T\text{jet}}$ . This  
1610 is in part explained by the changing kinematical limits when going to higher  $p_{T\text{jet}}$   
1611 which allows higher  $p_{T\text{track}}$ . Additionally the larger phase space allows stronger  
1612 parton splitting. The results are qualitatively compatible with previous studies  
1613 that studied  $j_T$  using two-particle correlations.

## 1614 References

- 1615 [1] PHENIX Collaboration, K. Adcox *et al.*, Nucl.Phys. **A757**, 184 (2005),  
1616 nucl-ex/0410003.
- 1617 [2] STAR Collaboration, J. Adams *et al.*, Nucl.Phys. **A757**, 102 (2005), nucl-  
1618 ex/0501009.
- 1619 [3] J.-Y. Ollitrault, Phys. Rev. D **46**, 229 (1992).
- 1620 [4] U. Heinz and P. Kolb, Nucl. Phys. **A702**, 269 (2002).
- 1621 [5] E. Shuryak, Prog. Part. Nucl. Phys. **62**, 48 (2009).
- 1622 [6] ATLAS Collaboration, J. Jia, Nucl.Phys.A904-905 **2013**, 421c (2013),  
1623 1209.4232.
- 1624 [7] R. A. Lacey *et al.*, (2012), 1207.1886.
- 1625 [8] R. Bjorklund, W. Crandall, B. J. Moyer, and H. York, Phys. Review **77**,  
1626 213 (1950).
- 1627 [9] W. Heisenberg, Zeitschrift für Physik **77**, 1 (1932).
- 1628 [10] M. Gell-Mann, Phys. Rev. **125**, 1067 (1962).
- 1629 [11] M. Gell-Mann, Phys. Lett. **8**, 214 (1964).
- 1630 [12] O. Greenberg, Phys. Rev. Lett. **13**, 598 (1964).
- 1631 [13] Crystal Ball Collaboration, D. Williams *et al.*, Phys.Rev. **D38**, 1365 (1988).
- 1632 [14] W. Krolikowski, Nuovo Cim. **A27**, 194 (1975).
- 1633 [15] D. J. Gross and F. Wilczek, Physical Review Letters **30**, 1343 (1973).
- 1634 [16] H. D. Politzer, Physical Review Letters **30**, 1346 (1973).
- 1635 [17] D. J. Gross and F. Wilczek, Physical Review D **8**, 3633 (1973).
- 1636 [18] D. J. Gross and F. Wilczek, Physical Review D **9**, 980 (1974).
- 1637 [19] H. Georgi and H. D. Politzer, Physical Review D **9**, 416 (1974).
- 1638 [20] H. Fritzsch, M. Gell-Mann, and H. Leutwyler, Physics Letters B **47**, 365  
1639 (1973).

- <sub>1640</sub> [21] I. Flegel and P. Söding, CERN courier (2004).
- <sub>1641</sub> [22] R. Brandelik *et al.*, Physics Letters B **86**, 243 (1979).
- <sub>1642</sub> [23] J. K. L. MacDonald, Phys. Rev. **43**, 830 (1933).
- <sub>1643</sub> [24] C. Berger *et al.*, Physics Letters B **86**, 418 (1979).
- <sub>1644</sub> [25] J. Collins and M. Perry, Phys. rev. Lett. **34**, 1353 (1975).
- <sub>1645</sub> [26] E. Shuryak, Phys. Reps. **61**, 71 (1980).
- <sub>1646</sub> [27] K. Rajagopal, SLAC Beam Line **31-2**, 9 (2001).
- <sub>1647</sub> [28] P. Kovtun, D. Son, and A. Starinets, Phys.Rev.Lett. **94**, 111601 (2005), hep-th/0405231.
- <sub>1649</sub> [29] R. A. Lacey *et al.*, Phys. Rev. Lett. **98**, 092301 (2007).
- <sub>1650</sub> [30] E. Lofgren, *ACCELERATOR DIVISION ANNUAL REPORTS, 1 JULY 1972 12/31/1974* (, 1975).
- <sub>1652</sub> [31] D. S. Barton, Heavy ion program at bnl: Ags, rhic, in *Proc. 1987 Particle Accelerator Conference, Washington, D.C., March, 1987*.
- <sub>1654</sub> [32] I. Vitev and M. Gyulassy, Phys.Rev.Lett. **89**, 252301 (2002), hep-ph/0209161.
- <sub>1656</sub> [33] S. Choi and K. S. Lee, Phys. Rev. C **84**, 064905 (2011).
- <sub>1657</sub> [34] A. Kovalenko *et al.*, Status of the nuclotron, in *Proceedings of EPAC Vol. 94*, pp. 161–164, 1994.
- <sub>1659</sub> [35] NA61/SHINE, K. Grebieszkow, PoS **CPOD2013**, 004 (2013).
- <sub>1660</sub> [36] BRAHMS Collaboration, I. Arsene *et al.*, Nucl.Phys. **A757**, 1 (2005), nucl-ex/0410020.
- <sub>1662</sub> [37] B. Back *et al.*, Nucl.Phys. **A757**, 28 (2005), nucl-ex/0410022.
- <sub>1663</sub> [38] S. A. Voloshin, A. M. Poskanzer, and R. Snellings, (2008), 0809.2949.
- <sub>1664</sub> [39] S. A. Voloshin, A. M. Poskanzer, A. Tang, and G. Wang, Phys.Lett. **B659**, 537 (2008), 0708.0800.
- <sub>1666</sub> [40] H. Holopainen, H. Niemi, and K. J. Eskola, Phys.Rev. **C83**, 034901 (2011), 1007.0368.

- <sub>1668</sub> [41] ALICE Collaboration, Phys. Rev. C **88**, 044909 (2013).
- <sub>1669</sub> [42] M. L. Miller, K. Reygers, S. J. Sanders, and P. Steinberg,  
<sub>1670</sub> Ann.Rev.Nucl.Part.Sci. **57**, 205 (2007), nucl-ex/0701025.
- <sub>1671</sub> [43] R. Glauber, Lectures in theoretical physics, 1959.
- <sub>1672</sub> [44] W. Czyż and L. Maximon, Annals of Physics **52**, 59 (1969).
- <sub>1673</sub> [45] A. Białłas, M. Bleszyński, and W. Czyż, Nuclear Physics B **111**, 461 (1976).
- <sub>1674</sub> [46] PHENIX Collaboration, S. Afanasiev *et al.*, Phys.Rev. **C80**, 054907 (2009),  
<sub>1675</sub> 0903.4886.
- <sub>1676</sub> [47] J.-Y. Ollitrault, Eur.J.Phys. **29**, 275 (2008), 0708.2433.
- <sub>1677</sub> [48] P. Romatschke, Int.J.Mod.Phys. **E19**, 1 (2010), 0902.3663.
- <sub>1678</sub> [49] L. LD, Izv. Akad. Nauk Ser. Fiz. **17**, 51 (1953).
- <sub>1679</sub> [50] H. Song, S. Bass, and U. W. Heinz, (2013), 1311.0157.
- <sub>1680</sub> [51] H. Niemi, G. Denicol, P. Huovinen, E. Molnar, and D. Rischke, Phys.Rev.  
<sub>1681</sub> **C86**, 014909 (2012), 1203.2452.
- <sub>1682</sub> [52] K. A. *et al.* [ALICE Collaboration], Phys. Rev. Lett **106** (2011), 032301.
- <sub>1683</sub> [53] J.-Y. Ollitrault, Phys.Rev. D **48**, 1132 (1993), hep-ph/9303247.
- <sub>1684</sub> [54] P. Danielewicz and G. Odyniec, Physics Letters B **157**, 146 (1985).
- <sub>1685</sub> [55] P. Danielewicz and M. Gyulassy, Physics Letters B **129**, 283 (1983).
- <sub>1686</sub> [56] T. Abbott *et al.*, Phys. Rev. Lett. **70**, 1393 (1993).
- <sub>1687</sub> [57] S. Voloshin and Y. Zhang, Z.Phys. **C70**, 665 (1996), hep-ph/9407282.
- <sub>1688</sub> [58] E877 Collaboration, J. Barrette *et al.*, Phys.Rev.Lett. **73**, 2532 (1994), hep-  
<sub>1689</sub> ex/9405003.
- <sub>1690</sub> [59] CMS Collaboration, S. Chatrchyan *et al.*, Phys.Rev.Lett. **109**, 022301  
<sub>1691</sub> (2012), 1204.1850.
- <sub>1692</sub> [60] A. Majumder and M. Van Leeuwen, Prog.Part.Nucl.Phys. **A66**, 41 (2011),  
<sub>1693</sub> 1002.2206.

- <sub>1694</sub> [61] F. Dominguez, C. Marquet, A. Mueller, B. Wu, and B.-W. Xiao, Nucl.Phys. **A811**, 197 (2008), 0803.3234.
- <sub>1696</sub> [62] M. Gyulassy, P. Levai, and I. Vitev, Nucl.Phys. **B571**, 197 (2000), hep-ph/9907461.
- <sub>1698</sub> [63] U. A. Wiedemann, Nucl.Phys. **B588**, 303 (2000), hep-ph/0005129.
- <sub>1699</sub> [64] P. B. Arnold, G. D. Moore, and L. G. Yaffe, JHEP **0112**, 009 (2001), hep-ph/0111107.
- <sub>1701</sub> [65] X.-N. Wang and X.-f. Guo, Nucl.Phys. **A696**, 788 (2001), hep-ph/0102230.
- <sub>1702</sub> [66] T. Sjostrand, S. Mrenna, and P. Z. Skands, Comput.Phys.Commun. **178**, 852 (2008), 0710.3820.
- <sub>1704</sub> [67] I. Lokhtin and A. Snigirev, Eur.Phys.J. **C45**, 211 (2006), hep-ph/0506189.
- <sub>1705</sub> [68] N. Armesto, L. Cunqueiro, and C. A. Salgado, Nucl.Phys. **A830**, 271C (2009), 0907.4706.
- <sub>1707</sub> [69] K. Zapp, G. Ingelman, J. Rathsman, J. Stachel, and U. A. Wiedemann, Eur.Phys.J. **C60**, 617 (2009), 0804.3568.
- <sub>1709</sub> [70] T. Renk, Phys.Rev. **C79**, 054906 (2009), 0901.2818.
- <sub>1710</sub> [71] ALICE Collaboration, K. Aamodt *et al.*, Phys.Lett. **B696**, 30 (2011), 1012.1004.
- <sub>1712</sub> [72] WA98 Collaboration, M. Aggarwal *et al.*, Eur.Phys.J. **C23**, 225 (2002), nucl-ex/0108006.
- <sub>1714</sub> [73] D. G. d'Enterria, Phys.Lett. **B596**, 32 (2004), nucl-ex/0403055.
- <sub>1715</sub> [74] PHENIX Collaboration, A. Adare *et al.*, Phys.Rev.Lett. **101**, 232301 (2008), 0801.4020.
- <sub>1717</sub> [75] STAR Collaboration, J. Adams *et al.*, Phys.Rev.Lett. **91**, 172302 (2003), nucl-ex/0305015.
- <sub>1719</sub> [76] A. Dainese, C. Loizides, and G. Paic, Eur.Phys.J. **C38**, 461 (2005), hep-ph/0406201.
- <sub>1721</sub> [77] I. Vitev, J.Phys. **G30**, S791 (2004), hep-ph/0403089.
- <sub>1722</sub> [78] C. A. Salgado and U. A. Wiedemann, Phys.Rev. **D68**, 014008 (2003), hep-ph/0302184.

- <sub>1724</sub> [79] N. Armesto, A. Dainese, C. A. Salgado, and U. A. Wiedemann, Phys.Rev. **D71**, 054027 (2005), hep-ph/0501225.
- <sub>1726</sub> [80] T. Renk, H. Holopainen, R. Paatelainen, and K. J. Eskola, Phys.Rev. **C84**, 014906 (2011), 1103.5308.
- <sub>1728</sub> [81] CMS Collaboration, S. Chatrchyan *et al.*, Eur.Phys.J. **C72**, 1945 (2012), 1202.2554.
- <sub>1730</sub> [82] PHENIX Collaboration, S. Afanasiev *et al.*, Phys. Rev. C **80**, 054907 (2009).
- <sub>1731</sub> [83] ALICE Collaboration, K. Aamodt *et al.*, Phys.Rev.Lett. **108**, 092301 (2012), 1110.0121.
- <sub>1733</sub> [84] J. L. Nagle and W. A. Zajc, Ann. Rev. Nucl. Part. Sci. **68**, 211 (2018), 1801.03477.
- <sub>1735</sub> [85] E735, T. Alexopoulos *et al.*, Phys. Rev. **D48**, 984 (1993).
- <sub>1736</sub> [86] MiniMax, T. C. Brooks *et al.*, Phys. Rev. **D61**, 032003 (2000), hep-ex/9906026.
- <sub>1738</sub> [87] C. Shen, Z. Qiu, and U. Heinz, Phys. Rev. **C92**, 014901 (2015), 1502.04636.
- <sub>1739</sub> [88] PHENIX, A. Adare *et al.*, Phys. Rev. **C94**, 064901 (2016), 1509.07758.
- <sub>1740</sub> [89] C. A. Salgado and J. P. Wessels, Ann. Rev. Nucl. Part. Sci. **66**, 449 (2016).
- <sub>1741</sub> [90] M. Gyulassy, I. Vitev, X.-N. Wang, and B.-W. Zhang, p. 123 (2003), nucl-th/0302077.
- <sub>1743</sub> [91] E. Norbeck, K. Šafařík, and P. A. Steinberg, Annual Review of Nuclear and Particle Science **64**, 383 (2014), <https://doi.org/10.1146/annurev-nucl-102912-144532>.
- <sub>1746</sub> [92] A. Accardi, F. Arleo, W. K. Brooks, D. D'Enterria, and V. Muccifora, Riv. Nuovo Cim. **32**, 439 (2010), 0907.3534.
- <sub>1748</sub> [93] ALICE, K. Aamodt *et al.*, JINST **3**, S08002 (2008).
- <sub>1749</sub> [94] ALICE, B. B. Abelev *et al.*, Int. J. Mod. Phys. **A29**, 1430044 (2014), 1402.4476.
- <sub>1751</sub> [95] ALICE, K. Aamodt *et al.*, JINST **5**, P03003 (2010), 1001.0502.
- <sub>1752</sub> [96] J. Alme *et al.*, Nucl. Instrum. Meth. **A622**, 316 (2010), 1001.1950.

- <sub>1753</sub> [97] ALICE, B. Abelev *et al.*, JHEP **03**, 053 (2012), 1201.2423.
- <sub>1754</sub> [98] ALICE, P. Cortese *et al.*, (2008).
- <sub>1755</sub> [99] J. Allen *et al.*, Report No. CERN-LHCC-2010-011. ALICE-TDR-14-add-1,  
<sub>1756</sub> 2010 (unpublished).
- <sub>1757</sub> [100] ALICE, G. Dellacasa *et al.*, (1999).
- <sub>1758</sub> [101] ALICE Collaboration, *Technical Design Report on Forward Detectors: FMD, T0 and V0*, 2004.
- <sub>1760</sub> [102] ALICE, B. Abelev *et al.*, Phys. Lett. **B719**, 29 (2013), 1212.2001.
- <sub>1761</sub> [103] M. Cacciari, G. P. Salam, and G. Soyez, Eur. Phys. J. **C72**, 1896 (2012),  
<sub>1762</sub> 1111.6097.
- <sub>1763</sub> [104] M. Cacciari, G. P. Salam, and G. Soyez, JHEP **04**, 063 (2008), 0802.1189.
- <sub>1764</sub> [105] T. Sjöstrand, S. Mrenna, and P. Z. Skands, Comput. Phys. Commun. **178**,  
<sub>1765</sub> 852 (2008), 0710.3820.
- <sub>1766</sub> [106] Roounfold: Root unfolding framework, <http://hepunx.rl.ac.uk/~adye/software/unfold/RooUnfold.html>, 2013.
- <sub>1768</sub> [107] <https://alice-publications.web.cern.ch/node/3655>, 2018.